



AFRL-OSR-VA-TR-2014-0374

Nonlinear High-Energy Pulse Propagation in Graded-Index Multimode Optical Fibers

Arash Mafi
UNIVERSITY OF WISCONSIN SYSTEM

12/23/2014
Final Report

DISTRIBUTION A: Distribution approved for public release.

Air Force Research Laboratory
AF Office Of Scientific Research (AFOSR)/ RTB
Arlington, Virginia 22203
Air Force Materiel Command

REPORT DOCUMENTATION PAGE					<i>Form Approved</i> OMB No. 0704-0188	
<p>The public reporting burden for this collection of information is estimated to average 1 hour per response, including the time for reviewing instructions, searching existing data sources, gathering and maintaining the data needed, and completing and reviewing the collection of information. Send comments regarding this burden estimate or any other aspect of this collection of information, including suggestions for reducing the burden, to Department of Defense, Washington Headquarters Services, Directorate for Information Operations and Reports (0704-0188), 1215 Jefferson Davis Highway, Suite 1204, Arlington, VA 22202-4302. Respondents should be aware that notwithstanding any other provision of law, no person shall be subject to any penalty for failing to comply with a collection of information if it does not display a currently valid OMB control number.</p> <p>PLEASE DO NOT RETURN YOUR FORM TO THE ABOVE ADDRESS.</p>						
1. REPORT DATE (DD-MM-YYYY) 12/22/2014		2. REPORT TYPE Final			3. DATES COVERED (From - To) 7/1/2012-9/30/2014	
4. TITLE AND SUBTITLE Nonlinear High-Energy Pulse Propagation in Graded-Index Multimode Optical Fibers for Mode-Locked Fiber Lasers				5a. CONTRACT NUMBER		
				5b. GRANT NUMBER FA9550-12-1-0329		
				5c. PROGRAM ELEMENT NUMBER		
6. AUTHOR(S) Arash Mafi Department of Physics & Astronomy, University of New Mexico formerly at the University of Wisconsin-Milwaukee 3200 Cramer St, Milwaukee, WI 53211				5d. PROJECT NUMBER		
				5e. TASK NUMBER		
				5f. WORK UNIT NUMBER		
7. PERFORMING ORGANIZATION NAME(S) AND ADDRESS(ES) University of Wisconsin-Milwaukee					8. PERFORMING ORGANIZATION REPORT NUMBER	
9. SPONSORING/MONITORING AGENCY NAME(S) AND ADDRESS(ES) USAF, AFRL DUNS 143574726 AF OFFICE OF SCIENTIFIC RESEARCH 875 NORTH RANDOLPH STREET, RM 3112 ARLINGTON VA 22203					10. SPONSOR/MONITOR'S ACRONYM(S)	
					11. SPONSOR/MONITOR'S REPORT NUMBER(S)	
12. DISTRIBUTION/AVAILABILITY STATEMENT Approved for public release; Distribution is unlimited						
13. SUPPLEMENTARY NOTES author's email: mafi@unm.edu						
14. ABSTRACT The main objective of the proposed research has been to investigate the proper integration of large-core graded-index multimode fibers (GIMFs) in ultrafast mode-locked fiber lasers to dramatically increase the pulse energy. Detailed theoretical investigations are aimed equally at developing a fundamental understanding of pulse propagation in GIMFs, as well as providing key opportunities to enhance the performance of ultrafast mode-locked fiber lasers.						
15. SUBJECT TERMS fiber nonlinear optics, four-wave mixing, optical fibers, graded-index multimode fibers, nonlinear switching, waveguides, mode-locked fiber lasers, ultra-short pulse fiber lasers						
16. SECURITY CLASSIFICATION OF:			17. LIMITATION OF ABSTRACT UU	18. NUMBER OF PAGES 59	19a. NAME OF RESPONSIBLE PERSON Arash Mafi	
a. REPORT unclassified	b. ABSTRACT unclassified	c. THIS PAGE unclassified			19b. TELEPHONE NUMBER (Include area code) (505) 272-7942	

ATTN: Dr. Arje Nachman
Program Manager, Electromagnetics
Physics and Electronics Directorate
The Air Force Office of Scientific Research
Award FA9550-12-1-0329

Final Report on:
**Nonlinear High-Energy Pulse Propagation in Graded-Index Multimode Optical Fibers for
Mode-Locked Fiber Lasers**

Arash Mafi
Associate Professor
Department of Physics & Astronomy
Optical Science and Engineering
Center for High Technology Materials
University of New Mexico
(505) 272-7942
<http://physics.unm.edu/mafi/>
mafi@unm.edu

This research was carried out at the University of Wisconsin-Milwaukee, PI Mafi's former university.

Outline

1 Introduction

2 Research outline

- 2.1 Preliminary analysis of nonlinear light propagation in GIMFs*
- 2.2 Nonlinear switching based on multimodal interference*
- 2.3 Why is the switching power so high? The case for multicore fibers*
- 2.4 How many cores are optimal for nonlinear switching in multicore fibers?*
- 2.5 Concentric ring core fiber for nonlinear switching*
- 2.6 Multicore design guidelines*
- 2.7 Extreme Raman cascade generation from 523 to 1750 nm using a GIMF*

3 Upcoming results in the near future

- 2.6 Multicore design guidelines*
- 3.1 Four-wave mixing in graded-index multimode fibers*
- 3.2 Experimental verification*

4 Key Personnel

5 Journal and conference publications resulting from this award

1 Introduction

The main objective of the proposed research has been to investigate the proper integration of large-core graded-index multimode fibers (GIMFs) in ultrafast mode-locked fiber lasers to dramatically increase the pulse energy. Detailed theoretical investigations are aimed equally at developing a fundamental understanding of pulse propagation in GIMFs, as well as providing key opportunities to enhance the performance of ultrafast mode-locked fiber lasers.

2 Research Outline

In the following, the main results of the research are outlined in chronological and logical order. Specifically, the rationale behind the research direction as captured in the sequence of the publications is explained.

2.1 Preliminary analysis of nonlinear light propagation in GIMFs:

In the first publication [J1], a detailed analysis of the modal properties, dispersive behavior, and nonlinear mode coupling in GIMFs were presented. A simplified form of a generalized nonlinear Schrodinger equation was derived to explore the rich nonlinear dynamics related to the propagation and interaction of light pulses in graded index multimode fibers in a tractable manner. Issues related to four-wave-mixing (FWM) in these fibers were briefly discussed, but detailed investigations on the FWM properties of GIMFs were left for future publications (see [J8]). Publication [J1] was mainly concerned with laying out the basic formalism and was meant to pave the way for future studies on detailed treatment of specific nonlinear phenomena such as self-phase modulation (SPM), cross-phase modulation (XPM), and FWM in GIMFs.

2.2 Nonlinear switching based on multimodal interference:

The results obtained in [J1] and earlier publications co-authored by the PI-Mafi showed that a multimode interferometric device based on single-mode fiber (SMF) and a multimode fiber (MMF) junctions in the form of a SMF-GIMF-SMF coupler can be used as a nonlinear switch to mode-lock fiber lasers. A similar device geometry had previously been used by PI-Mafi and collaborators to obtain ultra-low-loss coupling between two SMFs with very different mode-field diameters. In the second publication [J2], the authors presented a detailed investigation of the nonlinear multimodal interference in the SMF-GIMF-SMF coupler. The results indicated the potential application of this simple geometry for nonlinear devices, such as in nonlinear switching, optical signal processing, or as saturable absorbers in mode-locked fiber lasers. Saturable absorption in this all-fiber configuration was shown to provide attractive properties to be used in high pulse energy mode-locked fiber lasers.

2.3 Why is the switching power so high? The case for multicore fibers:

The nonlinear switching behavior presented in [J2] provided a very interesting possibility for building an in-line all-fiber nonlinear switch. However, it was observed that a much higher power was required for nonlinear-switching in multimode fibers compared to the previously reported nonlinear switching based on the nonlinear mode-coupling in multicore fibers. Moreover, the nonlinear-switching quality of the multimode fiber was shown to be inferior to those reported for multicore fibers. This prompted the team to investigate the main differences in nonlinear switching between multicore versus multimode waveguide couplers in publication [J3].

In publication [J3], it was shown that the switching power threshold in nonlinear multimode junctions was larger than in multicore junctions, mainly because the value of the modal propagation difference (supermodes in multicore fibers) was substantially larger in the former case. The XPM/FWM terms also played a role in setting the power threshold but their importance was orders of magnitude lower than that of the separation between effective propagation constants of the modes. It was shown that the injection of the right combination of the modes at the input and the collection of the right combination of the modes at the output were the main factors behind the quality of the nonlinear switching behavior. While creating the proper injection profile is often trivial in a weakly-coupled multicore waveguide, obtaining the right combination of the modes in a multimode junction is difficult, if not impossible, to achieve. Therefore, multimode junctions show lower quality nonlinear switching behavior.

2.4 How many cores are optimal for nonlinear switching in multicore fibers?

Based on the results obtained in publication [J3], the team decided that it was important to conduct a detailed investigation of the nonlinear switching behavior of multicore fibers. Several designs had been suggested and even fabricated by other research groups, but none had resulted in a robust high-quality nonlinear switching behavior. At this point, the main question for the team was whether increasing the number of the cores improved the saturable absorption characteristics of these nonlinear multi-core arrays. The team studied the saturable absorption characteristics of two-, three-, and five-core one-dimensional fiber coupler arrays and the seven-core hexagonal fiber coupler array in publication [J4]. It was shown that the performance of all these saturable absorbers were comparable and not much was gained, if anything, by going from a two-core nonlinear coupler geometry to a higher number of cores.

2.5 Concentric ring core fiber for nonlinear switching:

Previously in publication [J4], the team showed that going from a two-core fiber geometry to a higher number of cores does not improve the nonlinear switching performance of the device considerably, if any at all [7]. Hence, a two-core fiber coupler with optimized parameters seemed to be the optimum solution for a nonlinear switch. In publication [J6], the team proposed a novel concentric ring core fiber geometry as a nonlinear switch to initiate the mode-locking of the fiber lasers. This fiber has two concentric cores composed of a circular core located at the center of the fiber and a ring core placed around the central core. The main reason for choosing this geometry is its simple fabrication process. Given that conventional fibers are fabricated radially, maintaining the sensitive specifications of this fiber during the drawing process is easier than non-concentric conventional two-core fibers. Another related reason is that aligning the central core of this fiber with the SMFs in the laser cavity is much easier and more robust compared with conventional two-core geometries, especially in the presence of the inevitable variations in the fiber geometry due to the fabrication and drawing process.

2.6 Multicore design guidelines

In publication [J7], the team has reported important design rules regarding multicore nonlinear switches. The design rules will set limits on the maximum fabrication errors that are allowed for the nonlinear switching to be observed in multicore fibers.

2.7 Extreme Raman cascade generation from 523 to 1750 nm using a GIMF

Four-wave mixing in GIMFs is another nonlinear effect that has been of interest to the team, especially for the generation of new wavelengths based on multimode phase matching. In this line, it was decided to collect some experimental data on FWM in GIMFs before proceeding to explore the theory. The experimental work was conducted by a graduate student, Hamed Pourbeyram. The observations were totally surprising. The team reported in [J5] on the generation of a Raman cascade spanning the wavelength range of 523 to 1750 nm wavelength range (perhaps even higher but not measured), in a standard telecommunication graded-index multimode optical fiber. Despite the highly multimode nature of the pump, the Raman peaks were generated in specific modes of the fiber, providing substantial beam cleanup during the stimulated Raman scattering process. The observed results and the theoretical investigation that have followed [J5] clearly establish the Raman versus FWM regimes and what the conditions need to be in order to generate FWM without much Raman contamination in GIMFs. Moreover, the team has been looking at the generated Raman for various device applications, including an inexpensive tunable fiber-based light source. The green pump laser used in the experiment is available in most optics laboratories and an inexpensive commercial fiber coupled with a few other optical elements can potentially result in a very inexpensive high-power tunable light source.

3 Upcoming results

3.1 Four-wave mixing in graded-index multimode fibers

In publication [J8], general guidelines are established for the generation and observation of FWM in GIMFs. Once the theoretical work is finalized, experimental results are expected to follow.

3.2 Experimental verification

The results reported so far, especially on nonlinear switching in multimode and multicore fibers, have been followed with interest in the research community and experimental groups have contacted the team to fabricate and test some of the designs. We expect to report more on the experimental verification of the theoretical results in the future.

4 Key Personnel

The main project participants are:

- Dr. Arash Mafi, Associate Professor, Department of Physics & Astronomy, Optical Science and Engineering, Center for High Technology Materials, University of New Mexico
- Dr. Elham Nazemosadat, Postdoctoral Scholar, Electrical Engineering Department, University of Wisconsin-Milwaukee.

5 Publications Resulting from this Award

Published Peer Reviewed Journal Articles:

- J1: A. Mafi, “Pulse propagation in a short nonlinear graded-index multimode optical fiber,” **Journal of Lightwave Technology**, **30**, 2803–2811 (2012).
- J2: E. Nazemosadat and A. Mafi, “Nonlinear multimodal interference and saturable absorption using a short graded-index multimode optical fiber,” **Journal of the Optical Society of America, B**, **30**, 1357–1367 (2013).
- J3: E. Nazemosadat and A. Mafi, “Nonlinear switching in multicore versus multimode waveguide junctions for mode-locked laser applications,” **Optics Express**, **21** 30739–30745 (2013).
- J4: E. Nazemosadat and A. Mafi, “Saturable absorption in multi-core fiber couplers,” **Journal of the Optical Society of America, B**, **30**, 2787–2790 (2013).
- J5: H. Pourbeyram, G. P. Agrawal, and A. Mafi, “Stimulated Raman scattering cascade spanning the wavelength range of 523 to 1750 nm using a graded-index multimode optical fiber,” **Applied Physics Letters**, **102**, 201107 (2013).
- J6: E. Nazemosadat and A. Mafi, “Nonlinear switching in a concentric ring core chalcogenide glass optical fiber for an all-fiber passively mode-locked fiber laser,” **Optics Letters**, **9**, 4675–4678 (2014).
- J7: E. Nazemosadat and A. Mafi, “Design considerations for multi-core optical fibers in nonlinear switching and mode-locking applications,” **Journal of the Optical Society of America, B**, **31**, 1874–1878 (2014).
- J8: E. Nazemosadat and A. Mafi, “Four-wave mixing in a graded-index multimode optical fiber,” under preparation (2014).

Conference and Proceeding:

- 1. E. Nazemosadat and A. Mafi, “Saturable absorption properties of multi-core fiber arrays,” SPIE, Photonics West, San Francisco, CA (2014).
- 2. E. Nazemosadat and A. Mafi, “Mode-locking in multi-core fiber nonlinear couplers,” OSA FiO/LS 2013, Orlando, FL (2013).
- 3. S. Karbasi, E. Nazemosadat, and A. Mafi, “Enhancement of nonlinearity and phase-matching in Anderson localized 1D optical waveguides,” Nonlinear Optics (NLO), Kohala Coast, Hawaii (2013).
- 4. E. Nazemosadat, and A. Mafi, “Saturable absorption in a short graded-index multimode optical fiber using nonlinear multimodal interference,” Nonlinear Optics (NLO), Kohala Coast, Hawaii (2013).

5. H. Pourbeyram, G. Agrawal, and A. Mafi, “SRS-mediated generation of new wavelengths from 523 nm to 1750 nm in a graded-index multimode optical fiber,” CLEO, San Jose, CA (2013).

Pulse Propagation in a Short Nonlinear Graded-Index Multimode Optical Fiber

Arash Mafi, *Member, IEEE, Member, OSA*

Abstract—We present a detailed analysis of the modal properties, dispersive behavior, and nonlinear mode coupling in graded-index multimode fibers (GIMFs), and lay out a simplified form of a generalized nonlinear Schrödinger equation, which can be used to explore the rich nonlinear dynamics related to the propagation and interaction of light pulses in GIMFs in a tractable manner. We also briefly discuss an application of the presented formalism in the study of four-wave mixing in these fibers. While the reported formalism is fairly general, our presentation is mainly targeted at device applications in which short segments of GIMFs are used.

Index Terms—Fiber nonlinear optics, four-wave mixing, optical fibers.

I. INTRODUCTION

THE traditional view of multimode optical fibers (MMFs) as low-quality waveguides is gradually changing, as some researchers over the past few years have begun to view them as the new landscape of opportunities in novel applications. For example, there has been a surge of interest recently in multimode-multiplexed fiber-optic communications for ultrahigh-data-rate transmission [1]. Recently, a pioneering work on the integration of MMFs in mode-locked fiber lasers was reported; MMFs were used to reduce the total nonlinear phase shift in the fiber laser cavity in order to increase the pulse energy [2]. We also recently reported using graded-index multimode fibers (GIMFs) to build mode-field adapters and ultralow-loss couplers using the multimode interference (MMI) effect [3], [4].

While nonlinear phenomena in MMFs have been studied since the beginnings of the field of nonlinear optics [5]–[8], a systematic and comprehensive analysis of the nonlinear behavior of light propagation in multimode has been lacking. Perhaps, this can be partially blamed on the complexity of the nonlinear light propagation in MMFs. Even with only a few key dispersive and nonlinear processes governing the propagation of light in single-mode fibers (SMFs), their interplay results in such vast and rich dynamics that has been the subject of intense research over the past few decades where new phenomena are still being discovered [9]; perhaps there has been little incentive to add yet another complication to the system and cross over to the multimode side.

Conventional multimode fibers are often prohibitively complex to analyze and their rich nonlinear dynamics are buried underneath their hundreds of propagating modes and millions of nonlinear coupling terms [10]. In this paper, we will argue that GIMFs have specially interesting properties that make them an ideal platform to explore the rich nonlinear dynamics related to the propagation and interaction of multiple modes in optical fibers in a more tractable manner. In particular, we will show that the nonlinear dynamics in GIMFs can be considerably simplified for better fundamental understanding and easier control in novel device applications. Our arguments are in line with our recent work in the “linear” regime on making an ultralow-loss coupler based on MMI in GIMFs [3]. We will show that, with sufficient care, nonzero-angular-momentum modes are never excited; therefore, the nonlinear propagation dynamics can be limited to only a handful of zero-angular-momentum modes. Moreover, unlike conventional multimode fibers, all the modes in GIMFs can propagate with nearly identical group velocities at special wavelengths; therefore, nonlinear coupling among short pulses is maximally achieved all along the fiber, adding to the richness of the nonlinear dynamics.

The presence of multiple, though small number of nonlinearly coupled modes gives rise to an abundance of novel and complex nonlinear phenomena, above and beyond that of the highly interesting landscape of two-polarization-mode fibers [5]. The intention of this paper is to lay out a comprehensive formalism for the study of nonlinear light propagation in GIMFs in the scalar approximation (polarization effects are ignored). In particular, the modal properties, dispersive behavior, and nonlinear coupling terms are derived and explored in sufficient detail, paving the way for future detailed studies of nonlinear phenomena such as self-phase modulation (SPM), cross-phase modulation (XPM), and four-wave mixing (FWM) in GIMFs. While the reported formalism is fairly general, our presentation is mainly targeted at device applications in which short segments of GIMFs are used, such as those reported in [3] and [4].

Section II is primarily a review of the modal and dispersion properties of GIMFs. While most of the material presented in this section can be found in various earlier publications, our intention has been to provide a relatively self-contained manuscript with a more modern and accessible notation. We note that the modal and dispersion properties reviewed in Section II are the key ingredients which will be used to construct the equations governing the nonlinear propagation of light in GIMFs; therefore, a more detailed treatment of these parameters is warranted.

In Sections III and IV, we construct a simplified generalized nonlinear Schrödinger equation (GNLSE) for nonlinear light propagation in GIMFs. In Sections V and VI, we apply the GNLSE in a couple of specific examples, such as FWM in

Manuscript received March 12, 2012; revised May 25, 2012, June 28, 2012; accepted July 03, 2012. Date of publication July 17, 2012; date of current version August 08, 2012. This work was supported in part by the UWM Research Growth Initiative Grant and in part by the Air Force Office of Scientific Research under Grant FA9550-12-1-0329.

The author is with the Department of Electrical Engineering and Computer Science, University of Wisconsin-Milwaukee, Milwaukee, WI 53211 USA (e-mail mafi@uwm.edu).

Digital Object Identifier 10.1109/JLT.2012.2208215

GIMFs, and conclude in Section VII. Some issues related to mode coupling and excitation of nonzero-angular-momentum modes are briefly discussed in the Appendix.

II. BRIEF OVERVIEW OF GIMFs

In this section, we present a brief overview of GIMFs and establish the notation that will be used in the rest of this paper [11]. The refractive index profile of a GIMF is given by

$$n^2(\rho) = n_0^2 \left[1 - 2\Delta \left(\frac{\rho}{R} \right)^\alpha \right], \quad \rho \leq R$$

$$= n_0^2(1 - 2\Delta), \quad \rho > R \quad (1)$$

where R is the core radius, n_0 is the maximum refractive index in the center of the core, Δ is the relative index step, and $\alpha \approx 2$ characterizes a near parabolic-index profile. The transverse electric field of a propagating mode can be decomposed into separate radial and angular components as

$$E_{p,m}(\rho, \phi) = \tilde{E}_{p,m}(\rho) e^{im\phi} \quad (2)$$

where [12]

$$\tilde{E}_{p,m}(\rho) = A_p^m \frac{\rho^{|m|}}{\rho_0^{|m|+1}} \exp\left(-\frac{\rho^2}{2\rho_0^2}\right) L_p^{|m|}\left(\frac{\rho^2}{\rho_0^2}\right) \quad (3)$$

and

$$\rho_0 = \frac{R}{(4N_2)^{1/4}}, \quad A_p^m = \sqrt{\frac{p!}{\pi(p+|m|)!}}. \quad (4)$$

$L_p^{|m|}$ is the generalized Laguerre polynomial. Here, each mode is labeled by two integers, p and m , referred to as the radial and angular numbers, respectively. The coefficients in the field profile in (3) are chosen such that the fields are orthonormal according to

$$\int_0^{2\pi} d\phi \int_0^\infty \rho d\rho E_{p',m'}^*(\rho, \phi) E_{p,m}(\rho, \phi) = \delta_{pp'} \delta_{mm'}. \quad (5)$$

The total number of guided modes (counting the polarization degeneracy) is given as

$$N_\alpha = \frac{\alpha}{\alpha + 2} n_0^2 k^2 R^2 \Delta \quad (6)$$

where N_2 in (3) is also given by (6), and $k = 2\pi/\lambda$.

The near parabolic shape of the refractive index profile in (1) is due to the near parabolic Germanium (Ge) doping concentration d in the core of the GIMF

$$d(\rho) = d_0 \left[1 - \left(\frac{\rho}{R} \right)^\alpha \right], \quad \rho \leq R$$

$$= 0, \quad \rho > R \quad (7)$$

where d_0 is the maximum doping in weight percentage (wt%) at the center of the core. At each given value of Ge doping concentration, the refractive index can be accurately described by a fit to the Sellmeier equation, where the Sellmeier coefficients

depend on the Ge doping concentration. In particular, the Sellmeier coefficients are available in [13] and [14] for pure fused silica (refractive index represented as $n_{\text{si}}(\lambda)$), and Ge-doped fused silica with a Ge doping concentration of 6.3-wt% (refractive index represented as $n_{6.3}(\lambda)$). Here, we have implicitly assumed that the refractive index of the Ge-doped fused silica increases linearly with the Ge doping concentration and we have already relied on this assumption to relate (1) and (7). This is a reasonable approximation, which is also supported by experimental measurements [15]. Therefore, we derive a generalized Sellmeier equation to incorporate the dependence of the refractive index on both the wavelength and Ge doping concentration of fused silica as

$$n^2(\lambda, d) = n_{\text{si}}^2(\lambda) + \frac{d}{6.3} [n_{6.3}^2(\lambda) - n_{\text{si}}^2(\lambda)] \quad (8)$$

where d is again the Ge doping concentration in wt%. The utility of (8) is that it provides, along with (1) and (7), a reliable estimate of the refractive index for a broad wavelength span from near-ultraviolet through mid-infrared region for common levels of Ge doping concentration in GIMFs.

All the modes with equal group mode number $g = 2p + |m| + 1$ are almost degenerate in the value of the propagation constant, which is given according to the formula:

$$\beta_g = n_0 k (1 - 2\Delta x)^{1/2} \quad (9)$$

where

$$x = \left(\frac{g}{\sqrt{N_\alpha}} \right)^{2\alpha/(\alpha+2)}. \quad (10)$$

The group velocity of the modes in mode group number g is given by

$$v_g^{\text{gr}} = \left(\beta_g^{(1)} \right)^{-1} = (\partial_k \beta_g)^{-1} \quad (11)$$

where β_g defined in (9). After a few algebraic steps, one can show that

$$\beta_g^{(1)} = \frac{n_0^{\text{gr}}}{c} \left(1 - \frac{y+4}{\alpha+2} \Delta x \right) (1 - 2\Delta x)^{-1/2} \quad (12)$$

where $n_0^{\text{gr}} = \partial_k(n_0 k)$ is the group index at the center of the core, c is the speed of light in vacuum, and y is defined as [13], [16]

$$y = 2 \frac{n_0}{n_0^{\text{gr}}} \frac{k}{\Delta} \frac{\partial \Delta}{\partial k}. \quad (13)$$

There are three important points of caution regarding the use of analytical equations presented previously. The first point is that (3) is only strictly valid for $\alpha = 2$; however, the deviations are small and (3) is often very reliable. The second point is that (3) is only a solution of Maxwell's equations in the core of the fiber and must be matched to an exponentially decaying modified Bessel function of the second kind in the cladding. In calculating the overlap integrals for coupling in and out of the GIMF,

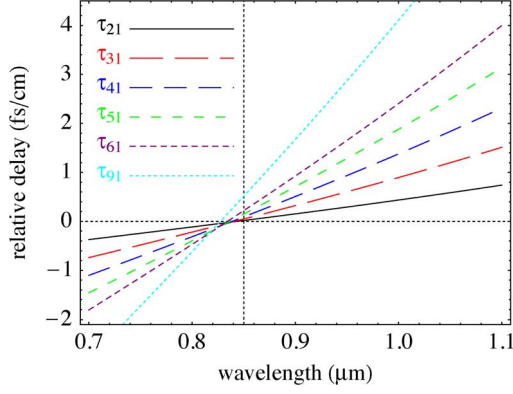


Fig. 1. Relative delays $\tau_{g1} = \beta_g^{(1)} - \beta_1^{(1)}$ (delay relative to mode group $g = 1$) are plotted as a function of the wavelength for different mode groups.

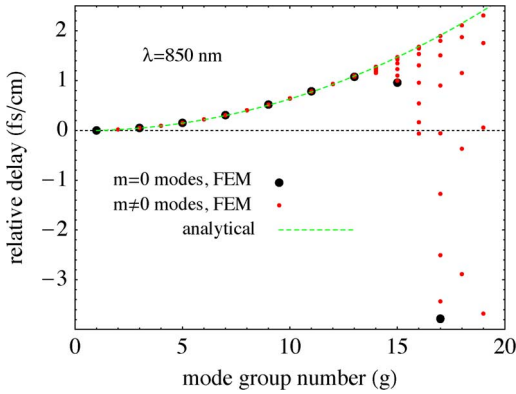


Fig. 2. Relative delay is plotted at $\lambda = 850$ nm for all the modes in a GIMF. The horizontal axis represents the mode group number g and the dots represent the values of relative delay calculated using the FEM, where the cladding effect is now taken into account. The large black dots are for $m = 0$ modes, the small red dots belong to $m \neq 0$ modes, and the green dashed line represents the analytical expression from (12).

as long as the beam diameters of the in-coupling and out-coupling “often”-Gaussian fields are smaller than the core diameter of the GIMF, it is perfectly fine to use (3). For larger in-coupling beam diameters, the use of (3) can still be at least qualitatively valid. In such cases, better accuracy can be achieved if the cladding profile is properly accounted for, for example by using a numerical solver. In either case, small adjustments in the normalization coefficients of (3) are expected according to (5) in order to compensate for substituting (3) for the modified Bessel function of the second kind in the cladding. The third point is that the presence of the cladding removes the degeneracy among modes within a mode group, both in the propagation constant and the group velocity. While this effect is generally quite small, it is more pronounced for higher order mode groups, which have a larger overlap with the cladding. Numerical examples of this last point are explored later in Figs. 2 and 3.

A. Optimum Value of α

The optimum value of α is often chosen to minimize the multimode dispersion in an optical fiber communication link at a specific wavelength. Olshansky and Keck [16] have derived a

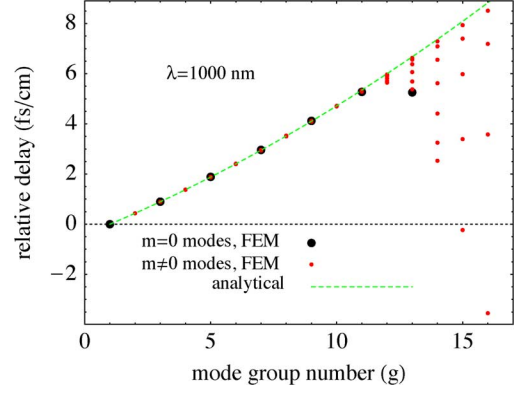


Fig. 3. Same as Fig. 2 except at $\lambda = 1000$ nm.

compact formula for the pulse dispersion in GIMFs and have shown that the minimum pulse dispersion occurs for

$$\alpha_{\text{opt}} = 2 + y - \Delta \frac{(4 + y)(3 + y)}{(5 + 2y)}. \quad (14)$$

While the optimum value of α from (14) is a classic result and is often quoted as the optimal design point for high-bandwidth GIMFs, it may not be suitable for most modern multimode optical communication systems. The key assumption in the derivation of α_{opt} by [16] is the equipartition of the power among all the guided modes. However, this assumption heavily favors the higher order mode groups, because higher order mode groups have a larger mode count and carry a larger share of the total power in this formulation. In modern multimode optical communication systems where laser transmitter sources are commonly used, lower mode groups often carry a larger share of the total power and GIMFs designed based on (14) result in low bandwidth.

In practice, for a typical untilted center-launch of a Gaussian-beam laser, zero-angular-momentum modes ($m = 0$) are predominantly excited and mode groups $g = 1$ and $g = 3$ carry the largest portion of the power. Therefore, a more appropriate choice of α_{opt} can be expressed as $\beta_{g=1}^{(1)} = \beta_{g=3}^{(1)}$, or even $\partial_g \beta_g^{(1)}|_{g=1} = 0$. We note that the actual value of α in high-bandwidth commercial GIMFs is proprietary and is also subject to variations in the manufacturing process. However, because $\alpha_{\text{opt}} = 2 + y$ provides a better modal delay balance among the lower order mode groups than (14) as is required in a typical laser launch, we speculate that it is a more accurate representation of the refractive index profile in high-bandwidth commercial GIMFs and we will adopt $\alpha_{\text{opt}} = 2 + y$ throughout this paper.

B. Dispersion Properties of a Conventional GIMF

Conventional high-bandwidth commercial-grade GIMFs such as Corning's InfiniCor eSX+ are commonly optimized for high-bandwidth performance at 850-nm wavelength. The typical core radius $R = 25 \mu\text{m}$ and the maximum Ge-doping is given by $d_0 \approx 10.8$. At $\lambda = 850$ nm, this results in $\alpha = 2.103$, $n_0 = 1.4676$, $\Delta = 0.01$, and $\text{NA} = 0.208$, where NA is the numerical aperture. We reiterate that the exact values of

the aforementioned parameters are often proprietary, but it is relatively easy to speculate on the values of these parameters from the published specifications of these fibers (R and NA), and the preceding analysis. In order to carry out specific numerical analysis in this paper, we choose the aforementioned typical parameters, which must be reasonably close to those of Corning's InfiniCor eSX+ or Thorlab's GIF50, and refer to this fiber as the conventional GIMF (C-GIMF) throughout this paper. All the numerical results in this paper are presented for C-GIMF.

In Fig. 1, we plot the relative delay $\tau_{g1} = \beta_g^{(1)} - \beta_1^{(1)}$ (delay relative to mode group $g = 1$), as a function of the wavelength for different mode groups. We observe that at around $\lambda = 850$ nm where the fiber bandwidth was optimized (by choosing $\alpha = 2 + y$ where y is determined at $\lambda = 850$ nm), the relative delay is very small and all mode groups propagate (approximately) with the same group velocity. However, for higher mode groups such as $g = 9$, τ_{91} is noticeably larger (0.51 fs/cm) compared with the delay experienced by lower order mode groups (e.g., $\tau_{21} = 0.018$ fs/cm). As we pointed out before, such high-order mode groups are excited less efficiently in most modern multimode optical communication systems and optimal values of α should not be chosen based on (14), which gives a high weight to such high-order mode groups. In Fig. 1, it is clear that at wavelengths substantially apart from $\lambda = 850$ nm, the modal group velocities are not longer balanced, but are "almost" equally spaced. For example, at $\lambda = 1.0$ μm , $\tau_{21} = 0.436$ fs/cm and $\tau_{31} = 0.896$ fs/cm.

Earlier, we cautioned that the presence of the cladding removes the degeneracy of the delays among modes within each mode group. In Fig. 2, we plot the relative delay at $\lambda = 850$ nm for all the modes in a GIMF. The horizontal axis represents the mode group number g and the dots represent the values of relative delay calculated using the finite element method (FEM) of [17], where the cladding effect is now taken into account. The large black dots are for zero-angular-momentum modes $m = 0$, the small red dots belong to $m \neq 0$ modes, and the numerical values of the delay are compared with the analytical expression from (12) plotted in the green dashed line. The impact of the cladding on lifting the degeneracy among modes in higher mode groups is more pronounced, as expected. In Fig. 3, we make a similar plot, except at $\lambda = 1000$ nm, where we observe similar features. As expected, the delays are much less balanced among the mode groups for $\lambda = 1000$ nm compared with $\lambda = 850$ nm. In this paper, as we will discuss later, we are primarily interested in zero-angular-momentum modes ($m = 0$), and Figs. 2 and 3 clearly illustrate the adequacy of analytical expression (12) for $g \leq 11$. Figs. 2 and 3 are quite useful in estimating the nonlinear modal interaction length between different mode groups, which is limited by the group velocity mismatch-induced walk-off. For example, from Fig. 3, at $\lambda = 1000$ nm, the relative delay between $g = 1$ and $g = 3$ mode groups (consecutive groups with $m = 0$ modes) is $\tau_{31} = 0.896$ fs/cm. Therefore, after 1 m of propagation, the pulse walk-off is around 90 fs, resulting in very low efficiency interaction between pulses with duration shorter than 100 fs. However, at $\lambda = 850$ nm, the pulse walk-off is quite smaller. It must be noted that these are crude but relevant approximations and one must include such effects as nonlinear

trapping in order to obtain a more reliable estimate of the true modal nonlinear interaction length.

Finally, GVD for mode group $g = 1$ (i.e., $\beta_1^{(2)}$) is plotted as a function of the wavelength. GVD does not appreciably differ among mode groups and is taken to be the same for all modes in this paper. The dashed lines identify the point of zero GVD.

C. Approximate Form for the Propagation Constant β_g

It is sometimes more convenient to adopt a simplified version of (9), when possible. For $\Delta \ll 1$, we can write

$$\beta_g \approx n_0 k \left(1 - \Delta x - \frac{\Delta^2 x^2}{2} \right) + O(\Delta^3). \quad (15)$$

The $O(\Delta^2)$ term can be ignored relative to the $O(\Delta)$ term for short propagation lengths where it does not amount to substantial "extra" phase mismatch between different mode groups. For example, the $O(\Delta^2)$ phase mismatch between $g = 1$ and $g = 3$ mode groups (consecutive groups with $m = 0$ modes) is given by

$$\delta\phi_{3,1} \approx \frac{8\Delta L}{n_0 k R^2} \quad (16)$$

where $\alpha \approx 2$ is assumed for simplicity and L is the length of the GIMF. Therefore, the $O(\Delta^2)$ term contributes a 2π additional phase if the length of the GIMF is $L_{2\pi} = \pi n_0 k R^2 / (4\Delta)$. For the typical design parameters of conventional commercial-grade GIMFs at $\lambda = 850$ nm, $L_{2\pi} \approx 54$ cm; therefore, in order to reliably ignore the $O(\Delta^2)$ term, the length of the GIMF must be considerably shorter than $L_{2\pi}$. We note that $L_{2\pi}$ is even shorter if calculated with higher order mode groups. In situations where the $O(\Delta^2)$ term can be ignored and $\alpha \approx 2$ can be trusted, (15) transforms into a particularly useful form of linear in g :

$$\beta_g = n_0 k_0 - \frac{\sqrt{2\Delta}}{R} g. \quad (17)$$

III. PULSE PROPAGATION IN A NONLINEAR MMF

In this section, we briefly review the basic formulation of the nonlinear pulse propagation in a MMF, as presented by Poletti and Horak [10]. Their approach is based on the pioneering work of Kolesik and Moloney [18]. In the next section, we will adapt this formulation to the specific case of the nonlinear pulse propagation in a GIMF.

While the formulation presented in [10] includes the polarization effects, we assume in this paper that the fields are excited and remain in the \hat{x} -linear polarization. This simplifying assumption should be valid based on our experience from the nonlinear pulse propagation in SMFs [5]. Essentially, all the nonpolarization-related phenomena in fiber optics can still be observed. While the polarization effects can also be easily included, the resulting equation is unnecessarily complicated for the purposes of this paper, which is focused on the multi(spatial)-mode-related behavior of the nonlinear propagation.

The modal decomposition of the (scalar) electric field into a sum of mode function $F_p(x, y, \omega)$ with envelopes $A_p(z, \omega)$ is given by

$$E(x, y, z, t) = \frac{1}{2} \sum_p \int d\omega \left\{ \frac{F_p(x, y, \omega)}{N_p(\omega)} A_p(z, \omega) \right. \\ \left. \times \exp [i(\beta_p(\omega)z - \omega t)] + \text{c.c} \right\} \quad (18)$$

where the field normalization constant $N_p(\omega)$ is chosen such that the mode profile satisfies the normalization and orthogonality condition

$$\int dx dy F_p^*(x, y, \omega) F_q(x, y, \omega) = \delta_{pq} \quad (19)$$

and $|A_p(z, t)|^2$ represents the optical power, where $A_p(z, t)$ is the Fourier transform of $A_p(z, \omega)$.

Poletti and Horak [10] have shown that the GNLSE for pulse propagation in multimode fibers can be written as

$$\begin{aligned} & \frac{\partial A_p(z, t)}{\partial z} \\ &= i \left(\beta_0^{(p)} - \beta_0^{(0)} \right) A_p(z, t) \\ & - \left(\beta_1^{(p)} - \beta_1^{(0)} \right) \frac{\partial A_p(z, t)}{\partial t} \\ & + i \sum_{n \geq 2} \frac{\beta_n^{(p)}}{n!} \left(i \frac{\partial}{\partial t} \right)^n A_p(z, t) \\ & + i \frac{n_2 \omega_0}{c} \sum_{l, m, n} \left\{ \left(1 + i \tau_{plmn}^{(1)} \frac{\partial}{\partial t} \right) Q_{plmn}^{(1)}(\omega_0) P_{lmn}^{(1)} \right. \\ & \left. + \left(1 + i \tau_{plmn}^{(2)} \frac{\partial}{\partial t} \right) Q_{plmn}^{(2)}(\omega_0) P_{lmn}^{(2)} \right\} \end{aligned} \quad (20)$$

where ω_0 is taken as the carrier frequency of the initial pulse. The nonlinear field terms are given by

$$\begin{aligned} P_{lmn}^{(1)} &= 2A_l(z, t) \int d\tau R(\tau) A_m(z, t - \tau) A_n^*(z, t - \tau) \quad (21) \\ P_{lmn}^{(2)} &= A_l^*(z, t) \int d\tau R(\tau) A_m(z, t - \tau) A_n(z, t - \tau) e^{2i\omega_0 \tau} \end{aligned}$$

and the nonlinear coupling terms are given by

$$\begin{aligned} Q_{plmn}^{(1)}(\omega) &= \frac{1}{3} \int dx dy F_p^*(\omega) F_l(\omega) F_m(\omega) F_n^*(\omega) \quad (22) \\ Q_{plmn}^{(2)}(\omega) &= \frac{1}{3} \int dx dy F_p^*(\omega) F_l^*(\omega) F_m(\omega) F_n(\omega). \end{aligned}$$

The nonlinear response function can be written as

$$R(\tau) = (1 - f_R) \delta(\tau) + f_R h(\tau) \quad (23)$$

where $f_R \approx 0.18$ is the fractional contribution of the Raman response to the total nonlinearity and $h(\tau)$ is the delayed Raman response function [5]. The shock time constants are given by

$$\tau_{plmn}^{(1,2)} = \frac{1}{\omega_0} + \left\{ \frac{\partial}{\partial \omega} \ln [Q_{plmn}^{(1,2)}(\omega)] \right\}_{\omega_0}. \quad (24)$$

IV. NONLINEAR PULSE PROPAGATION IN A GIMF

The GNLSE (20) is our starting point to construct a suitable equation for the nonlinear pulse propagation in a GIMF. A

conventional commercial-grade GIMF supports more than 100 modes. The nonlinear mode propagation can turn into a hopeless numerical integration of more than 100 coupled NLSEs, each with more than one million nonlinear coupling terms. While symmetry arguments can somewhat reduce the number of nonlinear coupling terms in cylindrically symmetric optical fibers as shown in [10], the large number of modes and coupling terms can easily bury the interesting physical phenomena and especially make it difficult to use the observations in a simple form for device application; therefore, we desire to restrict our study to a small and manageable subspace of modes in a consistent manner. Fortunately, not only is this possible in GIMFs, it is in fact a practical and preferred choice [3]. In this paper, we limit our formulation and studies only to the case of $m = 0$ or zero-angular-momentum modes. This choice of a limited subspace is very reasonable and desired, because the injected pulse is often coming either from the SMF, which is fusion-spliced to the GIMF, or from a similar azimuthally symmetric launch. The experimental evidence presented in our recent work in [3] confirms the reliability of this choice.

It is very important to note that in the nonlinear case, it can be shown that the conservation of angular momentum, dictated by the symmetries of $Q_{plmn}^{(1,2)}$ in (20) and (22), prevents the excitation of any modes with $m \neq 0$ along the fiber from only $m = 0$ modes; therefore, we can safely limit our analysis to the small and manageable zero-angular-momentum subset of modes. We note that $m \neq 0$ modes may still be excited because of the imperfection in the optical fiber. This coupling can be controlled and minimized in short fiber segments. Later in the Appendix, we will briefly discuss some of the issues related to the coupling among modes and excitation of $m \neq 0$ modes, especially in the context of macrobending.

The $m = 0$ modes of the GIMF can be read directly from (1), (3), and (4), where we have

$$\begin{aligned} F_p(\omega) &= E_{p,0}(\rho, \phi; \omega) \\ &= \frac{1}{\sqrt{\pi \rho_0^2}} \exp \left(-\frac{\rho^2}{2\rho_0^2} \right) L_p \left(\frac{\rho^2}{\rho_0^2} \right). \end{aligned} \quad (25)$$

L_p is the Laguerre polynomial, which is simply the generalized Laguerre polynomial with zero angular momentum. After a few simple algebraic steps, we can show that

$$\begin{aligned} Q_{plmn}(\omega) &= Q_{plmn}^{(1)}(\omega) = Q_{plmn}^{(2)}(\omega) \\ &= \frac{1}{3} \frac{1}{\pi \rho_0^2} \int_0^\infty du e^{-2u} L_p(u) L_l(u) L_m(u) L_n(u). \end{aligned} \quad (26)$$

From (26), we can readily calculate the nonlinear coupling among $m = 0$ modes propagating in a GIMF. In particular, for the lowest order mode, we obtain

$$Q_{0000}(\omega) = \frac{1}{3} \frac{1}{2\pi \rho_0^2} = \frac{1}{3} \frac{1}{A_{\text{eff}}^0}. \quad (27)$$

We note that $\rho_c = \sqrt{2} \rho_0$ is simply the modal radius of this lowest order mode and is the key spatial dimension in a GIMF that sets all its modal properties, not the core radius R [3]. Specifically, $\rho_c \propto \sqrt{\lambda R}$ and therefore, the effective area for

the lowest order mode $A_{\text{eff}}^0 = \pi \rho_c^2$ scales as the core radius, not as the core area as one might have reasonably imagined. The scaling of the modal area with the square root of the core area has important consequences for nonlinear pulse propagation in GIMFs. For example, unlike the single-mode fibers, where doubling the core area reduces the effective nonlinearity by a factor of 2, the effective nonlinearity of each mode is only reduced by a factor of $\sqrt{2}$ in GIMFs.

We can define the nonlinear coupling coefficient in GIMFs as

$$\gamma_{plmn} = 3 \frac{n_2 \omega_0}{c} Q_{plmn}(\omega). \quad (28)$$

We note that the forms of the diagonal terms γ_{pppp} agree with the conventional formulation often presented for the SMF and are inversely proportional to the modal area of that particular mode [5]. In particular, for the lowest order mode (LP₀₁-like and often the most important mode), we can use (26)–(28) to show that

$$\gamma = \gamma_{0000} = \frac{n_2 \omega_0}{A_{\text{eff}}^0}. \quad (29)$$

As shown in (29), we will simply use γ instead of γ_{0000} in the rest of this paper.

As a numerical example, we consider that the value of γ for a typical GIMF, such as GIF50, which was studied in [3], is approximately 3.6 times lower than that of a typical SMF-28, given that $\rho_c \approx 7.73 \mu\text{m}$ for GIF50 at $\lambda = 1550 \text{ nm}$. The value of γ increases at shorter wavelengths and becomes larger than 1.2/W.km at $\lambda \approx 1.0 \mu\text{m}$ (comparable to that of SMF-28 at $\lambda = 1550 \text{ nm}$).

Finally, in an attempt to further simplify our notation, we defined $\eta_{plmn} = \gamma_{plmn}/\gamma$ with $\eta_{0000} = 1$. We note that η_{plmn} is a fully symmetric tensor and represents the nonlinear coupling among propagating modes in a GIMF. Here, for reference, we calculate the nonlinear coupling terms among the three lowest order modes in GIMFs

$$\begin{aligned} \eta_{0001} &= \eta_{0011} = \eta_{1111} = \frac{1}{2}, & \eta_{0012} &= \eta_{0022} = \frac{3}{8} \\ \eta_{0002} &= \eta_{0111} = \eta_{0112} = \eta_{1112} = \frac{1}{4}, & \eta_{2222} &= \frac{11}{32} \\ \eta_{1122} &= \frac{5}{16}, & \eta_{0122} &= \frac{3}{16} \\ \eta_{1222} &= \frac{11}{64}, & \eta_{0222} &= \frac{5}{32}. \end{aligned} \quad (30)$$

These simplifications allow us to rewrite the GNLSE (31) in a more compact form

$$\begin{aligned} \frac{\partial A_p(z, t)}{\partial z} &= i \delta \beta_0^{(p)} A_p(z, t) - \delta \beta_1^{(p)} \frac{\partial A_p(z, t)}{\partial t} \\ &+ i \sum_{n \geq 2} \frac{\beta_n^{(p)}}{n!} \left(i \frac{\partial}{\partial t} \right)^n A_p(z, t) \\ &+ i \frac{\gamma}{3} \sum_{l, m, n} \left\{ \eta_{plmn} \left(1 + i \tau_{plmn} \frac{\partial}{\partial t} \right) \right. \\ &\quad \left. \times \left[P_{lmn}^{(1)} + P_{lmn}^{(2)} \right] \right\} \end{aligned} \quad (31)$$

where $\delta \beta_0^{(p)} = \beta_0^{(p)} - \beta_0^{(0)}$ and $\delta \beta_1^{(p)} = \beta_1^{(p)} - \beta_1^{(0)}$. A final and perhaps major simplification is possible if the delayed Raman response and the shock terms are ignored. In that case, the last line (nonlinear coupling terms) in (31) can be simplified as

$$i \gamma \sum_{l, m, n} \eta_{plmn} A_l(z, t) A_m(z, t) A_n^*(z, t). \quad (32)$$

In what follows, we will use (31) as our starting point to analyze the linear and nonlinear propagation of optical pulses in GIMFs. We will also ignore the delayed Raman response and the shock terms and, therefore, adopt the approximation presented in (32). The impact of the delayed Raman response and the shock terms will be addressed elsewhere in the future.

V. MMI IN GIMFs

Perhaps, the most trivial application of the GNLSE (31) is to the MMI in GIMFs as discussed in detail in [3] and [4]. We consider low-power constant wave (CW) light propagation where both temporal and nonlinear dynamics can be ignored and obtain

$$A_p(z) = A_p(0) \exp \left[i \delta \beta_0^{(p)} z \right]. \quad (33)$$

In [3] and [4], we assumed that the injected beam is in the form of a Gaussian with radius w , centrally aligned with the GIMF, and expressed as

$$|w\rangle = \sqrt{\frac{2}{\pi w^2}} \exp \left(-\frac{\rho^2}{w^2} \right) \quad (34)$$

where $\langle w|w\rangle = 1$ and the bra-ket notation indicates integration in the transverse ($\rho - \phi$) coordinates. The injected beam can be easily realized from the nearly Gaussian mode of an SMF to the GIMF. The initial excitation amplitudes are given by $A_p(0) = P_0^{1/2} \langle F_p|w\rangle$, where P_0 is the power of the input Gaussian field and $|F_p\rangle$ is given in (25). We also have

$$\langle F_p|w\rangle = \frac{\sqrt{4\eta}}{\eta + 1} \Psi^p, \quad \eta = \frac{\rho_c^2}{w^2}, \quad \Psi = \frac{\eta - 1}{\eta + 1}. \quad (35)$$

In particular, in [3], we assumed that the output port of the GIMF is spliced to another SMF with a mode-field radius of w' . If P'_0 is the power carried by the out-coupling SMF, the power coupling efficiency P'_0/P_0 between the in-coupling and out-coupling SMFs can be written as

$$\tau(z) = \frac{P'_0}{P_0} = \left| \sum_{p=0}^{P-1} \langle w'|F_p\rangle \langle F_p|w\rangle e^{i \delta \beta_0^{(p)} z} \right|^2. \quad (36)$$

Therefore, we get

$$\tau(z) = \frac{16\eta\eta'}{(\eta + 1)^2(\eta' + 1)^2} \left| \sum_{p=0}^{P-1} \Psi^p \Psi'^p e^{i \delta \beta_0^{(p)} z} \right|^2. \quad (37)$$

For $m = 0$ modes ($g = 2p + 1$), from (17) we have

$$\beta_p = n_0 k_0 - (2p + 1)\pi/Z \iff \delta \beta_0^{(p)} = -2\pi p/Z \quad (38)$$

where $Z = \pi R/\sqrt{2\Delta}$. If we use (38) in (37), we obtain the result presented in (12) of [3].

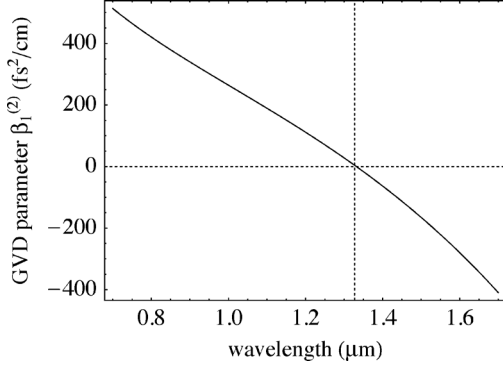


Fig. 4. GVD for mode group $g = 1$ is plotted as a function of the wavelength. GVD does not appreciably differ among different modes and can usually be taken to be the same for all modes.

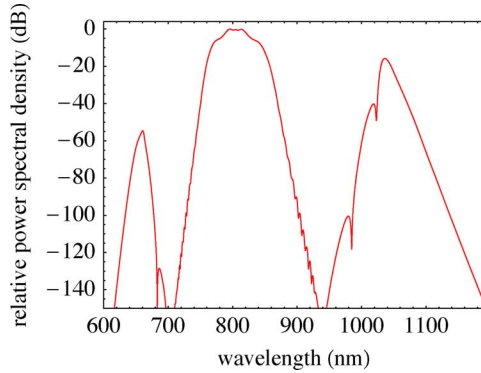


Fig. 5. Relative power spectral density for the lowest order mode in GIMF after 0.1 m of propagation in the C-GIMF. The injected pulses are each 57 fs long, with 200 kW peak power at $\lambda_P = 805$ nm and 1 kW peak power at $\lambda_S = 1030$ nm. In addition to the expected spectral broadening, the FWM generation of a new peak centered at $\lambda_A = 660$ nm is notable.

VI. NEW WAVELENGTH GENERATION VIA FWM

In the previous section, we used the GNLSE (31) to explore a MMI problem in the absence of both dispersive and nonlinear effects for low-power CW light propagation in GIMFs. In this section, we briefly review an antipodal application of the GNLSE (31) for short pulse propagation with high peak power. In particular, we will observe conversion of the pump light to other wavelengths via multimode phase-matched FWM in GIMF.

In the first numerical experiment, we launch an unchirped pulse of the form $\text{sech}(t/T_0)$ with $T_0 = 57$ fs and peak power $P_0 = 200$ kW at $\lambda_P = 805$ nm in a C-GIMF segment in the lowest order mode $(p, m) = (0, 0)$; this pulse can be obtained from a typical titanium-sapphire mode-locked laser. A much weaker pulse with peak power 1 kW and the same duration at $\lambda_S = 1030$ nm is also launched into the same mode of the GIMF; this pulse can be obtained from a typical Yb-doped mode-locked fiber laser. Fig. 5 shows the “relative” power spectral density for the lowest order mode after propagating a length of 0.1 m in the C-GIMF. We note that in our simulations, we have assumed $\gamma \approx 1.0/\text{W}\cdot\text{km}$ (typical value obtained for fused Silica at this wavelength from (29) for C-GIMF), which results in a nonlinear length $L_{NL} = 1/\gamma P_0 \approx 5$ mm. In addition to the expected spectral broadening at $\lambda_P = 805$ nm due to dispersive

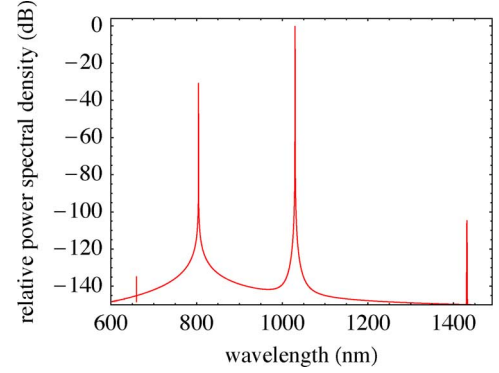


Fig. 6. Relative power spectral density for the lowest order mode in GIMF after 0.1 m of propagation in the C-GIMF. The injected pulses are each 5.6 ps long, with 1 kW peak power at $\lambda_S = 1030$ nm and 1 W peak power at $\lambda_P = 805$ nm. The FWM generation of a new peak centered at $\lambda_A = 660$ nm is notable.

and nonlinear SPM effects, the generation of a new peak centered at $\lambda_A = 660$ nm is notable. The conversion of light from λ_P and λ_S to λ_A is mediated by a FWM process where

$$2\omega_P = \omega_S + \omega_A \quad (39)$$

where $\omega_P = 2\pi c/\lambda_P$ and so on, and

$$2\beta_1(\lambda_P) = \beta_1(\lambda_S) + \beta_3(\lambda_A) \quad (40)$$

where $\beta_1(\lambda_P)$ is the propagation constant of the lowest order mode at the pump wavelength λ_P ($p = 0$ or $g = 1$ where according to (9) g is used as a lower index for β), $\beta_1(\lambda_S)$ is the propagation constant of the lowest order mode at the Stokes wavelength λ_S , and $\beta_3(\lambda_A)$ is the propagation constant of the next-order mode at the anti-Stokes wavelength λ_A ($p = 1$ gives $g = 3$ for the index of β). We note that the FWM process in GIMFs was experimentally observed in 1981 by Hill *et al.* [19]; using the formalism presented in this paper, we can explore the efficiency of such processes by numerically solving the GNLSE (31). We would like to point out that the required phase matching presented in (40) involves different modes of the GIMF, as also observed experimentally in [19]. A more comprehensive treatment of the FWM process in GIMFs is beyond the scope of this paper and will be presented elsewhere. The analysis presented in this section is merely intended to show the applicability of the GNLSE (31) to explore the diverse and rich linear, dispersive, and nonlinear phenomena that can occur due to the subtle interaction of the propagating modes in GIMFs. We note that all the features observed in Fig. 5 (and also in Fig. 6) relate only to the nonlinear interactions between $(m = 0, p = 0)$ and $(m = 0, p = 1)$ modes.

Before we close this section, we explore a similar example, though with much longer pulses and lower values of peak power. Here, we launch a much longer unchirped pulse with $T_0 = 5.7$ ps and peak power $P_0 = 1$ kW at $\lambda_P = 1030$ nm and a much weaker pulse with peak power 1 W and the same duration at $\lambda_S = 805$ nm, both into the lowest order mode of the GIMF. Fig. 6 shows the “relative” power spectral density for the lowest order mode after propagating a length of 0.1 m in the GIMF. The nonlinear length for this pulse is approximately

$L_{NL} = 1/\gamma P_0 \approx 1$ m. Considering the short propagation distance compared with the nonlinear length and the long duration of the pulse, we do not observe any appreciable dispersive or nonlinear pulse broadening effects. However, the impact of the FWM processes in generating new wavelengths can be clearly observed in Fig. 6. We note that other phase-matched FWM processes beyond (40) are possible in GIMFs which are responsible for the generation of other wavelengths as can be also observed in Fig. 6, the full treatment of which will be presented in a later publication.

VII. CONCLUSION

We have presented a detailed account of the modal properties, dispersive behavior, and nonlinear mode coupling in GIMFs and derived a simplified GNLSE, which can be used to explore the rich nonlinear dynamics related to the propagation and interaction of multiple modes in GIMFs in a tractable manner. Although we have restricted our formulation to only the zero-angular-momentum $m = 0$ modes, which are typically less than 5 modes among the more than 100 modes in a C-GIMF, the resulting propagation dynamics is still considerably more complex than that of the SMFs. While the exclusion of $m \neq 0$ restricts the applicability of our formalism to special cases and carefully crafted experiments, we anticipate that much can be learned from $m = 0$ modes, without having to deal with a system that can bury much of the interesting physics beneath its overwhelming complexity.

We note that this paper is mainly concerned with laying out the basic formalism, and is meant to pave the way for our future studies on detailed treatment of specific nonlinear phenomena such as SPM, XPM, and FWM in GIMFs. We anticipate that careful and detailed studies of the nonlinear multimode interactions in GIMFs result in interesting nonlinear dynamics and novel device applications.

APPENDIX

In this section, we will present order-of-magnitude estimates of mode coupling in GIMFs; in particular, we will discuss the efficiency of $m \neq 0$ mode excitations from $m = 0$ modes.

In most systems involving MMFs and especially in practical MMF communication systems, linear coupling among modes plays an important role and must be properly addressed. The coupling is mediated by various processes, including micro- and macrobending, stress, cabling, core size variations along the fiber, and various other manufacturing defects. Mode coupling, because of its random nature, is traditionally treated stochastically in MMF communication systems, often using power-coupling models (see, e.g., [20]–[23]). As a starting point for any method to address the mode coupling problem, the GNLSE (20) must be supplemented with an additional mode coupling term $i \sum_q C_{pq} A_q(z, t)$ on the right-hand side, where C_{pq} are the linear coupling coefficients among the modes, representing both the deterministic and stochastic processes. It must be noted that the presence of nonlinearity often complicates the stochastic analysis, because the interaction of the nonlinear coupling terms with the stochastic linear processes may result in colored non-Gaussian nonstationary statistics in the power flow equations. Unfortunately, well-developed methods do not exist to handle

such stochastic equations and one must resort to either brute-force application of Monte Carlo simulations, or exploring the systems in the low-power regime, where the nonlinear terms can be linearized.

For the purposes of this paper, which is more concerned with short segments of GIMFs, macrobending is the most important coupling process. In particular, macrobending can potentially result in the excitation of nonzero-angular-momentum modes ($m = \pm 1$) from $m = 0$ modes. The coupling between ($m = 0, p = 0$) and ($m = 1, p = 0$) modes can be easily estimated using the formalism presented in [1] and [24], and can be written as

$$\mathcal{C} \approx \frac{n_0 k_0}{R_c} \langle 1_m, 0_p | x | 0_m, 0_p \rangle = \frac{n_0 \pi \rho_0}{R_c \lambda} \quad (41)$$

where R_c is bending radius of the GIMF. $|0_m, 0_p\rangle$ and $|1_m, 0_p\rangle$ represent the ($m = 0, p = 0$) and ($m = 1, p = 0$) modes, respectively. The length scale associated with the coupling term is $\mathcal{L}_c = 1/\mathcal{C}$; for the design parameters of C-GIMF at $\lambda = 1550$ nm, $\mathcal{L}_c \approx R_c/16$. In practice, the coupling between these two modes is strongly suppressed due to the large phase mismatch, because the two modes belong to two different mode groups. The phase mismatch $\Delta\beta$ between these modes can be approximated using (17), resulting in $\Delta\beta = \sqrt{2\Delta}/R$. The power coupling efficiency (the maximum fraction of the power in $m = 0$ mode that couples to the $m = 1$ mode) can be characterized by $\zeta = \mathcal{C}^2/(\Delta\beta/2)^2$, where it can be easily shown that $\zeta \ll 1$, unless $R_c < 6$ mm.

From the aforementioned analysis, it is clear that for device applications which rely on short segments of GIMFs, and when only $m = 0$ modes are initially excited as in [3], [4], excitation of $m = \pm 1$ modes is a highly inefficient process; for example, for a fiber segment with $R_c \approx 1$ m, $\zeta \approx 3 \times 10^{-5}$. As long as the fiber is held fairly straight, the power coupled to the $m = \pm 1$ mode due to macrobending is negligible. We emphasize that such a large phase-mismatch between $m = 0$ and $m = \pm 1$ modes is a characteristic of GIMFs and does not hold in general for all MMFs; this is one of the key reasons in making GIMFs so attractive for device applications [3], [4].

Core size distortions can also lead to coupling among modes with $\Delta m = \pm 2$ [25]. Such distortions are the result of manufacturing errors and are often small; however, $\Delta m = \pm 2$ processes can result in couplings within a mode group where the modes are approximately phase-matched. Detailed analysis of this issue is beyond the scope of this paper and the results depend strongly on the manufacturing quality of the fiber. For short-length device applications such as those in [3] and [4], this effect is negligible, for the range of the fibers studied in [3] and [4]. However, in MMF communication systems where propagation distances are much longer, one must worry about both $\Delta m = \pm 1$ and $\Delta m = \pm 2$ process, where partial phase matching in the $\Delta m = \pm 1$ processes can also be assisted by various random variations along the fiber.

REFERENCES

- [1] M. B. Shemirani, W. Mao, R. A. Panickar, and J. M. Kahn, "Principal modes in graded-index multimode fiber in presence of spatial- and polarization-mode coupling," *J. Lightw. Technol.*, vol. 27, no. 10, pp. 1248–1261, May 2009.

- [2] E. Ding, S. Lefrancois, J. N. Kutz, and F. W. Wise, "Scaling fiber lasers to large mode-area: An investigation of passive mode-locking using multi-mode fiber," *IEEE J. Quantum Electron.*, vol. 47, no. 5, pp. 597–606, May 2011.
- [3] A. Mafi, P. Hofmann, C. J. Salvin, and A. Schülzgen, "Low-loss coupling between two single-mode optical fibers with different mode-field diameters using a graded-index multimode optical fiber," *Opt. Lett.*, vol. 36, pp. 3596–3598, 2011.
- [4] P. Hofmann, A. Mafi, C. J. Salvin, T. Tiess, N. Peyghambarian, and A. Schülzgen, "Detailed investigation of mode-field adapters utilizing multimode-interference in graded index fibers," *J. Lightw. Technol.*, vol. 30, no. 14, pp. 2289–2298, Jul. 2012.
- [5] G. P. Agrawal, *Nonlinear Fiber Optics*, 4th ed. San Diego: Academic Press, 2007.
- [6] G. P. Agrawal, "Nonlinear fiber optics: Its history and recent progress [invited]," *J. Opt. Soc. Amer. B*, vol. 28, pp. A1–A10, 2011.
- [7] R. H. Stolen, J. E. Bjorkholm, and A. Ashkin, "Phase-matched three-wave mixing in silica fiber optical waveguides," *Appl. Phys. Lett.*, vol. 24, pp. 308–310, 1974.
- [8] C. Lin and M. A. Bösch, "Large-Stokes-shift stimulated fourphoton mixing in optical fibers," *Appl. Phys. Lett.*, vol. 38, pp. 479–481, 1981.
- [9] B. Kibler, J. Fatome, C. Finot, G. Millot, F. Dias, G. Genty, N. Akhmediev, and J. M. Dudley, "The peregrine soliton in nonlinear fibre optics," *Nat. Phys.*, vol. 6, pp. 790–795, 2010.
- [10] F. Poletti and P. Horak, "Description of ultrashort pulse propagation in multimode optical fibers," *J. Opt. Soc. Amer. B*, vol. 25, pp. 1645–1654, 2008.
- [11] D. Gloge and E. A. J. Marcatili, "Multimode theory of graded-core fibers," *Bell Syst. Tech. J.*, vol. 52, pp. 1563–1578, 1973.
- [12] A. Mafi, "Bandwidth improvement in multimode optical fibers via scattering from core inclusions," *J. Lightw. Technol.*, vol. 28, pp. 1547–1555, 2010.
- [13] K. Okamoto, *Fundamentals of Optical Waveguides*, 2nd ed. San Diego: Academic Press, 2006.
- [14] N. Shibata and T. Eda, "Refractive index dispersion properties of glasses for optical fibers," Japan, 1980, pp. 114–118, Paper of Technical Group, IEICE, no. OQE80.
- [15] T. Izawa and S. Sudo, *Optical Fibers: Materials and Fabrication*. Tokyo: KTK Scientific Publisher, 1987.
- [16] R. Olshansky and D. B. Keck, "Pulse broadening in graded-index optical fibers," *Appl. Opt.*, vol. 15, pp. 483–491, 1976.
- [17] T. A. Lenahan, "Calculation of modes in an optical fiber using the finite element method and EISPACK," *Bell Syst. Tech. J.*, vol. 62, pp. 2663–2694, 1983.
- [18] M. Kolesik and J. V. Moloney, "Nonlinear optical pulse propagation simulation: From Maxwell's to unidirectional equations," *Phys. Rev. E*, vol. 70, p. 036604, 2004.
- [19] K. O. Hill, D. C. Johnson, and B. S. Kawasaki, "Efficient conversion of light over a wide spectral range by four-photon mixing in a multimode graded-index fiber," *Appl. Opt.*, vol. 20, pp. 1075–1079, 1981.
- [20] S. D. Personick, "Time dispersion in dielectric waveguides," *Bell Syst. Tech. J.*, vol. 50, pp. 843–859, 1971.
- [21] P. Pepeljugoski, S. E. Golowich, A. J. Ritger, P. Kolesar, and A. Risteski, "Modeling and simulation of next-generation multimode fiber links," *J. Lightw. Technol.*, vol. 21, no. 5, pp. 1242–1255, May 2003.
- [22] I. Gasulla and J. Capmany, "Transfer function of multimode fiber links using an electric field propagation model: Application to radio over fibre systems," *Opt. Express*, vol. 14, pp. 9051–9070, 2006.
- [23] D. Gloge, "Optical power flow in multimode fibers," *Bell Syst. Tech. J.*, vol. 51, pp. 1767–1780, 1972.
- [24] R. Olshansky, "Mode coupling effects in graded-index optical fibers," *Appl. Opt.*, vol. 14, pp. 935–945, 1975.
- [25] D. Marcuse and H. M. Presby, "Mode coupling in an optical fiber with core distortions," *Bell Syst. Tech. J.*, vol. 54, pp. 3–15, 1975.

Arash Mafi (M'07) received the Ph.D. degree from the Ohio State University, Columbus, in 2001.

He was a Research Associate at the Physics Department, Optical Sciences Center, and the Arizona Center for Mathematical Sciences, University of Arizona, from 2001 to 2005 where he was involved in single- and multicore double-clad and PCF lasers. He was a Senior Research Scientist at Corning Inc. from 2005 to 2008. He is currently an Assistant Professor in the Department of Electrical Engineering and Computer Science, University of Wisconsin-Milwaukee, Milwaukee.

Nonlinear multimodal interference and saturable absorption using a short graded-index multimode optical fiber

Elham Nazemosadat and Arash Mafi*

Department of Electrical Engineering and Computer Science, University of Wisconsin-Milwaukee, Milwaukee, Wisconsin 53211, USA

**Corresponding author: mafi@uwm.edu*

Received February 15, 2013; revised April 5, 2013; accepted April 5, 2013;
posted April 9, 2013 (Doc. ID 185419); published April 26, 2013

A detailed investigation of the nonlinear multimodal interference in a short graded-index multimode optical fiber is presented. The analysis is performed for a specific device geometry, where the light is coupled in and out of the multimode fiber via single-mode fibers. The same device geometry was recently used to obtain ultra-low-loss coupling between two single-mode optical fibers with very different mode-field diameters. Our results indicate the potential application of this simple geometry for nonlinear devices, such as in nonlinear switching, optical signal processing, or as saturable absorbers in mode-locked fiber lasers. Saturable absorption in this all-fiber configuration is discussed and it is shown that it provides attractive properties that can potentially be used in high pulse energy mode-locked fiber lasers. © 2013 Optical Society of America

OCIS codes: (060.2310) Fiber optics; (190.4370) Nonlinear optics, fibers; (060.7140) Ultrafast processes in fibers.

<http://dx.doi.org/10.1364/JOSAB.30.001357>

1. INTRODUCTION

Multimode interference (MMI) in optical fibers has been used successfully in recent years for various device applications, including beam shapers, sensors, and filters [1–8]. MMI in a graded-index multimode optical fiber (GIMF) was recently used to create very low-loss couplers between two single-mode optical fibers (SMFs) with very different mode-field diameters [9,10]. Here, the linear analysis of [9] is extended and the MMI effect in the nonlinear regime for the GIMF coupler geometry shown in Fig. 1 is investigated. The main intention of this study is to explore the possibility of using the simple SMF-GIMF-SMF geometry in nonlinear device applications, such as in optical signal processing [11] or as a saturable absorber (SA) in mode-locked fiber lasers [12,13].

GIMFs are commonly used in fiber-optic communications to reduce modal dispersion, as the group velocities of all modes are nearly identical at the design wavelength [14,15]. However, GIMFs exhibit another unique property that makes them very attractive for MMI applications: the propagation constants of their modes are equally spaced. Consequently, their self-imaging lengths can be very short, even less than 1 mm [9]; therefore, it is possible to make extremely short (even submillimeter) practical MMI devices [10] or to easily tune the length of the GIMF coupler for a specific MMI application [10].

In this paper, our studies are focused on the simplest case of nonlinear MMI (NL-MMI) in the setup shown in Fig. 1, with identical input and output SMFs. This choice is also the most practical one for most device applications. Our results will elucidate some general behaviors of such couplers in the nonlinear regime. More complex geometries involving different

fiber junctions and using various mode conversion techniques [16], such as long-period gratings [17], can modify some of the observations and conclusions. However, such complex modifications are less likely to be adopted in practical device applications in the near future. We hope that our results can be a useful starting point for future studies of NL-MMI and mode conversion in more complex systems.

NL-MMI has been studied in various contexts over the years (e.g., [18]). Generally speaking, nonlinear devices that operate based on nonlinear mode switching and coupling in spatially separated waveguides can also be viewed as MMI devices [19–22]. Nonlinear polarization rotation is another important example of NL-MMI (between two orthogonal polarization modes) that closely resembles our analysis here [23,24].

In Section 2, a general overview of GIMFs, nonlinear propagation in multimode optical fibers, and MMI are presented. NL-MMI in GIMFs in the context of the SMF-GIMF-SMF geometry of Fig. 1 is discussed in Section 3. In Subsection 3.A, a reduced version of the model that includes only two propagating modes is analyzed. This simplification helps us to develop proper insight into the physics of NL-MMI in GIMFs. In Subsection 3.B, our analysis is extended to the realistic case of five propagating modes. The impact of the presence of additional propagating modes in the NL-MMI setup can be shown by comparing these results with the results of Subsection 3.A. In Section 4, the saturable absorption behavior of the SMF-GIMF-SMF geometry is analyzed as an example of the utility of this setup for device applications. The concluding remarks are presented in Section 5, where it is shown that the SMF-GIMF-SMF geometry can be a viable design for nonlinear switching or saturable absorption.



Fig. 1. GIMF of length L is used as an intermediate coupler between two SMF fibers. In [9,10], this geometry was used to create very low-loss couplers between two SMFs with very different mode-field diameters. In this paper, nonlinear MMI effects for identical input and output SMFs are explored.

The formalism and results in this paper are mainly laid out in dimensionless units. This choice is common in nonlinear fiber optics because it reduces the number of parameters and prevents redundancy in the analysis. For real-world applications, it is easy to convert back to the dimensionful parameters. In Section 5, the performance of a NL-MMI SA device with specific parameters from commercially available optical fibers is analyzed.

In order to reduce the complexity of the analysis and to make the problem more tractable, the studies in this paper are considered in the continuous wave (CW) limit. In practice, after the design parameters are chosen based on the CW analysis, the temporal effects can be included to optimize the final design. GIMFs, if used near their optimal design wavelengths, are particularly attractive for short-pulse ultrafast applications compared with other MMFs. The low modal dispersion in GIMFs ensures that pulses do not break up in short GIMF segments [25], making the CW analysis an adequate approximation.

Finally, it should be pointed out that the transmission through the SMF-GIMF-SMF geometry is a periodic function of the frequency of the light source [9,10]. For mode-locking applications where short pulses are generated with very large spectral bandwidth, the length of the GIMF needs to be sufficiently short to provide the necessary spectral transmission window. Moreover, the SMF-GIMF-SMF geometry can be potentially used as the spectral filter that is required to stabilize the mode-locking operation of normal-dispersion high-energy femtosecond fiber lasers [26].

2. FUNDAMENTALS

In the following three subsections, a brief general overview of GIMFs (Subsection 2.A), nonlinear multimode propagation of light in GIMFs (Subsection 2.B), and the general formulation of the MMI phenomenon in GIMFs in the context of the SMF-GIMF-SMF coupler (Subsection 2.C) will be presented. The formulation presented in this section will be used to analyze the nonlinear behavior of the SMF-GIMF-SMF geometry in detail in subsequent sections.

A. Overview of GIMFs

The refractive index profile of a GIMF is given by

$$n^2(\rho) = n_0^2 \left[1 - 2\Delta \left(\frac{\rho}{R} \right)^\alpha \right], \quad (1)$$

where R is the core radius, n_0 is the refractive index at the center of the core, Δ is the index step, $\alpha \approx 2$ characterizes a near parabolic-index profile in the core ($\rho \leq R$), and $\alpha = 0$ in the cladding ($\rho > R$). The transverse electric field profile of a confined mode, with radial p ($p \geq 0$) and angular m integer numbers, can be expressed as [25]

$$E_{p,m}(\rho, \phi) = N_p^m \frac{\rho^{|m|}}{\rho_0^{|m|+1}} \exp\left(-\frac{\rho^2}{2\rho_0^2}\right) L_p^{|m|}\left(\frac{\rho^2}{\rho_0^2}\right) e^{im\phi}, \quad (2)$$

where $L_p^{|m|}$ are generalized Laguerre polynomials, and ρ_0 and N_p^m are given by

$$\rho_0 = \frac{R^{1/2}}{(k_0 n_0)^{1/2} (2\Delta)^{1/4}}, \quad N_p^m = \sqrt{\frac{p!}{\pi(p+|m|)!}}, \quad (3)$$

where $k_0 = 2\pi/\lambda$. The coefficients N_p^m of these Laguerre-Gauss modes (LG_{pm}) are chosen such that the modes are orthonormal. Using the bra-ket notation, the electric field profile of the LG_{pm} mode is identified as $|p, m\rangle = E_{p,m}(\rho, \phi)$ and the orthonormality condition is expressed as $\langle p, m | p', m' \rangle = \delta_{p,p'} \delta_{m,m'}$, where the bra-ket indicates integration in the transverse (ρ - ϕ) coordinates.

All modes with equal group mode number $g = 2p + |m| + 1$ are almost degenerate in the value of the propagation constant, which is given according to the formula

$$\beta_{(g)} = n_0 k (1 - 2\Delta X_g)^{1/2}, \quad (4)$$

where

$$X_g = \left(\frac{g}{\sqrt{N_\alpha}} \right)^{2\alpha/(\alpha+2)}, \quad (5)$$

N_α is the total number of guided modes (counting the polarization degeneracy) and is given by

$$N_\alpha = \frac{\alpha}{\alpha + 2} n_0^2 k_0^2 R^2 \Delta. \quad (6)$$

While the analysis presented in this article is generally applicable to a wide range of GIMFs and is presented in dimensionless units, for specific numerical arguments and comparisons, the parameters of a conventional high-bandwidth commercial-grade GIMF such as Corning's InfiniCor eSX+ will be used; this fiber is optimized for high bandwidth performance at 850 nm wavelength, with the core radius of $R = 25 \mu\text{m}$. The specified GIMF will be referred to as C-GIMF standing for the *conventional GIMF*. It should be noted that the key spatial dimension in a GIMF that sets all its modal properties is not the core radius R , but is $\rho_c = \sqrt{2}\rho_0$, where ρ_0 is defined in Eq. (3). ρ_c is the mode radius of the LG_{00} mode; for C-GIMF, $\rho_c \approx 7.7 \mu\text{m}$ at 1550 nm wavelength and $\rho_c \approx 5.7 \mu\text{m}$ at 850 nm wavelength.

B. Overview of Nonlinear Propagation in GIMFs

Consider an input optical field injected into the core of the GIMF. The injected field excites the LG_{pm} modes of the GIMF with different amplitudes $A_{p,m}(0)$. $A_{p,m}(z)$ will be regarded as the envelope of the electric field and $z = 0$ indicates the input end of the GIMF [25]. In order to simplify our notation, the collective index μ will be used to represent the p, m index pair of the LG_{pm} modes, i.e., $\mu \equiv (p, m)$ in the rest of this section. However, when necessary, we will directly use the (p, m) labels or specify how to translate the μ index into the (p, m) index pair. $|A_\mu(z)|^2$ represents the optical power in the LG_{pm} mode.

In the scalar approximation, the generalized nonlinear Schrödinger equation (GNLSE) describing the CW longitudinal evolution of $A_{p,m}(z)$ can be written as

$$\frac{\partial A_\mu}{\partial z} = i\delta\beta_\mu A_\mu + i\gamma \sum_{\nu,\kappa,\xi} \tilde{\eta}_{\mu\nu\kappa\xi} A_\nu A_\kappa A_\xi^*, \quad (7)$$

where $\delta\beta_\mu = \beta_\mu - \beta_{(1)}$, β_μ is the propagation constant of the mode with the collective index μ and $\beta_{(1)}$ is the propagation constant of the LG₀₀ mode with $g = 1$ from Eq. (4). The “normalized” nonlinear coupling coefficient is a fully symmetric tensor and is defined as $\tilde{\eta}_{\mu\nu\kappa\xi} = \gamma_{\mu\nu\kappa\xi}/\gamma$ where

$$\gamma_{\mu\nu\kappa\xi} = \left(\frac{n_2\omega_0}{c}\right) \int d^2x E_\mu^* E_\nu E_\kappa E_\xi^*. \quad (8)$$

In Eq. (8), E_μ is the shorthand notation for $E_{p,m}(\rho, \phi)$. $\gamma = \gamma_{0000}$ is the nonlinear coefficient of the LG₀₀ mode, n_2 is the nonlinear index coefficient, and ω_0 is the carrier frequency. For the lowest order mode LG₀₀ for which ρ_c is simply the modal radius, one can define $\gamma_{0000} = n_2\omega_0/A_{\text{eff}}^0$, where $A_{\text{eff}}^0 = \pi\rho_c^2$. The total optical power in the GIMF is given by $\tilde{P} = \sum_\mu |A_\mu(z)|^2$ and is conserved in propagation along the GIMF, i.e., $\partial_z \tilde{P} = 0$.

It is more convenient to express the GNLSE in dimensionless units. B_μ can be defined as

$$B_\mu(z) = \frac{1}{\sqrt{\tilde{P}}} A_\mu(z) e^{-i\gamma\tilde{P}z}, \quad (9)$$

and rescale the longitudinal coordinate z by the difference between the propagation constants of the first and the second mode groups $\beta_{(1)} - \beta_{(2)}$,

$$\zeta = z \times (\beta_{(1)} - \beta_{(2)}). \quad (10)$$

Using these transformations, Eq. (7) can be simplified as

$$\partial_\zeta B_\mu = -i(r_\mu + \tilde{\gamma})B_\mu + i\tilde{\gamma} \sum_{\nu,\kappa,\xi} \tilde{\eta}_{\mu\nu\kappa\xi} B_\nu B_\kappa B_\xi^*, \quad (11)$$

where Eq. (11) is expressed in terms of the dimensionless coefficients

$$r_\mu = \frac{\beta_\mu - \beta_{(1)}}{\beta_{(2)} - \beta_{(1)}}, \quad \tilde{\gamma} = \frac{\gamma\tilde{P}}{\beta_{(1)} - \beta_{(2)}}. \quad (12)$$

and can be solved for the dimensionless field B_μ in terms of the dimensionless longitudinal coordinate ζ . It can be realized that the rescaled fields B_μ satisfy the power conservation condition $\sum_\mu |B_\mu(z)|^2 = 1$ at any points along the GIMF.

Using Eqs. (4) and (5) the fact that $X_g \ll 1$, one can show that r_μ is non-negative and is nearly an integer: $r_\mu \approx g_\mu - 1$, where g_μ is the group number associated with mode μ [10].

C. Overview of MMI in GIMFs

The particular setup that is considered in this paper is shown in Fig. 1 and consists of injecting a nearly Gaussian beam from the input SMF, which is spliced to the input facet of the GIMF, and collecting the light at the other end of the GIMF from the output SMF. If the normalized mode of the input SMF is

defined as $|\text{in}\rangle$, where $\langle \text{in} | \text{in} \rangle = 1$, the mode amplitude in the GIMF at the input can be written as $A_\mu(0) = \sqrt{\tilde{P}} \langle p, m | \text{in} \rangle$, where $|p, m\rangle$ is the GIMF mode defined in Eq. (2).

The relative transmitted power to the output SMF is given by

$$\tau = \frac{1}{\tilde{P}} |\langle \text{out} | E(\rho, \phi, L) \rangle|^2, \quad (13)$$

where $|\text{out}\rangle$ is the normalized mode of the output SMF, and $|E(\rho, \phi, L)\rangle$ is the total field at the output facet of the GIMF with a length of L , calculated from

$$E(\rho, \phi, L) = e^{i\beta_{(1)}L} \sum_\mu A_\mu(L) E_\mu(\rho, \phi). \quad (14)$$

Identical input and output SMFs are the focus of this paper ($|\text{in}\rangle \equiv |\text{out}\rangle$), for which the relative power transmission can be written as

$$\tau = \frac{1}{\tilde{P}^2} \left| \sum_\mu A_\mu^*(0) A_\mu(z) \right|^2 = \left| \sum_\mu B_\mu^*(0) B_\mu(z) \right|^2. \quad (15)$$

The injected beam from the input SMF is in the form of a Gaussian with radius w and can be expressed as

$$|\text{in}\rangle = \sqrt{\frac{2}{\pi w^2}} \exp\left(-\frac{\rho^2}{w^2}\right). \quad (16)$$

Because of the azimuthal symmetry of the input Gaussian beam, if the input SMF is centrally aligned with the GIMF, only LG_{p0} ($m = 0$) modes can be excited in the GIMF. The excitation amplitude can be calculated as [9]

$$B_p(0) = \frac{2\sqrt{\eta}}{\eta + 1} \Psi^p, \quad \eta = \frac{\rho_c^2}{w^2}, \quad \Psi = \frac{\eta - 1}{\eta + 1}. \quad (17)$$

In Fig. 2, the excitation amplitudes of the LG_{p0} modes are displayed as a function of the radial number p , for three different values of the η parameter. For the case of $\eta = 1$ (not shown in Fig. 2), only the LG₀₀ mode is excited, because the input Gaussian beam is mode-matched to the LG₀₀ mode of the GIMF. For a slightly larger value of $\eta = 1.1$, only 0.2% of power is coupled to the LG₀₁ mode and the power coupled to

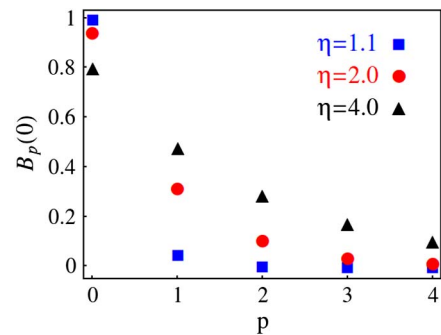


Fig. 2. Excitation amplitudes of the LG_{p0} modes from Eq. (17) are plotted as a function of the radial number p , for three different values of the η parameter.

higher order modes is negligible. For the larger value of $\eta = 4$, only 64% of the power is coupled to the LG_{00} mode. In this case, the relative power coupled to the LG_{01} , LG_{02} , and LG_{03} modes are 23%, 8%, and 3%, respectively. $\eta = 4$ is obtained when coupling the C-GIMF to an SMF with the mode-field diameter of nearly $7.7 \mu\text{m}$ at 1550 nm wavelength. For coupling of the C-GIMF to Corning SMF-28TM (SMF-28) with the mode-field diameter of $10.4 \mu\text{m}$ at 1550 nm wavelength, the value of η is nearly equal to 2.2.

There are two reasons for not exploring the case of $\eta < 1$ in this manuscript. First, under the $\eta \rightarrow \eta^{-1}$ transformation, Eq. (17) remains unchanged except for an overall multiplicative factor of $(-1)^p$ [9]. Despite this change in the initial phase, no new insight is obtained in overall observations and general conclusions presented in this paper. Second, η is larger than unity for most combinations of commercially available SMFs and GIMFs. Therefore, our analysis is limited to $\eta > 1$ to avoid adding unnecessary complexity.

3. NL-MMI: SMF-GIMF-SMF GEOMETRY

In the following, our studies will only include the case of $m = 0$ or zero-angular momentum modes (see the discussion in Subsection 2.C). The experimental evidence presented in [9,10] confirms the reliability of this choice. Moreover, using the formalism outlined in [25] it can be shown that the conservation of angular momentum, dictated by the symmetries of the nonlinear coupling terms, prevents the excitation of any modes with $m \neq 0$ along the fiber from only $m = 0$ modes. Therefore, our analysis can be safely limited to the small and manageable zero angular momentum subset of modes. It is worth mentioning that $m \neq 0$ modes may still be excited because of the bending and imperfections in the fiber. This issue will be addressed in Section 5, but for now our analysis is limited to the subspace of $m = 0$ modes.

Because only LG_{p0} modes are considered in the analysis, one can readily identify the collective index μ used in Section 2 with the radial mode number p .

Therefore, all the indexes in the relevant equations such as in Eqs. (7), (8), (11), and (14) can be directly replaced with the radial mode numbers of the LG_{p0} modes.

In a typical GIMF, only a handful of $m = 0$ modes are supported in the core; for example, only five $m = 0$ modes are supported at 1550 nm wavelength in a C-GIMF. Even for such a small number of modes, the GNLSSE will have many terms and becomes quite complicated. In order to develop the proper fundamental understanding and intuition on the key mechanisms involved in the NL-MMI of these modes in a GIMF, our analysis is initially limited to the smaller subset of LG_{00} and LG_{10} modes in Subsection 3.A. This way, the physics of the NL-MMI in the SMF-GIMF-SMF is not buried under the complexity introduced by the large number of modes propagating in the GIMF. Eventually, in Subsection 3.B, the number of propagating modes in the GIMF will be increased to five, considering LG_{00} through LG_{40} , and the similarities and differences between the two-mode and the five-mode scenarios will be explored.

As a reference for comparison with nonlinear couplings for self-phase modulation and cross-phase modulation in conventional SMFs [24], the nonlinear coupling terms among the three lowest order modes in GIMFs (i.e., LG_{00} , LG_{10} , and LG_{20}), are: $\tilde{\eta}_{0001} = \tilde{\eta}_{0011} = \tilde{\eta}_{1111} = 1/2$, $\tilde{\eta}_{0012} = \tilde{\eta}_{0022} = 3/8$,

$$\tilde{\eta}_{2222} = 11/32, \quad \tilde{\eta}_{1122} = 5/16, \quad \tilde{\eta}_{0002} = \tilde{\eta}_{0111} = \tilde{\eta}_{0112} = \tilde{\eta}_{1112} = 1/4, \quad \tilde{\eta}_{0122} = 3/16, \quad \tilde{\eta}_{1222} = 11/64, \quad \tilde{\eta}_{0222} = 5/32.$$

A. NL-MMI with and Modes

In this subsection, it is assumed that only LG_{00} and LG_{10} modes are excited in the GIMF and the optical power is distributed only between these two modes. It should be taken into account that this assumption is only strictly valid for $\eta \approx 1$ from Eq. (17) ($p_0 \gg p_1$ in that case). However, our intention in this section is not to simulate an exact experimentally realizable configuration in the spirit of Fig. 1. Rather, this limited two-mode subspace is used to gain insight into the physics of NL-MMI in GIMFs. Therefore, in this subsection, the limitations of Eq. (17) are abandoned and it is assumed that $p_0 + p_1 = 1$, where $p_0 = |B_0|^2$ and $p_1 = |B_1|^2$ can adopt any (positive) values subject to this condition. In practice, it may be possible to create this scenario experimentally in a more complex setup than that of Fig. 1, e.g., by using mode conversion techniques. However, such details are beyond the scope and intentions of this subsection.

Using Eq. (11), the following coupled nonlinear equations are obtained:

$$\begin{aligned} \partial_\zeta B_0 &= i\tilde{\gamma} \left(|B_0|^2 + \frac{1}{4}|B_1|^2 \right) B_0 + \frac{i\tilde{\gamma}}{2} (B_0^2 B_1^* + B_1^2 B_0^*), \\ \partial_\zeta B_1 &= -ir_1 B_1 + \frac{i\tilde{\gamma}}{2} B_0 + \frac{i\tilde{\gamma}}{2} \left(-|B_1|^2 B_1 + B_0^2 B_1^* + \frac{1}{2} B_1^2 B_0^* \right). \end{aligned} \quad (18)$$

Nonlinear effects can be ignored when $\tilde{\gamma}\tilde{L} \approx 0$, where $\tilde{L} = L \times (\beta_{(1)} - \beta_{(2)})$ and L is the total length of the GIMF. In the absence of nonlinear effects, the solution to Eq. (18) can be written as

$$B_0(\zeta) = B_0(0), \quad B_1(\zeta) = e^{-ir_1\zeta} B_1(0). \quad (19)$$

In the linear case, the relative power of each mode is conserved, i.e., p_0 and p_1 remain unchanged along the GIMF. The relative power transmission in an SMF-GIMF-SMF setup in the linear limit with two modes can be calculated from Eq. (15) as

$$\tau = 1 - 4p_0p_1 \sin^2 \left(\frac{r_1\tilde{L}}{2} \right). \quad (20)$$

The relative power transmission is a periodic function of the length of the GIMF and varies periodically between $\tau_{\min} = 1 - 4p_0p_1$ and $\tau_{\max} = 1$; $\tau_{\min} = 0$ in the special case where the power is equally distributed ($p_0 = p_1 = 1/2$). These issues have been discussed in further detail in [9], where the linear MMI in GIMFs is explored in the presence of multiple $m = 0$ modes.

The main parameters that determine the value of the relative power transmission in the SMF-GIMF-SMF setup are the relative power of the modes (p_0 and p_1), the normalized GIMF length (\tilde{L}), and the normalized nonlinear coefficient $\tilde{\gamma}$. In Fig. 3, the relative power transmission is plotted as a function of \tilde{L} for three different cases of $\tilde{\gamma} = 0$ (solid), $\tilde{\gamma} = 0.7$ (dashed), and $\tilde{\gamma} = 3$ (dotted). All cases are plotted for relative power values of $p_0 = p_1 = 0.5$. The linear case with $\tilde{\gamma} = 0$ clearly follows

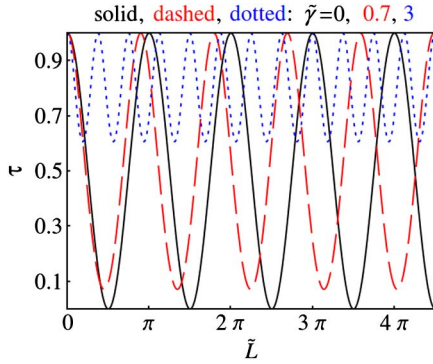


Fig. 3. Relative power transmission is plotted as a function of the normalized GIMF length \tilde{L} for the case of LG_{00} and LG_{10} modes when $p_0 = p_1 = 0.5$ at $\zeta = 0$, for $\tilde{\gamma} = 0$ (solid), $\tilde{\gamma} = 0.7$ (dashed), and $\tilde{\gamma} = 3$ (dotted).

Eq. (20), where the oscillation periodicity of τ with respect to \tilde{L} (normalized GIMF length) is $T_L = 2\pi/r_1 \approx \pi$.

When the nonlinear effects are small, the nonlinearity merely results in an additional phase mismatch between the LG_{00} and LG_{10} modes, e.g., for $\tilde{\gamma} = 0.7$ the accumulated nonlinear phase mismatch is nearly π at $\tilde{L} = 4.5\pi$ and is responsible for changing the $\tau = 0$ in the linear case to $\tau \approx 1$ for $\tilde{\gamma} = 0.7$ in Fig. 3. It should be emphasized that in the presence of nonlinearity, p_0 and p_1 are not conserved and vary periodically along the GIMF (LG_{00} and LG_{10} exchange power). However, unless we explicitly specify their ζ -dependence, when referring to p_0 and p_1 , we mean their initial value at the $\zeta = 0$ point in the GIMF and refrain from introducing new variables.

The linear and nonlinear cases of $\tilde{\gamma} = 0$ and $\tilde{\gamma} = 0.7$ differ in another important feature besides the cumulative nonlinear phase mismatch; the minimum value of τ for $\tilde{\gamma} = 0.7$ is larger than zero. This effect becomes more prominent for larger relative nonlinear coefficients. In fact, as can be seen for $\tilde{\gamma} = 3$ in Fig. 3, the relative power transmission remains above 60% for all values of \tilde{L} .

The relative power transmission explored in Fig. 3 is for the case of $p_0 = p_1 = 0.5$. In Fig. 4, similar situations as in Fig. 3 are considered, yet with $p_0 = 0.75$ and $p_1 = 0.25$ at $\zeta = 0$. The solid line relates to $\tilde{\gamma} = 0$ and follows Eq. (20). Similar to Fig. 3, the nonlinear phase mismatch between the LG_{00} and LG_{10} modes increases the frequency of oscillation of τ with respect of \tilde{L} as the relative nonlinear coefficient is increased. In the case of $\tilde{\gamma} = 3$ (dotted), the relative power transmission τ

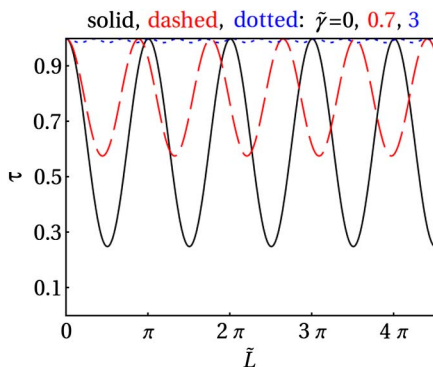


Fig. 4. Same as Fig. 3, except for $p_0 = 0.75$ and $p_1 = 0.25$ at $\zeta = 0$.

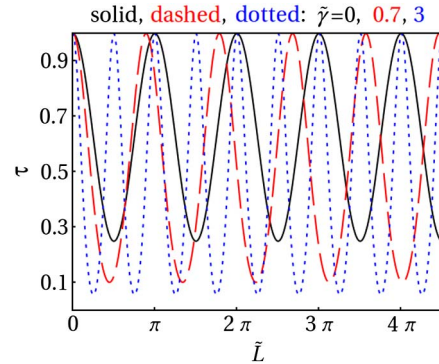


Fig. 5. Same as Fig. 3, except for $p_0 = 0.25$ and $p_1 = 0.75$ at $\zeta = 0$.

remains nearly equal to unity for all values of \tilde{L} . For large values of $\tilde{\gamma}$ (e.g., $\tilde{\gamma} = 3$), the power coupling between LG_{00} and LG_{10} modes is inefficient and the amplitude of the oscillation in the relative power carried by each mode as a function of \tilde{L} is small and is a decreasing function of $\tilde{\gamma}$. In other words, for a sufficiently large values of $\tilde{\gamma}$, p_0 and p_1 remain unchanged as they propagate through the GIMF. The cumulative phase of the LG_{00} and LG_{10} modes is also nearly identical for large $\tilde{\gamma}$ as the two modes propagate along the GIMF. The combined effects of the nearly unchanged relative power and the nearly identical cumulative phase of the modes results in the near unity value of τ in this situation.

In Fig. 5, similar situations as in Fig. 4 are considered, yet with $p_0 = 0.25$ and $p_1 = 0.75$ at $\zeta = 0$. The solid line relates to $\tilde{\gamma} = 0$ and is identical to the case of $p_0 = 0.75$ and $p_1 = 0.25$ presented in Fig. 4, in agreement with Eq. (20). Similar to Fig. 4, increasing the relative nonlinear coefficient results in a larger oscillation frequency of τ with respect to \tilde{L} . However, in complete contrast to the behavior observed in Fig. 4 for $\tilde{\gamma} \neq 0$, increasing $\tilde{\gamma}$ initially lowers the minimum value of τ and for sufficiently large values of $\tilde{\gamma}$, the minimum can even be equal to zero. If $\tilde{\gamma}$ is further increased, the minimum value of τ increases again and eventually settles asymptotically at a value that can be substantially different from zero. This behavior is dictated by a very efficient exchange of power between LG_{00} and LG_{10} modes as well as considerable difference between the cumulative phases of the modes; however, at a large $\tilde{\gamma}$ the cumulative phases of the modes become nearly identical.

As discussed above, the dynamics of power coupling between the LG_{00} and LG_{10} modes is quite complex. In Fig. 6, $p_0(\zeta = \tilde{L})$ is plotted as a function of $p_0(\zeta = 0)$ for $\tilde{L} = 4.5\pi$.

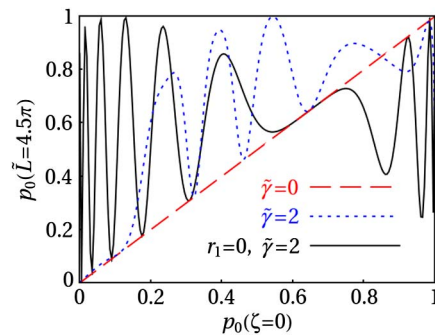


Fig. 6. This figure shows the exchange of power between the LG_{00} and LG_{10} modes, where p_0 at the output of the GIMF is plotted as a function of p_0 at the input for $\tilde{L} = 4.5\pi$.

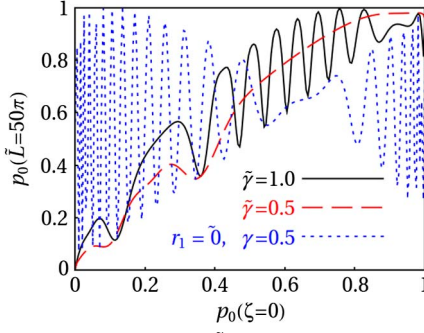


Fig. 7. Same as Fig. 6, except for $\tilde{L} = 50\pi$, and different choices of $\tilde{\gamma}$.

In the linear case, LG_{00} and LG_{10} modes are totally uncoupled and $p_0(\zeta = \tilde{L}) = p_0(\zeta = 0)$, as shown with the diagonal dashed line in Fig. 6. However, for $\tilde{\gamma} = 2$, nonlinearity couples the power between LG_{00} and LG_{10} modes and $p_0(\zeta = \tilde{L})$ oscillates as a function of $p_0(\zeta = 0)$, shown with the dotted line in Fig. 6. It can be seen that $p_0(\zeta = \tilde{L})$ oscillates more rapidly as $\tilde{\gamma}$ increases. In order to isolate the nonlinear effect, the dispersive term r_1 is set to zero and the power coupling curve for $\tilde{\gamma} = 2$ is re-plotted as the solid line in Fig. 6. Comparing the solid and dotted lines, it can be concluded that the effect of the dispersive term ($-ir_1B_1$) is to tame the oscillations, especially for p_0 near zero or unity.

For a longer GIMF (at fixed $\tilde{\gamma}$), the taming effect of the dispersive term will be even more pronounced and the amplitude of oscillations will be smaller. In Fig. 7, where \tilde{L} is assumed to be 50π , the “artificial” case of $r_1 = 0$, $\tilde{\gamma} = 0.5$ (dotted) oscillates rapidly and with large amplitude. However, for the real situation where $r_1 \approx 2$ (and $\tilde{\gamma} = 0.5$), the rapid oscillation is replaced with a smooth change (dashed line) that does not move far away from the diagonal virtual line of $p_0(\zeta = \tilde{L}) = p_0(\zeta = 0)$. Once the nonlinearity is increased to $\tilde{\gamma} = 1.0$, the oscillations reappear, yet with a much lower frequency and smaller amplitude (solid line) compared with the artificial case of $r_1 = 0$. It is noteworthy that the oscillations in the solid curve are mainly located in the region of the graph where the dotted curve does not oscillate much.

In order to examine the effect of the total power injected in the GIMF on the relative power transmission, the transmission is plotted as a function of $\tilde{\gamma}$ for the case of $\tilde{L} = 4.5\pi$ in Fig. 8. The length of the GIMF is chosen in such a way that for the linear case of $\tilde{\gamma} = 0$, relative power transmission τ is at its

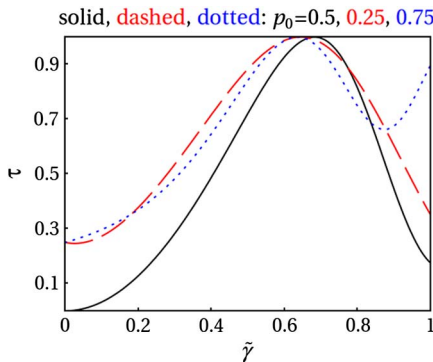


Fig. 8. Relative power transmission is plotted as a function of $\tilde{\gamma}$ (thus the total power) for $\tilde{L} = 4.5\pi$ for the case of LG_{00} and LG_{10} modes, when $p_0 = 0.5, 0.25, 0.75$ at $\zeta = 0$, in solid, dashed, and dotted lines, respectively.

minimum value of $\tau_{\min} = 1 - 4p_0p_1$ for the three cases of $p_0 = 0.5, 0.25, 0.75$ shown in Fig. 8. In agreement with our previous discussions, increasing the power (increasing $\tilde{\gamma}$) results in an increase in the value of τ and the maximum transmission of $\tau_{\max} = 1$ is obtained for $\tilde{\gamma} \approx 0.65$, nearly independent of the initial value of p_0 . As $\tilde{\gamma}$ is further increased, τ decreases again and follows an oscillatory form as a function of $\tilde{\gamma}$.

In practical devices, the GIMF is often considerably longer than $(\beta_{(1)} - \beta_{(2)})^{-1}$; therefore, $\tilde{L} \gg 1$. In Fig. 9, a scenario identical to that explored in Fig. 8 is considered, except for a much longer GIMF with $\tilde{L} = 100.5\pi$. The main difference between the cases of $\tilde{L} = 100.5\pi$ in Fig. 9 and $\tilde{L} = 4.5\pi$ in Fig. 8 is that much lower power (much smaller $\tilde{\gamma}$) is required for the GIMF with $\tilde{L} = 100.5\pi$ to switch the relative power transmission from τ_{\min} to τ_{\max} . For the case of $p_0 = 0.25$, the required $\tilde{\gamma}$ for power transmission switching is as low as ≈ 0.026 as can be seen in the dashed line in Fig. 9. Another important difference between the cases of $\tilde{L} = 4.5\pi$ and $\tilde{L} = 100.5\pi$ is that in the latter case, the value of $\tilde{\gamma}$ at which τ_{\max} is obtained is very sensitive to the initial distribution of the power among the modes.

B. Nonlinear MMI With Through Modes

In this subsection, the analysis of Subsection 3.A is extended to the more realistic case of five propagating modes. As mentioned before, this is a realistic scenario for the case of a C-GIMF at 1550 nm wavelength. The general observations in this subsection and the similarities and differences with the two-mode scenario of Subsection 3.A should cover the overall nonlinear dynamics in most realistic cases of NL-MMI in GIMFs.

In addition to the difference between the number of modes in this subsection versus Subsection 3.A, here the initial excitation amplitudes are chosen such that they satisfy Eq. (17) (otherwise the problem would become intractable). The main advantage of this choice is that it complies with the configuration of Fig. 1 and can be tested experimentally. Another important difference is that in Subsection 3.A it was assumed that $p_0 + p_1 = 1$, which resulted in $\tau_{\max} = 1$. In a realistic case where Eq. (17) is applied and the number of guided modes is finite, some of the power coming from the input SMF is coupled to the radiation and cladding modes. Therefore, it can be shown [9] that the maximum transmission is given by

$$\tau_{\max} = (1 - \Psi^{2P})^2 \leq 1, \quad (21)$$

where Ψ is defined in Eq. (17) and P is the total number of propagating modes with $m = 0$: $P = 5$ in this subsection.

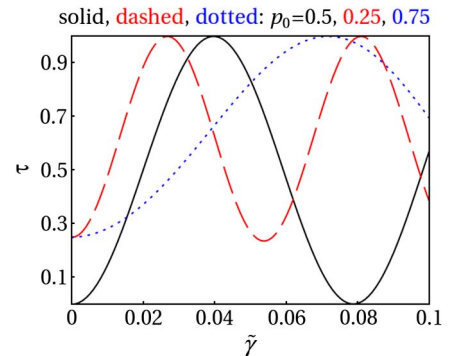


Fig. 9. Same as Fig. 8, except for $\tilde{L} = 100.5\pi$.

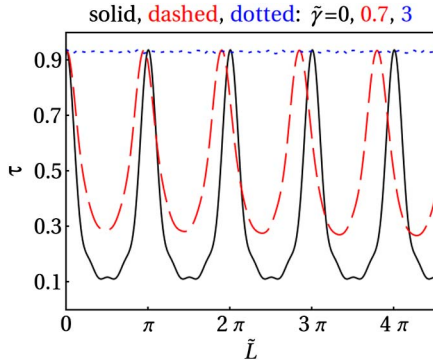


Fig. 10. Relative power transmission is plotted as a function of the normalized GIMF length \tilde{L} for the case of LG_{00} through LG_{40} modes (five zero angular modes) when $p_0 = 0.5$ at $\zeta = 0$ ($\eta = 3 + \sqrt{8}$), for $\tilde{\gamma} = 0$ (solid), $\tilde{\gamma} = 0.7$ (dashed), and $\tilde{\gamma} = 3$ (dotted). The results should be compared with Fig. 3 where only two modes, LG_{00} and LG_{10} , were considered.

Therefore, in all the plots shown in this subsection, $\tau_{\max} < 1$ and is given by Eq. (21).

In Fig. 10, the relative power transmission is plotted as a function of the normalized GIMF length \tilde{L} , for $\eta = 3 + \sqrt{8}$, which results in $p_0 = 0.5$. Similar to the two-mode scenario plotted in Fig. 3, the cases of $\tilde{\gamma} = 0$ (solid), $\tilde{\gamma} = 0.7$ (dashed), and $\tilde{\gamma} = 3$ (dotted) are analyzed. The linear case ($\tilde{\gamma} = 0$) in Fig. 10 is very similar to the two-mode case of Fig. 3, except that τ_{\min} and τ_{\max} are different due to the power leakage to the radiation and cladding modes, as explained above. However, the major difference is that at $\tilde{L} = 4.5\pi$, $\tilde{\gamma} = 0.7$ is not nearly enough to switch the relative power transmission from τ_{\min} (at $\tilde{\gamma} = 0$) to τ_{\max} in the five-mode scenario. In other words, higher power is required in the realistic five-mode scenario for transmission switching compared with the two-mode scenario. This is intuitively expected, as the presence of the higher modes results in the distribution of the intensity over a larger cross sectional area of the GIMF.

Next, the case of $p_0 = 0.75$ for the five-mode scenario is considered in Fig. 11, which should be compared with the two-mode scenario in Fig. 4. According to Eq. (17), this case can be obtained by choosing $\eta = 3$. Unlike the case of $p_0 = 0.5$ studied above, there is a strong similarity between the five-mode and two-mode scenarios in the $p_0 = 0.75$ case. At $\tilde{L} = 4.5\pi$, $\tilde{\gamma} = 0.7$ is nearly sufficient to switch the relative power transmission from τ_{\min} (at $\tilde{\gamma} = 0$) to $\approx \tau_{\max}$. This result

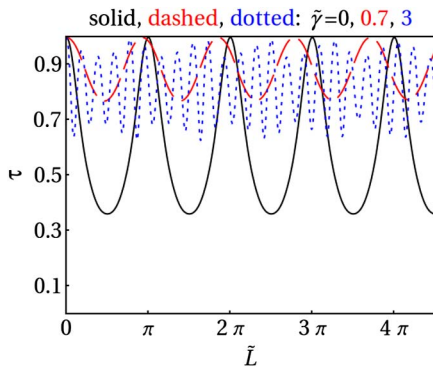


Fig. 11. Same as Fig. 10, except for $p_0 = 0.75$ at $\zeta = 0$ ($\eta = 3$). The results should be compared with Fig. 4 where only two modes, LG_{00} and LG_{10} , were considered.

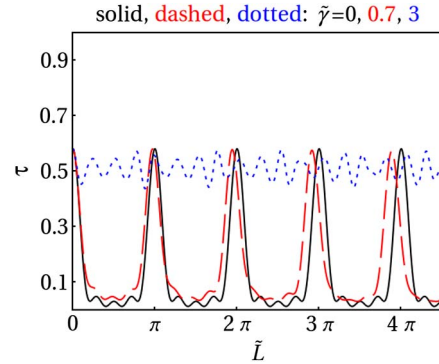


Fig. 12. Same as Fig. 10, except for $p_0 = 0.25$ at $\zeta = 0$ ($\eta = 7 + \sqrt{48}$). The results should be compared with Fig. 5 where only two modes, LG_{00} and LG_{10} , were considered.

is quite important, because $\eta = 3$ is more readily achievable when using standard commercial fibers than such large values as $\eta = 3 + \sqrt{8} \approx 5.8$. For example, as mentioned before, coupling C-GIMF to SMF-28 at 1550 nm, results in $\eta \approx 2.2$, or coupling 1060XP fiber from Thorlabs catalog to C-GIMF leads to $\eta \approx 4.27$ at 1060 nm wavelength. The major difference between the two-mode and five-mode scenarios is that at the higher value of $\tilde{\gamma} = 3$, τ experiences a much higher amplitude oscillation as a function of \tilde{L} in the five-mode case. The large amplitude oscillations in the five-mode scenario for $\tilde{\gamma} = 3$ are due to the efficient power transfer from the lowest order mode to the other four modes. Each mode accumulates a different linear and nonlinear phase as it propagates along the GIMF resulting in large variations in the relative power transmission, which is a sensitive function of both the amplitude and the phase of each mode [see Eq. (15)].

Finally, the case of $p_0 = 0.25$ for the five-mode scenario is considered in Fig. 12, which should be compared with the two-mode scenario in Fig. 5. This case corresponds to $\eta = 7 + \sqrt{48} \approx 13.9$, which is very hard to obtain using conventional fibers. Substantial power leakage into the radiation and cladding modes is observed in the five-mode scenario and the results contrast sharply from the two-mode scenario in Fig. 5. Because of the finite number of core-guided modes supported by the finite GIMF core [see Eq. (6)], which is truncated by the cladding at radius R , some of the power from the input SMF does not couple to the core-guided modes and couples to the cladding and radiation modes, as estimated in Eq. (21) and also discussed in [9]. The power leakage can be substantial for $\eta \gg 1$, as observed in Fig. 12. There is hardly any difference between the linear case ($\tilde{\gamma} = 0$) and $\tilde{\gamma} = 0.7$ in Fig. 12; however, for $\tilde{\gamma} = 3$, the relative power transmission nearly saturates over the entire value of \tilde{L} at τ_{\max} .

In summary, the NL-MMI related to $p_0 = 0.75$ in the five-mode scenario closely resembles that of the two-mode scenario presented in Subsection 3.A. This similarity is lost as the value of p_0 is lowered (via increasing η); however, a larger value of p_0 is generally more accessible using commercially available optical fibers. Fortunately, the power switching dynamics (from τ_{\min} to τ_{\max}) is more desirable for $p_0 = 0.75$ than $p_0 = 0.25$ in the SMF-GIMF-SMF geometry shown in Fig. 1.

4. SATURABLE ABSORBER USING NL-MMI

In Section 3, the NL-MMI behavior of the SMF-GIMF-SMF geometry of Fig. 1 was discussed in great detail. Here, the

results will be used to explore the application of this geometry as an SA. Specifically, it is desirable for the SMF-GIMF-SMF configuration to attenuate low power signals ($\tilde{\gamma} \approx 0$), but allow the higher power signals to go through. All analysis performed in this section is for the realistic case of five-modes (LG₀₀ through LG₄₀), subject to the constraint of Eq. (17) for the initial excitation amplitudes.

Figure 13 depicts the behavior of the relative power transmission τ as a function of $\tilde{\gamma}$ for a fixed value of $\tilde{L} = 4.5\pi$ in a SMF-GIMF-SMF configuration, for $p_0 = 0.5, 0.25, 0.75$ at $\zeta = 0$, in solid, dashed, and dotted lines. The value of \tilde{L} is chosen such that in the linear case, the relative power transmission is at its minimum value. In Subsection 3.B, it was pointed out that the case of $p_0 = 0.75$ is the most interesting scenario from an experimental point of view. For $p_0 = 0.75$, the relative power transmission increases from τ_{\min} to $\tau_{\max} \approx 1$ monotonically as $\tilde{\gamma}$ is increased from zero to $\tilde{\gamma} \approx 0.75$. Beyond $\tilde{\gamma} \approx 0.75$, τ goes through a few low amplitude oscillations and saturates at $\tau_{\max} \approx 1$. This is nearly an ideal scenario for an SA, where the only downside with this design is that τ_{\min} is considerably larger than zero.

For $p_0 = 0.5$ in Fig. 13, a slightly higher value of $\tilde{\gamma}$ is required compared with $p_0 = 0.75$ to achieve the maximum transmission; moreover, more oscillations are observed beyond the transmission peak value, which may not be a desirable feature for an SA. Another important feature of this plot is the large low-transmission plateau and the sudden rise of τ near the peak values, which is desirable for pulse shortening in an SA. The case of $p_0 = 0.25$ is also shown in Fig. 13; the peak value of transmission in this scenario is only near 50% due to power coupling to the radiation and cladding modes, as discussed in Subsection 3.B, making this an undesirable design. The results in Fig. 13 should be compared with the two-mode scenario in Fig. 8. A notable feature in Fig. 8 is the large-amplitude oscillations of τ as a function of $\tilde{\gamma}$; this behavior is very different from Fig. 13, where τ was nearly saturated to τ_{\max} beyond $\tilde{\gamma} \approx 0.75$ for $p_0 = 0.75$.

In Fig. 14, a similar case to the one discussed in Fig. 13 is considered, except for a longer GIMF section where $\tilde{L} = 100.5\pi$. Similarly, this value of \tilde{L} is chosen such that, in the linear case, the relative power transmission is at its minimum value. The most notable differences between the case of $\tilde{L} = 100.5\pi$ in Fig. 14 and $\tilde{L} = 4.5\pi$ in Fig. 13 are that τ_{\max} is obtained at a lower value of $\tilde{\gamma}$ for the longer GIMF design. This is somewhat expected, given that the nonlinear phase is

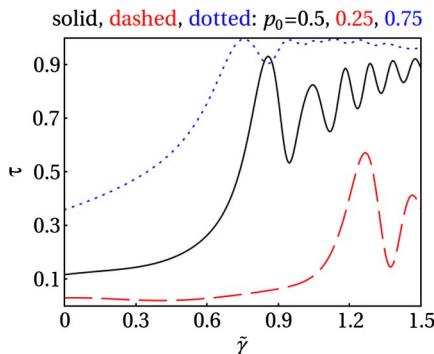


Fig. 13. Relative power transmission is plotted as a function of $\tilde{\gamma}$ (thus the total power) for $\tilde{L} = 4.5\pi$ for the case of five modes, when $p_0 = 0.5, 0.25, 0.75$ at $\zeta = 0$, in solid, dashed, and dotted lines, respectively.

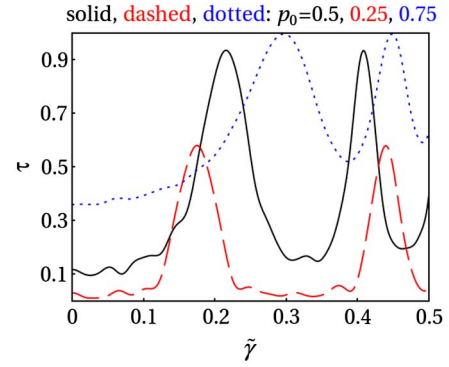


Fig. 14. Same as Fig. 13, except for $\tilde{L} = 100.5\pi$.

cumulative. However, comparing the five-mode scenario in Fig. 14 with the two-mode case of Fig. 9 shows that a much higher value of $\tilde{\gamma}$ is required in the five-mode scenario to obtain τ_{\max} ; therefore, the five-mode and two-mode scenarios differ substantially from each other.

In Figs. 13 and 14, the value of \tilde{L} is chosen such that $\tau = \tau_{\min}$ is obtained for $\tilde{\gamma} = 0$. While this may seem a reasonable choice, this is not required from an SA; rather, all that is required from an SA is to efficiently discriminate against low power signals with minimal impact on the high power. Therefore, it is necessary to examine other possibilities for \tilde{L} and find the most efficient SA that is possible with the SMF-GIMF-SMF geometry of Fig. 1. A relevant metric for the pulse power discrimination in an SA is the value of $(\delta\tau/\tau)$, which characterizes the sensitivity of an SA to a change in the pulse power.

Figure 15 shows $(\delta\tau/\tau)$, defined as

$$(\delta\tau/\tau) = \frac{1}{\tau}(\tau|_{\tilde{\gamma}=0.001} - \tau|_{\tilde{\gamma}=0}), \quad (22)$$

as a function of the normalized GIMF length. $(\delta\tau/\tau)$ is used as the metric because it is related to $(\partial\tau/\partial\tilde{\gamma})$ via $(\delta\tau/\tau) \approx \tau^{-1}(\partial\tau/\partial\tilde{\gamma})\delta\tilde{\gamma}$ for $\delta\tilde{\gamma} = 0.001$. The normalized length of the GIMF is chosen to be $\tilde{L} = 300\pi + \delta\tilde{L}$, and the horizontal axis in Fig. 15 is expressed as $\delta\tilde{L}$ in the range $[-\pi/2, +\pi/2]$. The reason for this limited range in $\delta\tilde{L}$ is that $(\delta\tau/\tau)$ repeats in a nearly periodic fashion outside this range, unless $\delta\tilde{L}$ becomes very large. It will be discussed later in Section 5 that

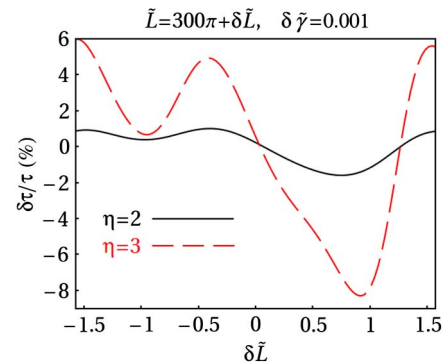


Fig. 15. Relative change in the normalized power transmission in the SMF-GIMF-SMF geometry defined in Eq. (22) plotted as a function of $\delta\tilde{L}$, where the length of the GIMF section is given by $\tilde{L} = 300\pi + \delta\tilde{L}$. A large positive value of $(\delta\tau/\tau)$ is desirable for saturable absorption. The plots are presented for $\eta = 2$ (solid) and $\eta = 3$ (dashed).

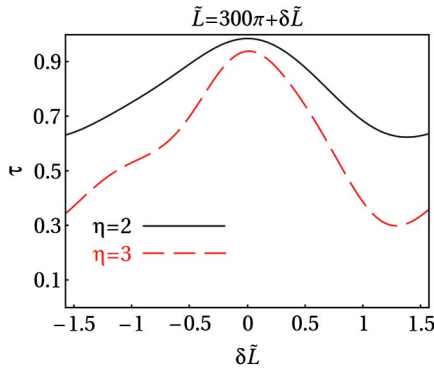


Fig. 16. Relative power transmission is shown as function of $\delta\tilde{L}$, where the length of the GIMF section is given by $\tilde{L} = 300\pi + \delta\tilde{L}$. τ presented in this figure is the average value between $\tau|_{\tilde{\gamma}=0.001}$ and $\tau|_{\tilde{\gamma}=0}$. This figure is intended to show that the value of τ is not too low near the peak value of $(\delta\tau/\tau)$ in Fig. 15. The plots are presented for $\eta = 2$ (solid) and $\eta = 3$ (dashed).

even a seemingly small value of $\tilde{\gamma} = 0.001$ can translate to multi-kilowatts of peak power in some commercial GIMFs, such as C-GIMF. Therefore, our main intention in choosing $\delta\tilde{\gamma} = 0.001$ in Eq. (22) and subsequent figures is to ensure that our design and observations are relevant for practical situations.

For both $\eta = 2$ (solid line) and $\eta = 3$ (dashed line) in Fig. 15, the maximum value of $(\delta\tau/\tau)$ is obtained at $\delta\tilde{L} \approx -0.4$, while the large low-transmission plateau already observed in Figs. 13 and 14 at near $\tilde{\gamma} = 0$ is responsible for the small value of $(\delta\tau/\tau)$ near $\delta\tilde{L} = 0$. The maximum value of $(\delta\tau/\tau)$ is around 1% for $\eta = 2$ and 5% for $\eta = 3$. It should be pointed out that SAs can be used to mode-lock lasers even when their modulation depth (MD) is as low as 0.5% [27]. MD is defined as the maximum change in transmission in an SA. Although MD is often the standard quantity used to assess the performance of SAs, the large values of MD obtained in the SMF-GIMF-SMF (between τ_{\min} and τ_{\max}) can be misleading, because a very high peak power may be needed to access the full range of the MD (some numerical values will be presented in Section 5). Therefore, $(\delta\tau/\tau)$ has been used in this paper and is identical to MD within the reasonably accessible range of pulse peak powers.

It is required to ensure that the total transmission through the SMF-GIMF-SMF geometry is not too low; in other words, the SA is not too lossy near the peak value of $(\delta\tau/\tau)$. In Fig. 16, the average value $(\tau|_{\tilde{\gamma}=0.001} + \tau|_{\tilde{\gamma}=0})/2$ is plotted as a function of $\delta\tilde{L}$ for $\eta = 2$ (solid line) and $\eta = 3$ (dashed line). It can be

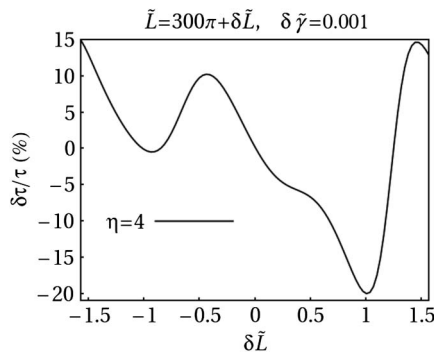


Fig. 17. Same as Fig. 15, except for $\eta = 4$.

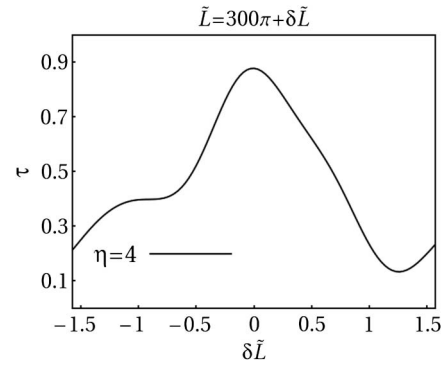


Fig. 18. Same as Fig. 16, except for $\eta = 4$.

seen that the average relative power transmission is reasonably large near the peak value of $(\delta\tau/\tau)$ of Fig. 15; therefore, the SA can be regarded as a viable design.

In Fig. 17, $(\delta\tau/\tau)$ is plotted in the same fashion as in Fig. 15, except for $\eta = 4$. The reason separate figures are used to plot $\eta = 2, 3$ and $\eta = 4$ is that the vertical scales are different. As can be seen in Fig. 17, $(\delta\tau/\tau)$ as large as 15% is possible in this case. While this may seem like a highly desirable SA, the relative power transmission plot for $\eta = 4$ in Fig. 18 shows that τ is quite small near the peak values of $(\delta\tau/\tau)$. Perhaps an optimum operation of this device can be accomplished at $\delta\tilde{L} \approx -0.3$ where $\delta\tau/\tau \approx 9\%$.

5. DISCUSSION AND CONCLUSION

In this paper, a detailed analysis of the NL-MMI behavior of the SMF-GIMF-SMF geometry shown in Fig. 1 has been presented. Recently, this setup was successfully used to create very low-loss couplers between two SMFs with very different mode-field diameters [9,10]. Here, it has been shown that the transmission through this coupler has a very interesting nonlinear behavior and can be potentially used for switching purposes or for saturable absorption in all-fiber mode-locked lasers.

The key parameters that affect the NL-MMI in this geometry are the ratio of the mode-field diameter of the LG₀₀ mode in GIMF to the mode-field diameters of the SMFs [characterized by η defined in Eq. (17)]; the length of the GIMF section (characterized by the relative length parameter \tilde{L}); the relative nonlinear coefficient $\tilde{\gamma}$, which incorporates the total power and nonlinear coefficient of the GIMF; and the total number of propagating modes in the GIMF.

It was observed that the best performances for switching and intensity discrimination applications, such as in SAs, can be obtained when the value of η defined in Eq. (17) is not too large; $\eta < 4$ seems like a reasonable choice. This is easily achievable for reasonable selection of commercially available fibers.

Like most other nonlinear devices, the interaction length plays a very important role in the behavior of the SMF-GIMF-SMF device. The dimensionless normalized length \tilde{L} has been used throughout this paper, which is the length of the GIMF normalized by $\beta_{(1)} - \beta_{(2)}$. This normalization factor is $(183 \mu\text{m})^{-1}$ for a C-GIMF operating at 1550 nm. Therefore, $\tilde{L} = 4.5\pi$, $\tilde{L} = 100.5\pi$, and $\tilde{L} = 300\pi$ used in this paper translate to $L = 2.6$ mm, 5.78, and 17.24 cm for the length of the GIMF section, which are all reasonable lengths for device applications. For SA purposes, $\tilde{L} = 300\pi + \delta\tilde{L}$ was explored in Figs. 15 and 17, where it was realized that some level of fine

tuning of the order of $\delta\tilde{L} \sim \pi$ is required, which is $\delta L \sim 575 \mu\text{m}$ for C-GIMF at 1550 nm wavelength. This situation is not different from that of Refs. [9,10], and the fact that the required fine-tuning range is so small means that it can be easily achieved by polishing the GIMF to the desired length. It should be emphasized that the problem of fine-tuning is not very serious and the length needs to be adjusted over a maximum one period of $\delta\tilde{L} \sim \pi$, because reducing \tilde{L} to $\tilde{L} - \pi$ shifts the periodic transmission pattern by one full period. Other pragmatic approaches can be taken instead of fine-tuning the length. For example, an ensemble of twenty SMF-GIMF-SMF couplers can be built around the same average GIMF length. Using this approach, the value of $\delta\tilde{L}$ will be uniformly distributed over the range of $[-\pi/2, +\pi/2]$ and one of the elements of the ensemble will likely perform up to the required specification.

The relative nonlinear coefficient $\tilde{\gamma}$ is defined in Eq. (12). For C-GIMF at 1550 nm wavelength, $\tilde{\gamma} = 1.0$ corresponds to a power of $\tilde{P} \approx 10.0$ MW, given that the nonlinear coefficient γ (defined for the LG₀₀ mode in GIMF) is smaller than that of the SMF-28 by a factor $\eta \approx 2.2$. For practical fiber-based mode-locking applications, this value is unacceptably large. The feasible range of operation for the peak power of a mode-locked fiber laser is from several to a likely maximum of a few hundred kW of peak power. If the GIMF is made from highly nonlinear material, e.g., chalcogenide glass with a nonlinear coefficient of up to 1000 times larger than silica, then $\tilde{\gamma} = 1.0$ will correspond to $\tilde{P} \approx 10.0$ kW.

The feasibility of using the SMF-GIMF-SMF geometry has been shown for SA applications, even for $\tilde{\gamma} = 0.001$, in Fig. 17, which corresponds to $\tilde{P} \approx 10.0$ kW using C-GIMF and SMF-28 commercial fibers at 1550 nm wavelength. Therefore, it is probable that the SMF-GIMF-SMF geometry can be used even with conventional commercially available fibers to mode-lock fiber lasers at the presently achievable power levels. The main advantage of this geometry is that it can be designed to operate at a much higher power level compared with the existing SAs that exploit nonlinear polarization rotation, semiconductors, or carbon nanotubes. Therefore, it might offer a very attractive solution for scaling up the pulse energy and peak power in mode-locked fiber lasers that are currently limited by the existing SA technology.

Throughout this paper, it was observed that having a smaller number of propagating modes in the GIMF is beneficial, especially in the design of an SA. While specific designs need to be carefully analyzed using the formalism laid out in this manuscript, this can be taken as a general guideline and highly multimode GIMFs should be avoided if possible. We do not think that the quality and the telecommunication bandwidth of the GIMF (e.g., due to the centerline defect [28]) has any appreciable effect on the NL-MMI behavior and the SA performance of the SMF-GIMF-SMF geometry.

Finally, we would like to comment on the possibility of exciting nonzero angular momentum modes, which are excluded from our analysis. It is possible to excite $m = \pm 1$ modes via coupling them to $m = 0$ modes by bending the GIMF. In order for the power exchange to operate efficiently in a resonant fashion, the phase mismatch between the $m = 0$ and $m = \pm 1$ must be compensated for by the bend; e.g., long-period gratings are optimized to provide this phase-matching condition [17]. However, in a GIMF, the $m = 0$ and $m = \pm 1$ modes always belong to different mode groups with a very large

mismatch in their propagation constants, according to Eq. (4). Therefore, a very small bending radius (submillimeter for C-GIMF) is required for efficient phase matching. Therefore, coupling between $m = 0$ and $m = \pm 1$ will not be an efficient process in GIMFs, unless assisted by specialty devices such as long-period gratings [17].

Coupling between $m = 0$ and $m = \pm 2$ is induced via the random variations in the diameter of the GIMF, caused by manufacturing errors [29], and can even happen within the same mode group with minimal phase matching issue. While this can be minimized by selecting a high quality GIMF, in practice this should not cause any issues for GIMFs shorter than approximately one meter in length.

It has also been previously shown that fabrication errors due to the misalignment of the fibers can be minimized to the extent where they do not have a noticeable impact on the linear operation of the device [10]. Similar robustness is expected in the nonlinear regime of operation.

ACKNOWLEDGMENTS

The authors acknowledge support from the Air Force Office of Scientific Research under Grant FA9550-12-1-0329.

REFERENCES

1. A. Mehta, W. S. Mohammed, and E. G. Johnson, "Multimode interference based fiber optic displacement sensor," *IEEE Photon. Technol. Lett.* **15**, 1129–1131 (2003).
2. W. S. Mohammed, A. Mehta, and E. G. Johnson, "Wavelength tunable fiber lens based on multimode interference," *J. Light-wave Technol.* **22**, 469–477 (2004).
3. W. S. Mohammed, P. W. E. Smith, and X. Gu, "All-fiber multimode interference band-pass filter," *Opt. Lett.* **31**, 2547–2549 (2006).
4. Q. Wang and G. Farrell, "All-fiber multimode-interference-based refractometer sensor: proposal and design," *Opt. Lett.* **31**, 317–319 (2006).
5. Y. O. Yilmaz, A. Mehta, W. S. Mohammed, and E. G. Johnson, "Fiber-optic beam shaper based on multimode interference," *Opt. Lett.* **32**, 3170–3172 (2007).
6. X. Zhu, A. Schülzgen, H. Li, L. Li, L. Han, J. V. Moloney, and N. Peyghambarian, "Detailed investigation of self-imaging in large-core multimode optical fibers for application in fiber lasers and amplifiers," *Opt. Express* **16**, 16632–16645 (2008).
7. X. Zhu, A. Schülzgen, L. Li, and N. Peyghambarian, "Generation of controllable nondiffracting beams using multimode optical fibers," *Appl. Phys. Lett.* **94**, 201102 (2009).
8. X. Zhu, A. Schülzgen, H. Li, H. Wei, J. V. Moloney, and N. Peyghambarian, "Coherent beam transformation using multimode waveguides," *Opt. Express* **18**, 7506–7520 (2010).
9. A. Mafi, P. Hofmann, C. Salvin, and A. Schülzgen, "Low-loss coupling between two single-mode optical fibers with different mode-field diameters using a graded-index multimode optical fiber," *Opt. Lett.* **36**, 3596–3598 (2011).
10. P. Hofmann, A. Mafi, C. J. Salvin, T. Tiess, N. Peyghambarian, and A. Schülzgen, "Detailed investigation of mode-field adapters utilizing multimode-interference in graded index fibers," *J. Light-wave Technol.* **30**, 2289–2298 (2012).
11. G. P. Agrawal, *Fiber-Optic Communication Systems*, 4th ed. (Wiley, 2011).
12. M. I. Dzhibladze, Z. G. Esiashvili, E. S. Teplitskii, S. K. Isaev, and V. R. Sagaradze, "Mode-locking in a fiber laser," *Kvantovaya Elektron.* **10**, 432–434 (1983).
13. L. F. Mollenauer and R. H. Stolen, "The soliton laser," *Opt. Lett.* **9**, 13–15 (1984).
14. D. Gloge and E. A. J. Marcattii, "Multimode theory of graded-core fibers," *Bell Syst. Tech. J.* **52**, 1563–1578 (1973).
15. K. Okamoto, *Fundamentals of Optical Waveguides*, 2nd ed. (Academic, 2006).

16. M. Mayeh and F. Farahi, "Laser beam shaping and mode conversion in optical fibers," *Photonic Sens.* **1**, 187–198 (2011).
17. M. Sumetsky and S. Ramachandran, "Multiple mode conversion and beam shaping with superimposed long period gratings," *Opt. Express* **16**, 402–412 (2008).
18. G. J. Liu, B. M. Liang, Q. Li, and G. L. Jin, "Beam propagation in nonlinear multimode interference waveguide," *J. Opt. A* **7**, 457–462 (2005).
19. G. I. Stegeman and E. M. Wright, "All-optical waveguide switching," *Opt. Quantum Electron.* **22**, 95–122 (1990).
20. H. G. Winful and D. T. Walton, "Passive mode locking through nonlinear coupling in a dual-core fiber laser," *Opt. Lett.* **17**, 1688–1690 (1992).
21. J. Proctor and J. N. Kutz, "Nonlinear mode-coupling for passive mode-locking: application of waveguide arrays, dual-core fibers, and/or fiber arrays," *Opt. Express* **13**, 8933–8950 (2005).
22. D. N. Christodoulides, F. Lederer, and Y. Silberberg, "Discretizing light behaviour in linear and nonlinear waveguide lattices," *Nature* **424**, 817–823 (2003).
23. R. H. Stolen, J. Botineau, and A. Ashkin, "Intensity discrimination of optical pulses with birefringent fibers," *Opt. Lett.* **7**, 512–514 (1982).
24. G. P. Agrawal, *Nonlinear Fiber Optics*, 5th ed. (Academic, 2012).
25. A. Mafi, "Pulse propagation in a short nonlinear graded-index multimode optical fiber," *J. Lightwave Technol.* **30**, 2803–2811 (2012).
26. A. Chong, J. Buckley, W. Renninger, and F. Wise, "All-normal-dispersion femtosecond fiber laser," *Opt. Express* **14**, 10095–10100 (2006).
27. F. Kartner, J. aus der Au, and U. Keller, "Slow and fast saturable absorbers for modelocking of solid state lasers—what's the difference?," *IEEE J. Sel. Top. Quantum Electron.* **4**, 159–168 (1998).
28. A. Mafi, "Bandwidth improvement in multimode optical fibers via scattering from core inclusions," *J. Lightwave Technol.* **28**, 1547–1555 (2010).
29. R. Olshansky, "Mode coupling effects in graded-index optical fibers," *Appl. Opt.* **14**, 935–945 (1975).

Nonlinear switching in multicore versus multimode waveguide junctions for mode-locked laser applications

Elham Nazemosadat and Arash Mafi*

Department of Electrical Engineering and Computer Science, University of Wisconsin-Milwaukee, Milwaukee, WI, 53211 USA

[*mafi@uwm.edu](mailto:mafi@uwm.edu)

Abstract: The main differences in nonlinear switching behavior between multicore versus multimode waveguide couplers are highlighted. By gradually decreasing the separation between the two cores of a dual-core waveguide and interpolating from a multicore to a multimode scenario, the role of the linear coupling, self-phase modulation, cross-phase modulation, and four-wave mixing terms are explored, and the key reasons are identified behind higher switching power requirements and lower switching quality in multimode nonlinear couplers.

© 2013 Optical Society of America

OCIS codes: (060.2310) Fiber optics; (190.4370) Nonlinear optics, fibers; (060.7140) Ultrafast processes in fibers; (080.1238) Array waveguide devices.

References and links

1. H. G. Winful and D. T. Walton, "Passive mode locking through nonlinear coupling in a dual-core fiber laser," *Opt. Lett.* **17**, 1688–1690 (1992).
2. J. L. Proctor and J. N. Kutz, "Passive mode-locking by use of waveguide arrays," *Opt. Lett.* **30**, 2013–2015 (2005).
3. D. D. Hudson, K. Shish, T. R. Schibli, J. N. Kutz, D. N. Christodoulides, R. Morandotti, and S. T. Cundiff, "Nonlinear femtosecond pulse reshaping in waveguide arrays," *Opt. Lett.* **33**, 1440–1442 (2008).
4. Q. Chao, D. D. Hudson, J. N. Kutz, and S. T. Cundiff, "Waveguide array fiber laser," *IEEE Photonics J.* **4**, 1438–1442 (2012).
5. E. Nazemosadat and A. Mafi, "Saturable absorption in multicore fiber couplers," *J. Opt. Soc. Am. B* **30** 2787–2790 (2013).
6. B. E. A. Saleh and M. C. Teich, *Fundamentals of Photonics*, 2nd ed. (Wiley, 2007).
7. S. M. Jensen, "The nonlinear coherent coupler," *IEEE J. Quantum Electron.* **18**, 1580–1583 (1982).
8. E. Nazemosadat and A. Mafi, "Nonlinear multimodal interference and saturable absorption using a short graded-index multimode optical fiber," *J. Opt. Soc. Am. B* **30**, 1357–1367 (2013).
9. F. Poletti and P. Horak, "Description of ultrashort pulse propagation in multimode optical fibers," *J. Opt. Soc. Am. B* **25**, 1645–1654 (2008).
10. A. Mafi, "Pulse propagation in a short nonlinear graded-index multimode optical fiber," *J. Lightwave Technol.* **30**, 2803–2811 (2012).

1. Introduction

The nonlinear switching (NLS) properties of waveguide arrays and multicore fiber couplers have recently attracted considerable attention for mode-locked fiber laser applications [1–5]. In the linear regime, where optical power is low, neighboring waveguides exchange optical power periodically; the linear coupling is caused by the modal overlap of adjacent waveguides and is most efficient when adjacent modes have identical propagation constants [6]. In the

nonlinear regime, where optical power is high, nonlinear effects alter the refractive index of each waveguide and consequently detune the effective propagation constants of the modes, reducing the power exchange efficiency between adjacent cores [7]. By only retaining the light in the launch waveguide at the output, it is possible to achieve power-dependent transmission and intensity discrimination required for mode-locked operation [1, 2].

Recently, it was shown that nonlinear multimodal interference in a graded-index multimode fiber has intensity discrimination properties as well and can be used for NLS [8]. However, it was observed that a much higher power is required for NLS based on the nonlinear multi-modal interference in multimode fibers compared to the NLS based on the nonlinear mode coupling in multicore fibers. Moreover, the NLS quality of the multimode fiber was shown to be inferior to those reported for multicore fibers.

The objective of this manuscript is to highlight the differences between the NLS behavior in multimode versus multicore waveguides. Several key questions are addressed: Why is higher power required to achieve NLS in multimode versus multicore waveguides? What is the main reason behind the inferior NLS quality in multimode waveguides? Is it because of the cross-phase modulation (XPM) and four-wave mixing (FWM) terms? Or because of the way the modes are excited in the multimodal junctions?

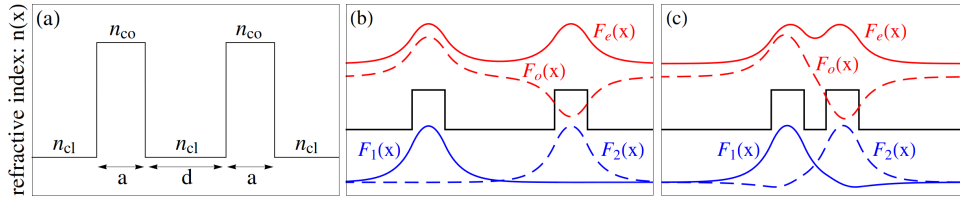


Fig. 1. (a) The refractive index profile of the double-waveguide nonlinear coupler is shown. (b) For weakly coupled waveguides ($d = 10\lambda$), the even and odd mode profiles $F_e(x)$ and $F_o(x)$ in *Picture-A* are sketched above the index profile and $F_1(x)$ and $F_2(x)$ in *Picture-B* are sketched below the index profile. (c) is similar to (b), except the waveguides are strongly coupled for $d = 2\lambda$. Results are shown for the TE polarization, where the transverse electric field vector is pointing in the vertical direction in these figures.

In order to present the arguments in a concrete model, NLS is explored for the Transverse Electric (TE) polarization in a pair of identical one-dimensional waveguides shown in Fig. 1(a). The design parameters are such that each waveguide supports only a single TE-polarization mode, with $n_{cl} = 1.5$, $n_{co} = 1.506$, and $a = 3\lambda$, where λ is the optical wavelength. We refer to the spatial transverse mode profile of a “single” waveguide as $F_w(x)$ throughout this paper.

In the linear regime, light propagation through this double-waveguide is commonly treated using the standard coupled-mode theory, which is valid as long as the waveguides are weakly coupled [6]. In Fig. 1(b) where the separation between the waveguides is $d = 10\lambda$, the standard coupled mode theory can be reliably applied to the individual modes of the waveguides whose profiles are identified as $F_1(x)$ and $F_2(x)$. The overlap between these modal profiles determines their coupling. However, a rigorous approach, which is applicable to both weak and strong coupling, is based on directly solving for the even and odd supermodes of the double-waveguide and treating the light propagation as a modal interference problem. The even and odd eigenmodes of the full index profile are sketched as $F_e(x)$ and $F_o(x)$ in Fig. 1(b). When the waveguides are only weakly coupled, the two approaches can be identically mapped to one another by $F_{1,2} = (F_e \pm F_o)/\sqrt{2}$. We will take this relationship as the definition of $F_1(x)$ and $F_2(x)$. Therefore, for the case of the weakly coupled waveguides, we can write $F_1 \equiv F_2 \equiv F_w$, where \equiv implies similarity up to a shift in the x-coordinate.

The case of the strongly coupled waveguides with $d = 2\lambda$ is shown Fig. 1(c), where $F_e(x)$ and $F_o(x)$ profiles are sketched as the exact eigenmodes of the system. The standard coupled

mode theory is not applicable here, and $F_1(x)$ and $F_2(x)$ profiles obtained from $F_{1,2}(x) = (F_e \pm F_o)/\sqrt{2}$ are far from the eigenmodes of the individual waveguides. In this case, $F_1 \neq F_2 \neq F_w$.

In this paper, the NLS behavior of the double-waveguide of Fig. 1(a) is studied as a function of the waveguide separation. This analysis provides an interpolation from the multicore to the multimode setup as the two waveguides are brought closer together and eventually merged. The NLS problem is initially treated using the generalized nonlinear Schrödinger equation (GNLSE) applied to the even and odd supermodes of the double-waveguide (F_e and F_o), which are the exact eigenmodes of the Helmholtz equation. This treatment is rigorous and is referred to as *Picture-A*. The nonlinear propagation problem is then transformed to the language of the $F_1(x)$ and $F_2(x)$ profiles, referred to as *Picture-B*. Although, $F_1(x)$ and $F_2(x)$ are not eigenmodes of the individual waveguides and take their meaning only from $F_e(x)$ and $F_o(x)$, the nonlinear propagation problem can be recast in their language with no loss of generality and both *Pictures* are equally valid. However, it will be seen that *Picture-B* is more suitable for the purposes of this paper, as the role of the XPM/FWM versus self-phase modulation (SPM) terms and the initial modal excitations are more clear in this *Picture*. This holds especially true in the limit of weakly coupled waveguides, where the XPM/FWM terms are completely absent in the nonlinear propagation equation in *Picture-B*.

2. The formulation and results

In what follows, only the continuous wave (CW) limit is considered, in order to reduce the complexity of the analysis and to ensure that the physics is not buried under phenomena that are not essential in conveying the intended message. However, the temporal effects can be easily included and the main observation will not be affected. The observations are general and equally apply, at least qualitatively, to Transverse Magnetic (TM) waves, and optical fibers.

In the coupled waveguide problem of Fig. 1(a), the lowest order modes are a pair of z-propagating bound states with the even and odd spatial profiles $F_e(x) = F_e(-x)$ and $F_o(x) = -F_o(-x)$ being invariant along the y-axis. The symmetries of these two profiles are dictated by the parity symmetry of the refractive index profile $n(x) = n(-x)$ and its invariance along the y-axis. The GNLSE describing the CW evolution of light in the two-mode double-waveguide in *Picture-A* can be written as [9, 10]

$$\frac{\partial A_\mu}{\partial z} = i\delta\beta_\mu A_\mu + i\left(\frac{n_2\omega_0}{c}\right) \sum_{\nu,\kappa,\rho=e,o} f_{\mu\nu\kappa\rho} A_\nu A_\kappa A_\rho^*, \quad \mu = e, o, \quad (1)$$

where $A_\mu(z)$ is the slowly varying envelope of the electric field of the μ th mode (even or odd mode) with the propagation constant β_μ . $P_\mu = |A_\mu|^2$ is the linear power density carried by this mode per unit y-length. The indices can take the value of e or o corresponding to even and odd modes. We also define $\delta\beta_e = -\delta\beta_o = \beta_e - \beta_{\text{ref}}$, where $\beta_{\text{ref}} = (\beta_e + \beta_o)/2$. The nonlinear coupling coefficients are given by

$$f_{\mu\nu\kappa\rho} = \int_{-\infty}^{\infty} F_\mu F_\nu F_\kappa F_\rho dx, \quad (2)$$

where the mutually orthogonal spatial profiles are assumed to be normalized according to $\int F_e^2 dx = \int F_o^2 dx = 1$. n_2 is the nonlinear index coefficient, and ω_0 is the carrier frequency. $f_{\mu\nu\kappa\rho}$ is a fully symmetric tensor, and f_{eooo} and f_{eeeo} vanish due to the parity symmetry.

In Fig. 2(a), $\delta\beta_e$ is plotted as a function of the normalized separation d/λ between the waveguides. At a large separation, the even and odd modes are nearly degenerate in the value of the propagation constant. However, $\delta\beta_e$ rapidly increases as the waveguides are brought closer together and the degeneracy between the even and odd modes is strongly broken.

In Fig. 2(b), the non-zero nonlinear coupling coefficients of the even and odd modes in *Picture-A* are plotted as a function of the normalized waveguide separation. The nonlinear coupling coefficients f_{eeee} , f_{eeoo} and f_{oooo} are equal when the two waveguides are far apart and

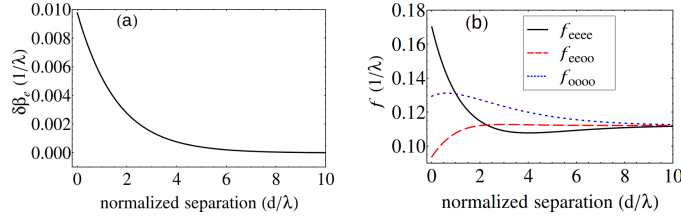


Fig. 2. (a) The splitting between the propagation constants of the modes increases significantly as the waveguides are brought closer together. (b) The nonlinear coupling coefficients for the even and odd modes are shown as a function of the normalized separation, where their degeneracy is removed when the waveguides are strongly interacting.

hence, weakly coupled. However, as the two waveguides get closer, the difference between the nonlinear couplings increases. Other elements of the $f_{\mu\nu\kappa\rho}$ tensor not shown in Fig. 2(b) are related to the plotted elements by symmetry relationships of the tensor; e.g., $f_{eoeo} = f_{eeoo}$.

The large values of the XPM/FWM terms in *Picture-A* complicate the analysis of the NLS. In *Picture-B*, the nonlinear propagation is more intuitive and the XPM/FWM terms are absent in the limit of weakly coupled waveguides. In *Picture-B*, the field amplitudes are defined as $\tilde{A}_{1,2} := (A_e \pm A_o)/\sqrt{2}$. The GNLSE Eq. (1) is transformed to

$$\frac{\partial \tilde{A}_j}{\partial z} = i\delta\beta_e \tilde{A}_{j'} + i \left(\frac{n_2 \omega_0}{c} \right) \sum_{k,l,m=1,2} f_{jklm} \tilde{A}_k \tilde{A}_l \tilde{A}_m^*, \quad j = 1, j' = 2, \text{ or } j = 2, j' = 1, \quad (3)$$

where the nonlinear coefficients f_{jklm} are given by

$$\begin{aligned} f_{1111} &= f_{2222} = (f_{eeee} + f_{oooo} + 6f_{eeoo})/4, \\ f_{1122} &= (f_{eeee} + f_{oooo} - 2f_{eeoo})/4, \quad f_{1112} = f_{1222} = (f_{eeee} - f_{oooo})/4. \end{aligned} \quad (4)$$

The results of Eq. (4) are consistent with the field profiles defined in *Picture-B* as $F_{1,2} = (F_e \pm F_o)/\sqrt{2}$, given $f_{jklm} = \int F_j F_k F_l F_m^* dx$ with $j, k, l, m = 1, 2$. f_{jklm} is a fully symmetric tensor. It remains invariant if all indices valued at 1 are changed to 2 and vice versa; e.g., $f_{1112} = f_{1222}$.

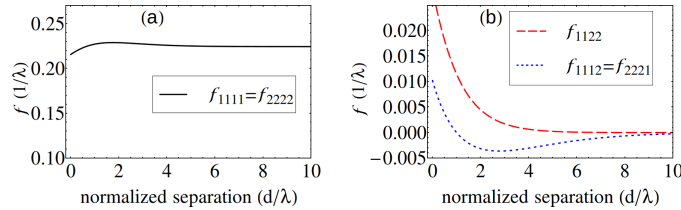


Fig. 3. The nonlinear coupling coefficients in *Picture-B* are shown as a function of d/λ . The SPM coefficients in (a) are much stronger than the XPM/FWM coefficients in (b).

The non-zero elements of f_{jklm} are plotted in Figs. 3(a) and 3(b). The SPM nonlinear coupling terms f_{1111} and f_{2222} are larger than the XPM/FWM terms by more than an order of magnitude, even when the two waveguides are merged. This behavior is dictated by the relationships presented in Eq. (4) and the near degeneracy of $f_{\mu\nu\kappa\rho}$ in Fig. 2(b), especially at weak coupling. Thus, in *Picture-B*, the nonlinear switching is dominated by SPM, which is easier to analyze.

The NLS behavior of the waveguide coupler is shown in Fig. 4. A multicore NLS configuration is sketched in Fig. 4(a), where the beam is injected into the two-core switch using an input coupler waveguide and is collected at an output coupler. The length of the nonlinear switch is equal to the half-beat-length L_h , so that at low powers, all the injected light is transferred to the second waveguide and no power is collected at the output. However, when the input power is

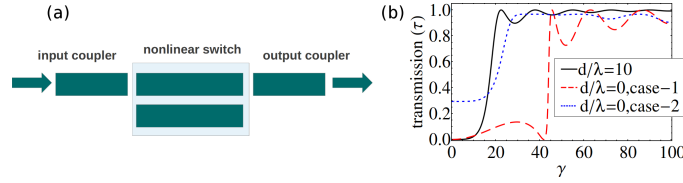


Fig. 4. (a) A sketch of the NLS device. (b) The relative power transmission is plotted as a function of γ . The solid (black) curve corresponds to weakly coupled waveguides with $d/\lambda = 10$. The dashed (red) and dotted (blue) NLS curves correspond to the strongly interacting merged waveguide with $d/\lambda = 0$, where in case-1 the injected and collected beam profiles are $F_1(x)$, while in case-2, the injected and collected beam profiles are $F_w(x)$.

increased, the nonlinearity detunes the coupling between the two waveguides and all the power is collected at the output port. This behavior is shown in Fig. 4(b), where the transmission τ is plotted as a function of the effective nonlinear coefficient defined as $\gamma = n_2 \omega_0 \tilde{P} / (c \delta \beta_e)$, where \tilde{P} is the linear optical power density injected from the input coupler.

In Fig. 4(b), the solid (black) line shows the NLS behavior of the double-waveguide coupler when the normalized separation is $d/\lambda = 10$. In this case, the injected and collected field profiles are assumed to be those of a single waveguide identical to the waveguides in the nonlinear coupler. The relative transmitted power can be obtained from [8]

$$\tau = \frac{1}{\tilde{P}^2} \left| \sum_{i=1,2} \tilde{A}_i^*(0) \tilde{A}_i(L_c) \right|^2 = \frac{1}{\tilde{P}^2} \left| \sum_{\mu=e,o} A_\mu^*(0) A_\mu(L_c) \right|^2, \quad (5)$$

where L_c is the total length of the nonlinear switch. In this case, the input boundary conditions (BC) for the GNLSE of Eq. (3) are $\tilde{A}_1(0)/\sqrt{\tilde{P}} = 1$ and $\tilde{A}_2(0)/\sqrt{\tilde{P}} = 0$. These BCs hold because the injected and collected beam profiles are $F_w(x)$ and is mode-matched to $F_1(x)$ of *Picture-B*, which is due to the weak coupling between the two waveguides.

When the waveguides are brought closer together, $F_1(x)$ can no longer be approximated as $F_w(x)$, as can also be seen in Fig. 1(c). In Fig. 4(b), the dashed (red) line shows the NLS behavior of the double-waveguide coupler, when the normalized separation is $d/\lambda = 0$, which is the limit of a standard single-core multimode coupler. In this case (case-1), the BCs are assumed to be $\tilde{A}_1(0)/\sqrt{\tilde{P}} = 1$ and $\tilde{A}_2(0)/\sqrt{\tilde{P}} = 0$. However, given the difference between $F_1(x)$ and $F_w(x)$ in this strong coupling regime, it is clear that these BCs cannot be achieved using an input coupler waveguide identical to those used in the nonlinear switch. In fact, the injected and collected beam profiles must be modified by additional optics (such as a spatial light modulator) or must come from special waveguides in order to mode-match to $F_1(x)$. Even if $F_1(x)$ is used for the injection, it might be more desirable to collect the beam directly from the nonlinear coupler in the form of $F_w(x)$. In this case, it is possible to slightly change the device length away from L_h to improve the coupling efficiency at high power at the expense of a perfect attenuation at low power (linear case). This is a reasonable trade-off because efficient transmission at high power is desired for mode-locked lasers while some level of compromise in nonlinear modulation depth is acceptable.

The difference between the dashed (red) line of $d/\lambda = 0$ compared with the solid (black) line of $d/\lambda = 10$ is caused by the XPM/FWM terms; if the XPM/FWM terms in Fig. 3(b) are artificially set to zero, the dashed (red) line in Fig. 4(b) falls almost exactly on the solid (black) line. The XPM/FWM terms nearly double the switching threshold in units of γ . However, given that $\delta \beta_e$ is nearly 555 times larger for $d/\lambda = 0$ than $d/\lambda = 10$ [see Fig. 2(a)], the switching threshold in the merged waveguides will become larger by the same factor when expressed in terms of power density instead of γ , because a factor of $\delta \beta_e$ is embedded in the definition of γ . The merged waveguides will have to be shorter by a factor of $\delta \beta_e$, because in *Picture-B*, $\delta \beta_e$ plays the role of the coupling between \tilde{A}_1 and \tilde{A}_2 as can be seen in Eq. (3), and because L_c must

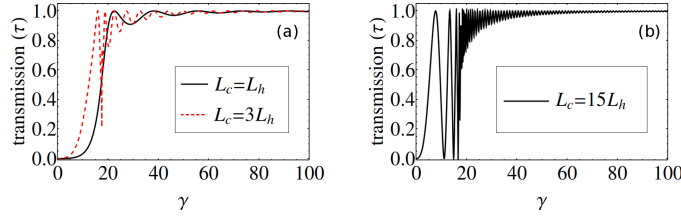


Fig. 5. The relative power transmission is plotted as a function of γ for (a) $L_c = L_h$ versus $L_c = 3L_h$ and (b) for $L_c = 15L_h$. The NLS quality for $L_c = 3L_h$ and $L_c = 15L_h$ are lower.

equal the half-beat-length L_h .

Injecting the double-waveguide coupler with a complex beam profile of $F_1(x)$ to obtain the $\tilde{A}_1(0)/\sqrt{\tilde{P}} = 1$ and $\tilde{A}_2(0)/\sqrt{\tilde{P}} = 0$ BCs may not be possible. In many situations, it is more practical to inject the beam from a waveguide that is identical to one of the waveguides in the multicore coupler. For the merged waveguides ($d/\lambda = 0$), this means that $F_w(x)$ is used as the injected and collected beam, instead of $F_1(x)$. We refer to this as case-2 and the NLS curve is shown as dotted (blue) in Fig. 4(b). Because the injected and collected beams are not properly mode-matched to the input and output couplers, respectively, both modes are excited (with different powers) and we need to use $\tilde{A}_1(0)/\sqrt{\tilde{P}} \approx 0.95$ and $\tilde{A}_2(0)/\sqrt{\tilde{P}} \approx 0.29$. Moreover, approximately 1.7% of the injected power is coupled to radiation modes. The modulation depth in the NLS curve in Fig. 4(b) for case-2 in dotted (blue) is lower because of the injection beam profile, resulting in a lower quality NLS.

We note that a linear switch can fully transfer the power from one waveguide to another if $L_c = nL_h$, where n is an odd integer. Therefore, all such linear switches are equivalent. However, in the nonlinear case the quality of the NLS is reduced for $n > 1$ as shown in Fig. 5 and undesired oscillations are observed before γ is sufficiently large for full power switching.

3. Conclusions

It is argued that the switching power threshold in nonlinear multimode junctions is larger than in multicore junctions, mainly because the value of $\delta\beta_e$ is substantially larger in the former case. The XPM/FWM terms also play a role in setting the power threshold but their importance is orders of magnitude lower than that of $\delta\beta_e$. When expressed in proper dimensionless parameters, the NLS curves are almost identical in a multimode and a multicore junction if the XPM/FWM terms are artificially switched off.

The presence of the XPM/FWM terms do not seem to play any essential role in the quality of the nonlinear switching curve of the multimode or multicore systems, especially in the value of the modulation depth. Rather, injection of the right combination of the modes at the input and the collection of the right combination of the modes at the output are the main factors behind the quality of the NLS curves. Creating the proper injection profile is often trivial in a weakly-coupled multicore waveguide; however, obtaining the right combination of the modes in a multimode junction is difficult, if not impossible, to achieve. Therefore, multimode junctions show lower quality NLS curves. This finding agrees with the observations reported in Ref. [8] and provides an intuitive explanation for those results.

Finite element method has been used to calculate the spatial profiles and propagation constants of the modes. Embedded nonlinear differential equation solvers in Mathematica have been used for the NLS simulations.

Acknowledgments

The authors acknowledge support from the Air Force Office of Scientific Research under Grant FA9550-12-1-0329 and are indebted to an anonymous reviewer for helpful comments.

Saturable absorption in multicore fiber couplers

Elham Nazemosadat and Arash Mafi*

*Department of Electrical Engineering and Computer Science, University of Wisconsin-Milwaukee,
Milwaukee, Wisconsin 53211, USA*

**Corresponding author: mafi@uwm.org*

Received August 20, 2013; accepted September 9, 2013;
posted September 16, 2013 (Doc. ID 196124); published October 3, 2013

The saturable absorption characteristics of two-, three-, and five-core one-dimensional fiber coupler arrays and the seven-core hexagonal fiber coupler array are investigated. It is shown that the performance of all these saturable absorbers is comparable and not much is gained, if anything, by going from a two-core nonlinear coupler geometry to a higher number of cores. This observation is supported by the similarity of the saturable absorption curves, as well as comparable pulse characteristics obtained from the simulation of a generic mode-locked fiber laser cavity. © 2013 Optical Society of America

OCIS codes: (060.2310) Fiber optics; (190.4370) Nonlinear optics, fibers; (060.7140) Ultrafast processes in fibers; (080.1238) Array waveguide devices.

<http://dx.doi.org/10.1364/JOSAB.30.002787>

1. INTRODUCTION

The operation of a mode-locked laser requires a form of intensity discrimination otherwise known as saturable absorption [1]. Common saturable absorbers (SAs) include semiconductor SA mirrors (SESAMs) [2], carbon nanotubes [3], graphene [4], Kerr lensing [5], and nonlinear polarization rotation (NPR) [6]. Desired attributes of SAs include fast response time (relaxation time), stability, long-term reliability, ease of use, appropriate saturation fluence, and low loss [7].

For mode-locked fiber laser applications, fully integrable SAs are desired in order to take full advantage of a robust alignment-free fiber cavity. Common fiber-integrable SA solutions have deficiencies that limit their usefulness for mode-locked fiber laser applications: SESAMs generally have picosecond response times, making them less desirable for ultrashort pulse generation, and their nonsaturable losses can result in excessive heating [8]. The long-term reliability of carbon nanotube- and graphene-based SAs when exposed to intense optical pulses is at best questionable [9], and both are limited in modulation depths. SAs based on NPR are very sensitive to the slightest perturbation of the fiber cavity, making them unsuitable outside the laboratory.

Another problem with the present SA technology concerns the rapid growth in the maximum achievable pulse energy and peak power in mode-locked fiber lasers over the past decade [10–12]. SAs are becoming a limiting factor in scaling up the pulse energy and peak power to higher values. SESAMs, carbon nanotubes, and graphene will likely not be suitable for ultrahigh pulse energies due to heat generation and long-term reliability. The periodic SA curve in a NPR SA with respect to the pulse power and its sensitivity to environmental perturbations makes this technique unsuitable for ultrahigh-peak-power mode-locked lasers.

Nonlinear mode coupling in waveguide arrays (NMCWA), including multicore fiber implementations, offers an attractive alternative that addresses most of the limitations faced by common SAs. A dual-core fiber laser geometry as an

embedded SA was originally proposed by Winful and Walton [13]. Since then, several theoretical studies have been conducted on nonlinear mode coupling in semiconductor coupled waveguide arrays [14–16], and multicore optical fibers [17,18]. More recently, a seven-core tapered optical fiber was explored in the nonlinear regime, and it was shown to have the potential to be used as an SA [19].

A mode-locked fiber laser using an AlGaAs waveguide array SA was recently demonstrated experimentally [20]. This demonstration clearly serves as a convincing experimental proof of concept for the potential application of NMCWA as an SA. However, for practical device applications and improved efficiency, the insertion loss of the waveguide array needs to improve. An all-fiber SA in the spirit of [13,17,18] seems like an ideal solution to the insertion loss problem, because it can be easily spliced to other components in the fiber cavity. Although semiconductor arrays benefit from a larger nonlinear coefficient resulting in desirably short SAs, fibers made from chalcogenide glasses with nonlinear coefficients of up to 1000 times larger than silica can provide similar performances [21,22]. In addition, the nearly instantaneous response of nonlinearities in optical fibers is ideal for ultrashort pulse generation [22,23].

In this paper, we study the performance of the multicore SAs as a function of the number of waveguide cores. Many-core geometries have been the center of attention in NMCWA SAs; e.g., the NMCWA studied in [14] has 41 coupled waveguides. We explore and compare the saturable absorption characteristics of two-, three-, and five-core one-dimensional (1D) arrays and the seven-core hexagonal array illustrated in Fig. 1. The main question that is addressed in this paper is whether increasing the number of cores improves the saturable absorption characteristics of these nonlinear multicore arrays.

The results indicate that the performance of all these SAs is comparable and not much is gained, if anything, by going from a two-core nonlinear coupler geometry to a higher number of cores. This observation is supported by the similarity of the

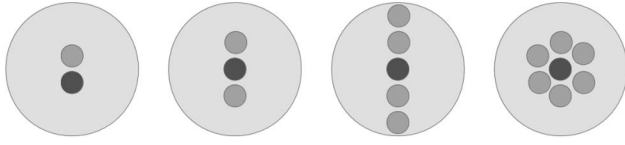


Fig. 1. Two-, three-, and five-core 1D arrays and the seven-core hexagonal array are shown in a fiber-optic geometry. All cores are assumed to be identical in a given geometry. The launch core is identified with a darker shade.

saturable absorption curves, as well as comparable pulse characteristics obtained from the simulation of a generic mode-locked fiber laser cavity. In the latter case, these SAs are placed in a fiber laser cavity, in which self-starting stable mode-locked pulses are generated. According to the results, one can benefit from the simpler setup of a two-core fiber with optimized parameters to get the desired output mode-locked pulses instead of using the more complex multicore fibers.

In the following, for each multicore fiber SA in Fig. 1, the optical beam is launched in the *launch core* identified with a darker shade and is collected from the same core at the other end after propagating through the length of the SA. The dependence of the transmission through the multicore fiber on the optical power serves as the desired saturable absorption mechanism.

2. DISCUSSION

In the linear regime where optical power is low, neighboring waveguides exchange optical power periodically; the linear coupling is caused by the modal overlap of adjacent waveguides and is most efficient when the adjacent modes have identical propagation constants [24]. In Fig. 2, the transmission through the multicore arrays of Fig. 1 is shown in the linear regime as a function of the normalized length L relative to \tilde{c}^{-1} ; \tilde{c} is the linear coupling coefficient between adjacent cores and is assumed to be the same among all neighboring cores in a given geometry. The half-beat length L_c is defined as the distance over which the energy is maximally exchanged from the launch core to the neighboring cores and depends on the number of fiber cores and the geometry.

It can be seen that the half-beat length of a three-core fiber is shorter than the two-core fiber, because its launch core is coupled to “more” side cores with the same strength and can exchange the optical power more efficiently. The linear dynamics in the case of five cores is a bit more complex due

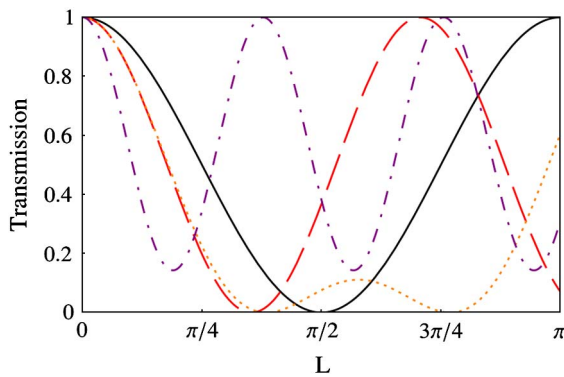


Fig. 2. Transmission through the two-core (solid black), three-core (dashed red), and five-core (dotted orange) fiber 1D arrays and the seven-core hexagonal array (dashed-dotted purple) is shown as a function of the normalized length in the linear regime.

to the differing power exchange efficiencies of the side cores, but the first minimum happens for only a slightly longer SA device. In the case of the seven-core hexagonal array, the central core couples to six cores in the outer ring, resulting in a rapid exchange of optical power and shorter half-beat length; however, the power in the central core always remains larger than zero where the minimum value of transmission is $1/7 \approx 14.3\%$. In all these cases, the half-beat length is inversely proportional to the coupling strength and is given by $\tilde{c}L_c = \xi_n(\pi/2)$, where ξ_n is a numerical coefficient for the n -core scenarios studied here. We have $\xi_2 = 1$, $\xi_3 = 1/\sqrt{2} \approx 0.71$, $\xi_5 = 4/\sqrt{27} \approx 0.77$, and $\xi_7 \approx 0.378$.

In the nonlinear regime where optical power is high, self-phase and cross-phase modulation (SPM and XPM) effects alter the refractive index of each waveguide and consequently detune the effective propagation constants of the modes, reducing the power exchange efficiency between adjacent cores [25]. In other words, if high power is launched into a waveguide, the effective couplings to neighboring cores are reduced and the light remains mainly in the launch core. If the total length of the coupler in each case is chosen to be equal to the half-beat length, for an optical pulse transmitting through the fiber array, its low intensity sides are efficiently channeled to the adjacent cores, while its high intensity center peak remains in the launch core, resulting in a power-dependent transmission and intensity discrimination [13,14]. This saturable absorption feature can be used to produce the required pulse shaping for stable and robust mode-locked pulse trains.

The differential equation describing the propagation of the electric field in the n th core of a multicore fiber nonlinear coupler, where only the interactions between the nearest neighbors are considered, is given by

$$\frac{\partial E_n}{\partial \zeta} = i \sum_{\tilde{n}} E_{\tilde{n}} + i \tilde{\gamma}_n |E_n|^2 E_n + i \sum_{\tilde{n}} \mu_{n,\tilde{n}} |E_{\tilde{n}}|^2 E_n. \quad (1)$$

E_n is the electric field envelope normalized to the pulse peak power P_0 at the entrance of the launch core. The \tilde{n} sums are over the cores adjacent to the n th core. The propagation distance is rescaled to $\zeta = \tilde{c}z$. $\tilde{\gamma}_n = \gamma_n^* P_0 / \tilde{c}$ is a dimensionless parameter characterizing the nonlinear strength, where γ_n^* is the SPM coefficient of the n th core and $\mu_{n,\tilde{n}}$ is the XPM coefficient between the n th core and the adjacent cores. The XPM terms are much smaller than the SPM terms and are thus neglected, i.e., $\mu_{n,\tilde{n}} \approx 0$. The dispersion and loss of the fiber coupler can be neglected if the SA length is sufficiently smaller than its dispersion length and effective length [23].

The nonlinear consequences of the coupled beam propagation in multicore arrays have been previously explored in detail, e.g., in [26]. Here, we borrow from these studies to obtain the saturable absorption curves of the multicore arrays of Fig. 1. The length of each SA array is assumed to be equal to the half-beat length to ensure minimum transmission in the low-power linear regime. The saturable absorption curves are shown in Fig. 3 where the transmission through the launch core of the multicore SA array is plotted as a function of the normalized nonlinear strength $\tilde{\gamma}$, which is assumed to be the same for all cores. The saturable absorption is dictated by a competition between the linear coupling term $i \sum_{\tilde{n}} E_{\tilde{n}}$ versus the nonlinear SPM term $i \tilde{\gamma}_n |E_n|^2 E_n$ in Eq. (1), and the transition from low transmission to high transmission occurs when these two terms are comparable.

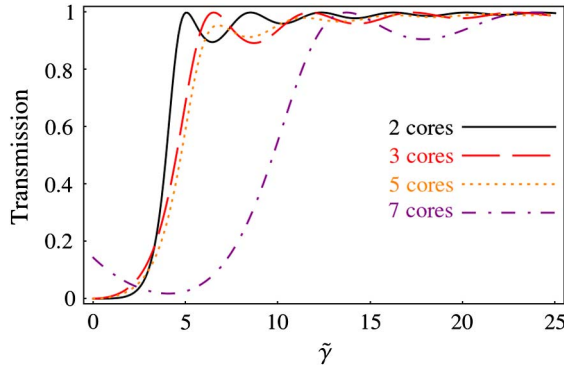


Fig. 3. Nonlinear transmission through two-core (solid black), three-core (dashed red), five-core (dotted orange) fiber 1D arrays and the seven-core hexagonal array (dashed-dotted purple) is shown as a function of the normalized nonlinear strength $\tilde{\gamma}$, which is assumed to be the same for all cores. The length of each SA array is chosen to be equal to the half-beat length.

The three-core fiber SA has two adjacent cores coupled to its launch core and consequently has a larger linear coupling term compared with the two-core scenario; therefore, more optical power (larger SPM term) is required to overcome the linear coupling term. That is why the three-core SA requires slightly higher power for nonlinear saturation. The five-core and three-core scenarios are nearly identical, because even in the five-core scenario, the launch core is only adjacent to two neighboring cores. The saturable absorption curves for a higher number of cores in 1D linear arrays are practically identical to the five-core SA.

For the seven-core hexagonal array SA, the nonlinear SPM term must overcome the linear coupling to six adjacent cores and requires higher normalized nonlinearity to saturate the SA. However, the SA curve closely resembles those of 1D arrays and can be mapped to the 1D saturable absorption curves by adjusting the core-to-core \tilde{c} coefficient. In fact, if SA devices are chosen at the same length, where \tilde{c} must inevitably be smaller for the seven-core array, the saturable absorption curves for all the geometries in Fig. 1 will be nearly identical as a function of the input power. This can easily be seen if the “horizontal scale” for the seven-core SA curve in Fig. 1 is rescaled by a factor of approximately 2/6 to compensate for the six adjacent cores versus the two adjacent cores in the three-core fiber. The SA curves nearly overlap after such a rescaling. This fact will result in nearly identical pulse characteristics in the mode-locked cavity simulations of Fig. 4, as will be discussed shortly.

There is another notable difference in the seven-core SA: the transmission initially drops to zero at finite $\tilde{\gamma}$ before saturating at higher power. This effect is due to the complex coupling pattern in the seven-core geometry. A nearly monotonic increase can be artificially created by shortening the fiber below the half-beat length at the expense of a smaller modulation depth.

To study the mode-locking behavior of the multicore array, it is placed within the mode-locking optical cavity. A typical passive mode-locked fiber laser consists of an active single-mode fiber with a bandwidth-limited gain, which compensates for the energy loss in the cavity, and an intensity discrimination device as an SA. When the interactions of the attenuation, chromatic dispersion, nonlinearity, and bandwidth-limited

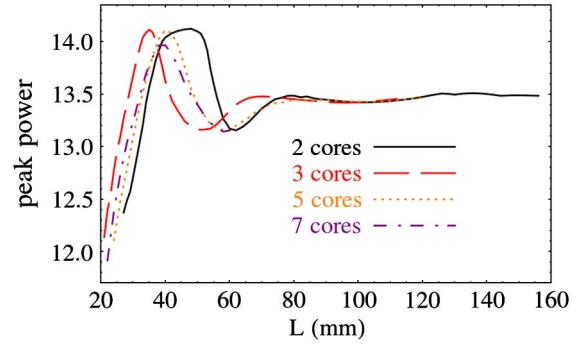


Fig. 4. Normalized peak power of the mode-locked pulses is shown as a function of the length of the SA, where the core-to-core coupling coefficients c are adjusted so that the length of the SA is equal to the half-beat length.

gain in the optical fiber cavity are combined with the intensity discrimination, a train of mode-locked pulses is formed from white noise after several numbers of round trips in the cavity. These interactions are captured by two sets of equations: one is the nonlinear Schrödinger equation governing the pulse propagation in the cavity, while the other is Eq. (1), describing the saturable absorption.

The pulse propagation in the cavity is given by [27]

$$\frac{\partial A}{\partial z} = -\alpha A + \frac{i}{2} \frac{\partial^2 A}{\partial T^2} + i\eta |A|^2 A + g(z) \left(1 + \tau \frac{\partial^2}{\partial T^2} \right) A, \quad (2)$$

where $A(z, T)$ is the normalized electric field envelope, z is the propagation distance along the fiber, and T represents the time measured in the retarded frame of the pulse normalized by a constant T_0 , which is the expected pulse duration. $A(z, T)$ is normalized by the peak power of the fundamental soliton $P_{\text{fs}} = |\beta_2|/(\gamma T_0^2)$, where β_2 is the group velocity dispersion of the fiber, and γ is the fiber nonlinear coefficient [23].

It is also implicitly assumed that the wavelength of the pulse $\lambda_0 = 1.55 \mu\text{m}$ falls within the anomalous-dispersion regime of the fiber. The propagation distance z is scaled to the dispersion length $L_D = T_0^2/|\beta_2|$, and η is the dimensionless cavity nonlinear coefficient given by $\eta = \gamma P_{\text{fs}} L_D$. The normalized attenuation is considered through α , while the bandwidth-limited gain of the cavity is described by the parameters $g(z)$ and τ . The dimensionless parameter τ controls the pulsewidth in the mode-locking process and is given by $\tau = 1/(\Delta\omega T_0)^2$, where $\Delta\omega = (2\pi c/\lambda_0^2)\Delta\lambda$ is the spectral gain bandwidth and $\Delta\lambda$ is the gain bandwidth [28]. The gain saturation $g(z)$ is given by

$$g(z) = \frac{2g_0}{1 + \|A\|^2/e_0}, \quad (3)$$

where g_0 and e_0 are the pumping strength and the cavity saturation energy, respectively, and $\|A\|^2 = \int_{-\infty}^{\infty} |A|^2 dT$ is the pulse energy.

The simulations are based on Eq. (2), while Eq. (1) is applied in every round trip of the laser cavity. The coupling efficiency of the cavity to the launch core of the multicore SA is assumed to be 100% on both the entrance and the exit ports; therefore, A in Eq. (2) becomes E at the entrance in the launch core of the multicore geometry in Eq. (1) and vice versa at the exit.

For the mode-locking cavity simulations, the initial pulse conditions are assumed to be low-amplitude noise fluctuations. The cavity length is 5 m, while the rest of the parameters used are $T_0 = 114$ fs, $\alpha = 0.05$, $\Delta\lambda = 35$ nm, $g_0 = 0.39$, and $e_0 = 1$ [28]. We also have $\beta_2 = -0.0153$ ps²/m resulting in $L_D = 0.84$ m. The nonlinear coefficient of the cavity is chosen as $\gamma = 1.7$ km⁻¹ W⁻¹. The nonlinear coefficient of the SA is assumed to be $\gamma^* = 0.34$ m⁻¹ W⁻¹, which can be obtained by using a chalcogenide glass fiber [21].

Figure 4 shows the normalized power of the mode-locked pulses after 100 round trips in the laser cavity, resulting in full convergence, as a function of the length the SA. For each length (and for each SA), the core-to-core coupling coefficients \tilde{c} are adjusted so that the length of the SA is equal to the half-beat length for optimum performance. This choice of the coupling coefficients ensures that the power is maximally transferred from the launch core to the other cores in the linear regime. In practice, the core-to-core coupling coefficients \tilde{c} can be designed and controlled via core-to-core separations. As we discussed above, the saturable absorption curves for all multicore arrays studied here are nearly identical when the SAs are of the same length. Therefore, it should come as no surprise that the normalized pulse peak power is nearly the same for all these SAs as shown in Fig. 4.

In summary, the results in Figs. 3 and 4 show that nearly identical performance is expected from the geometries that are explored in this manuscript. While that results are seemingly generic for popular SA geometries, we emphasize that this study is not exhaustive. An infinite number of multicore geometries can be constructed even with nonuniform core-to-core couplings and nonidentical core sizes applied to many different choices of laser parameters. Therefore, the main conclusion one can draw from this study is that when an NMCWA is to be used as an SA, it is important to verify whether multiple cores yield any tangible performance benefits besides making the device unnecessarily more complex. Future efforts will focus on comparisons between multimode and multicore all-fiber SA devices [29].

ACKNOWLEDGMENTS

The authors acknowledge support from the Air Force Office of Scientific Research under Grant FA9550-12-1-0329.

REFERENCES

- B. K. Garside and T. K. Lim, "Laser mode locking using saturable absorbers," *J. Appl. Phys.* **44**, 2335–2342 (1973).
- U. Keller, K. J. Weingarten, F. X. Kartner, D. Kopf, B. Braun, I. D. Jung, R. Fluck, C. Honninger, N. Matuschek, and J. Aus der Au, "Semiconductor saturable absorber mirrors (SESAM's) for femtosecond to nanosecond pulse generation in solid-state lasers," *IEEE J. Sel. Top. Quantum Electron.* **2**, 435–453 (1996).
- S. Y. Set, H. Yaguchi, Y. Tanaka, and M. Jablonski, "Laser mode locking using a saturable absorber incorporating carbon nanotubes," *J. Lightwave Technol.* **22**, 51–56 (2004).
- T. Hasan, Z. Sun, F. Wang, F. Bonaccorso, P. H. Tan, A. G. Rozhin, and A. C. Ferrari, "Nanotube-polymer composites for ultrafast photonics," *Adv. Mater.* **21**, 3874–3899 (2009).
- D. E. Spence, P. N. Kean, and W. Sibbett, "60 fsec pulse generation from a self-mode-locked Ti:sapphire laser," *Opt. Lett.* **16**, 42–44 (1991).
- D. U. Noske, N. Pandit, and J. R. Taylor, "Subpicosecond soliton pulse formation from self-mode-locked erbium fibre laser using intensity dependent polarisation rotation," *Electron. Lett.* **28**, 2185–2186 (1992).
- M. Haiml, R. Grange, and U. Keller, "Optical characterization of semiconductor saturable absorbers," *Appl. Phys. B* **79**, 331–339 (2004).
- R. Paschotta, J. Aus der Au, G. J. Spühler, F. Morier-Genoud, R. Hövel, M. Moser, S. Erhard, M. Karszewski, A. Giesen, and U. Keller, "Diode-pumped passively mode-locked lasers with high average power," *Appl. Phys. B* **70**, S25–S31 (2000).
- Y. W. Song, S. Yamashita, and S. Maruyama, "Single-walled carbon nanotubes for high-energy optical pulse formation," *Appl. Phys. Lett.* **92**, 021115 (2008).
- B. Ortac, M. Baumgartl, J. Limpert, and A. Tunnermann, "Approaching microjoule-level pulse energy with mode-locked femtosecond fiber lasers," *Opt. Lett.* **34**, 1585–1587 (2009).
- S. Lefrancois, K. Kieu, Y. Deng, J. D. Kafka, and F. W. Wise, "Scaling of dissipative soliton fiber lasers to megawatt peak powers by use of large-area photonic crystal fiber," *Opt. Lett.* **35**, 1569–1571 (2010).
- S. Lefrancois, C.-H. Liu, M. L. Stock, T. S. Sosnowski, A. Galvanauskas, and F. W. Wise, "High-energy similariton fiber laser using chirally coupled core fiber," *Opt. Lett.* **38**, 43–45 (2013).
- H. G. Winful and D. T. Walton, "Passive mode locking through nonlinear coupling in a dual-core fiber laser," *Opt. Lett.* **17**, 1688–1690 (1992).
- J. L. Proctor and J. N. Kutz, "Passive mode-locking by use of waveguide arrays," *Opt. Lett.* **30**, 2013–2015 (2005).
- H. S. Eisenberg, Y. Silberberg, R. Morandotti, A. R. Boyd, and J. S. Aitchison, "Discrete spatial optical solitons in waveguide arrays," *Phys. Rev. Lett.* **81**, 3383–3386 (1998).
- D. D. Hudson, K. Shish, T. R. Schibli, J. N. Kutz, D. N. Christodoulides, R. Morandotti, and S. T. Cundiff, "Nonlinear femtosecond pulse reshaping in waveguide arrays," *Opt. Lett.* **33**, 1440–1442 (2008).
- S. R. Friberg, A. M. Weiner, Y. Silberberg, B. G. Sfez, and P. S. Smith, "Femtosecond switching in a dual-core-fiber nonlinear coupler," *Opt. Lett.* **13**, 904–906 (1988).
- A. Betlej, S. Suntsov, K. G. Makris, L. Jankovic, D. N. Christodoulides, G. I. Stegeman, J. Fini, R. T. Bise, and D. J. DiGiovanni, "All-optical switching and multifrequency generation in a dual-core photonic crystal fiber," *Opt. Lett.* **31**, 1480–1482 (2006).
- T. F. S. Büttner, D. D. Hudson, E. C. Mägi, A. Casas Bedoya, T. Taunay, and B. J. Eggleton, "Multicore, tapered optical fiber for nonlinear pulse reshaping and saturable absorption," *Opt. Lett.* **37**, 2469–2471 (2012).
- Q. Chao, D. D. Hudson, J. N. Kutz, and S. T. Cundiff, "Waveguide array fiber laser," *IEEE Photon. J.* **4**, 1438–1442 (2012).
- G. Lenz, J. Zimmermann, T. Katsufuji, M. E. Lines, H. Y. Hwang, S. Spälter, R. E. Slusher, S.-W. Cheong, J. S. Sanghera, and I. D. Aggarwal, "Large Kerr effect in bulk Se-based chalcogenide glasses," *Opt. Lett.* **25**, 254–256 (2000).
- N. Sugimoto, H. Kanbara, S. Fujiwara, K. Tanaka, Y. Shimizugawa, and K. Hirao, "Third-order optical nonlinearities and their ultrafast response in Bi₂O₃-B₂O₃-SiO₂ glasses," *J. Opt. Soc. Am. B* **16**, 1904–1908 (1999).
- G. P. Agrawal, *Nonlinear Fiber Optics*, 5th ed. (Elsevier, 2013).
- B. E. A. Saleh and M. C. Teich, *Fundamentals of Photonics*, 2nd ed. (Wiley, 2007).
- S. M. Jensen, "The nonlinear coherent coupler," *IEEE J. Quantum Electron.* **18**, 1580–1583 (1982).
- D. N. Christodoulides and R. I. Joseph, "Discrete self-focusing in nonlinear arrays of coupled waveguides," *Opt. Lett.* **13**, 794–796 (1988).
- H. A. Haus, "Mode-locking of lasers," *IEEE J. Sel. Top. Quantum Electron.* **6**, 1173–1185 (2000).
- J. L. Proctor and J. N. Kutz, "Nonlinear mode-coupling for passive mode-locking: application of waveguide arrays, dual-core fibers, and/or fiber arrays," *Opt. Express* **13**, 8933–8950 (2005).
- E. Nazemosadat and A. Mafi, "Nonlinear multimodal interference and saturable absorption using a short graded-index multimode optical fiber," *J. Opt. Soc. Am. B* **30**, 1357–1367 (2013).

SRS generation spanning over two octaves in a graded-index multimode optical fiber

Hamed Pourbeyram,¹ Govind P. Agrawal,² and Arash Mafi^{1,*}

¹*Department of Electrical Engineering and Computer Science, Univ. of Wisconsin-Milwaukee, Milwaukee, WI 53211, USA*

²*The Institute of Optics, University of Rochester, Rochester, NY 14627, USA*

[*mafi@uwm.edu](mailto:mafi@uwm.edu)

Abstract: We report on the generation of new wavelengths, mediated by the stimulated Raman scattering process and extending over two octaves covering 523 to 1750 nm wavelength range, in a standard telecommunication graded-index multimode optical fiber. Despite the highly multimode nature of the pump, the Raman peaks are generated in specific modes of the fiber, confirming substantial beam cleanup during the stimulated Raman scattering process.

© 2013 Optical Society of America

OCIS codes: (060.4370) Nonlinear optics, fibers; (290.5910) Scattering, stimulated Raman.

References and links

1. R. H. Stolen, E. P. Ippen, and A. R. Tynes, "Raman oscillation in glass optical waveguide," *Appl. Phys. Lett.* **20**, 62–64 (1972).
 2. L. G. Cohen and C. Lin, "A universal fiber-optic (UFO) measurement system based on a near-IR fiber Raman laser," *IEEE J. Quantum Electron.* **QE-14**, 855–859 (1978).
 3. G. Rosman, "High-order comb spectrum from stimulated Raman scattering in a silica-core fibre," *Opt. Quantum Electron.* **14**, 92–93 (1982).
 4. F. Couny, F. Benabid, P. J. Roberts, P. S. Light, M. G. Raymer, "Generation and photonic guidance of multi-octave optical-frequency combs," *Science* **318** 1118–1121 (2007).
 5. G. P. Agrawal, *Nonlinear Fiber Optics*, 5th ed. (Academic Press, 2012).
 6. R. H. Stolen, J. E. Bjorkholm, and A. Ashkin, "Phase-matched three-wave mixing in silica fiber optical waveguides," *Appl. Phys. Lett.* **24**, 308–310 (1974).
 7. J. Cheng, M. E. V. Pedersen, K. Charan, K. Wang, C. Xu, L. Gruner-Nielsen, and D. Jakobsen, "Intermodal four-wave mixing in a higher-order-mode fiber," *Appl. Phys. Lett.* **101**, 161106–161109 (2012).
 8. A. Mafi, "Pulse propagation in a short nonlinear graded-index multimode optical fiber," *J. Lightwave Technol.* **30**, 2803–2811 (2012).
 9. A. Polley and S. E. Ralph, "Raman amplification in multimode fiber," *IEEE Photon. Technol. Lett.* **19**, 218–220 (2007).
 10. J. M. Dudley and J. R. Taylor, *Supercontinuum Generation in Optical Fibers*, 1st ed. (Cambridge University Press, 2010).
 11. A. Sharma, M. Dokhanian, Z. Wu, A. Williams, and P. Venkateswarlu, "Four-photon-mixing-mediated stimulated Raman scattering in a multimode optical fiber," *Opt. Lett.* **19**, 1122–1124 (1994).
 12. N. B. Terry, T. G. Alley, and T. H. Russell, "An explanation of SRS beam cleanup in graded-index fibers and the absence of SRS beam cleanup in step-index fibers," *Opt. Express* **15**, 17509–17519 (2007).
 13. K. S. Chiang, "Stimulated Raman scattering in a multimode optical fiber: evolution of modes in Stokes waves," *Opt. Lett.* **17**, 352–354 (1992).
-

1. Introduction

Stimulated Raman scattering (SRS) is a well-known nonlinear process with numerous applications including optical amplifiers, tunable lasers, spectroscopy, meteorology, and optical coherence tomography. SRS was first observed in silica glass fibers in 1972 by Stolen et al. [1]. They used a frequency-doubled, pulsed, Nd:YAG laser operating at the 532 nm wavelength to pump a single-mode optical fiber and observed Stokes emission at 545 nm. Since then, several groups have reported the observation of SRS in optical fibers using various configurations. For example, Cohen and Lin [2] generated 6 cascaded Raman peaks in a silica fiber, pumped by a mode-locked, Q-switched, Nd:YAG laser operating at 1064 nm. Rosman [3] observed 15 orders of cascaded Raman peaks by pumping a silica fiber at 532 nm with a frequency-doubled Nd:YAG laser. Other configurations involving unconventional fibers have been used for extreme Raman-comb generation. For example, Couny et al. [4] demonstrated the generation of a Raman comb spanning wavelengths from 325 nm to 2300 nm in a 1-m-long hydrogen-filled hollow-core photonic crystal fiber.

In this article, we report on the generation of new wavelengths, mediated by the SRS process and spanning over two octaves, in a standard graded-index multimode fiber (GIMF). The GIMF is pumped at a wavelength of 523 nm, and an optical-frequency Raman comb is generated on the Stokes side of the pump. At high power levels the measured spectrum extends up to 1750 nm, which is the upper detection limit of our optical spectrum analyzer (OSA). The generation of such a wide wavelength range, covering two octaves from 523 to 1750 nm, using a large-core telecommunication-grade multimode fiber distinguishes our results from those carried out in small-core or highly customized optical fibers.

Multimode optical fibers are easy to handle and are also easy to align to external sources; however, their large core diameter is perceived as undesirable for nonlinear applications. Despite a lower effective nonlinearity associated with a larger core of conventional multimode fibers, the multimode nature of these fibers can play an important role in some nonlinear applications. In particular, the presence of multiple propagating modes with different dispersive properties results in expanded phase-matching opportunities for the generation of four-wave mixing (FWM) signals in optical fibers [5–7]. The GIMF used in our experiments has two desirable properties that make it particularly suitable for SRS generation. First, since the effective modal area of each mode in the GIMF scales only as square root of the core area, the effective nonlinearity of some propagating modes is comparable with conventional single-mode fibers [8]. Second, a relatively high GeO₂ content in the core of the standard telecommunication GIMF used in our experiments results in a higher peak Raman gain coefficient compared with silica-core fibers [9].

2. Generation of new wavelengths and spectral measurements

The pump used in our experiment is a frequency-doubled, Q-switched, Nd:YLF laser operating at 523 nm wavelength, and its 8-ns duration pulses are coupled to the input tip of the fiber using a microscope objective. The laser beam is not diffraction-limited, and many modes in the fiber are excited simultaneously. The GIMF is a 1-km long standard, 50/125- μ m, bare fiber (Corning ClearCurve OM2). The output spectrum is measured using a CCS200 spectrometer (from Thorlabs) operating in the range of 200–1000 nm and a MS9740A OSA (from Anritsu) covering the 600–1750 nm wavelength range. We measured the energy of input pulses required for reaching the Raman threshold immediately after coupling into the fiber (less than 1-meter of propagation inside the GIMF) to be 20.9 μ J; we estimate the peak power to be about 2.5 kW. The pulse energy decreased to about 0.515 μ J after 1-km of propagation, which is consistent with the expected attenuation of about 16 dB/km at the pump wavelength.

The sequential generation of cascaded Raman peaks at four different pump power levels is

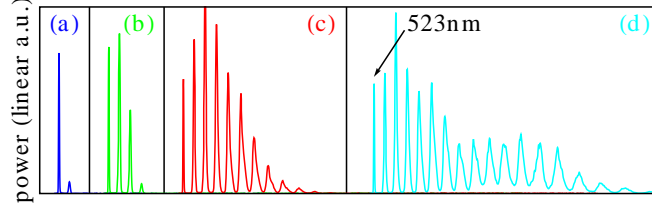


Fig. 1. Sequential generation of Raman peaks at four pump power levels as measured by the spectrometer. The vertical axis is in arbitrary “linear” unit of power. Labels are omitted on the horizontal wavelength axis for clarity. The leftmost peak in each subplot is at 523 nm.

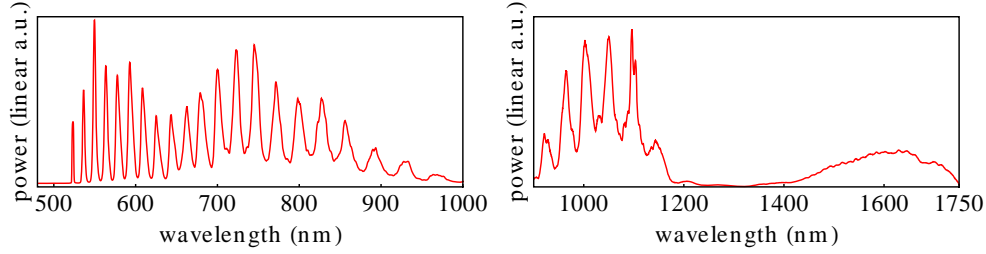


Fig. 2. (left) Cascaded Raman peaks measured with the spectrometer. (right) Spectrum measured by the OSA when pump power is increased to just below the burning threshold of fiber's tip; the spectral dip at around 1300 nm and the broad peak beyond 1400 nm are two notable features in this infrared range.

shown in four separate subplots in Fig. 1 using spectrometer measurements. The pump power just exceeds the Raman threshold in subplot (a) showing the pump at 523 nm and the first low-power Stokes line. As the pump power is increased, the first Stokes line extracts power from the pump until it becomes strong enough to seed the generation of next Stokes line. This process continues and more and more Raman peaks are generated with increasing pump power, as shown in subplots (b), (c), and (d) in Fig. 1. The 20 cascaded peaks shown in Fig. 2 (left) extend from 523 nm to just above 1000 nm in wavelength. The estimated input peak power of our pulses is 22 kW for this figure.

As the pump power is further increased, even more cascaded Raman peaks appear beyond the 1000 nm wavelength range of our spectrometer. Figure 2 (right) shows the spectrum measured with the Anritsu OSA in the range of 900–1750 nm at the maximum pump power level (just below the burning threshold of fiber's input tip). The spectral dip at around 1300 nm and the broad peak beyond 1400 nm are two notable features in this infrared range. In our opinion, the broad peak centered at 1600 nm results from the onset of modulation instability in the presence of anomalous dispersion. The resulting short pulses can undergo soliton fission and experience Raman-induced spectral shifts as well as soliton-collision-based spectral broadening, resulting in a broad supercontinuum like feature [10]. We stress that the two plots in Fig. 2 should not be compared directly since they correspond to different power levels and employ different vertical scales.

The spectral dip centered at the 1320-nm wavelength is surprising at first sight. We think its appearance is related to a reduction in the SRS gain occurring near the zero-dispersion-wavelength of the fiber, where the SRS gain is suppressed due to a near-perfect phase-matching of the FWM process [10]. The dip at 1320 nm can be seen more clearly in Fig. 3, where we plot the data in Fig. 2 (right) on a logarithmic power scale.

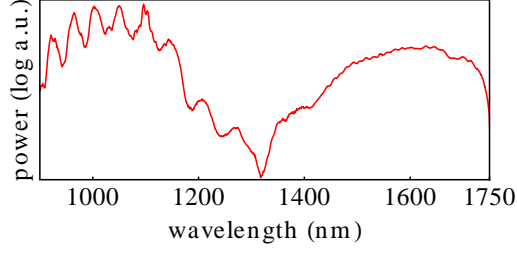


Fig. 3. Same as Fig. 2 (right) but data plotted using a logarithmic vertical scale. The input pump power is just below the burning threshold of fiber's tip.

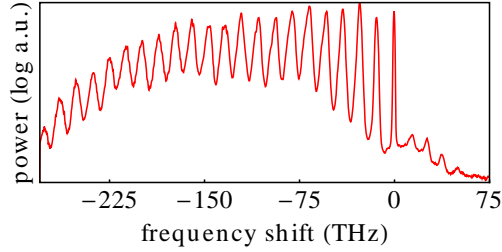


Fig. 4. Raman comb measured with the spectrometer and plotted using frequency shift on the horizontal axis. Notice the presence of FWM peaks on the anti-Stokes side.

We note that the presence of efficient FWM phase-matching opportunities in the GIMF impacts the generation of the cascaded Raman peaks [8]. Figure 4 shows the spectrometer data in the frequency domain, by plotting on the horizontal axis the frequency shift of the Raman comb relative to the pump frequency, and power on a logarithmic scale on the vertical axis. Equal spacing of various peaks on the Stokes side is expected for a cascaded Raman process. However, the presence of FWM frequencies on the anti-Stokes side of the pump is the most notable feature in this figure. The phase-matched frequency counterparts of these FWM idlers on the Stokes side can affect the location and amplitude of the cascaded Raman peaks. We observed that the strength of the FWM signal depended on launch conditions, and FWM was absent (or highly suppressed) in some of our measurements.

In order to explore this effect, we slightly offset the input pump beam so that beam center is not aligned with the center of the fiber core. The pump now excites the GIMF modes with different power ratios, resulting in efficient FWM in a different set of phase-matched wavelengths. The result is a shift in the position of the spectral combs. The red and green spectra in Fig. 5 are measured before and after offsetting the pump laser, respectively. The shift seems to be seeded around the third cascaded Raman peak, separated by about 50 THz from the pump frequency, which is also consistent with the location of a FWM peak in Fig. 4. Similar observations of the effect of the FWM processes on shifting the SRS spectrum have been reported by Sharma et al. [11]; they have shown that the cascaded Raman peaks can shift depending on which modes are excited by the pump laser.

3. Spatial beam profiles and beam cleanup in SRS generation

We also measured the transverse intensity profile of the output beam by a CCD camera using several bandpass color filters with a bandwidth of about 10 nm (full width at half-maximum). The results are shown in Fig. 6. The leftmost profile is measured without a color filter, and

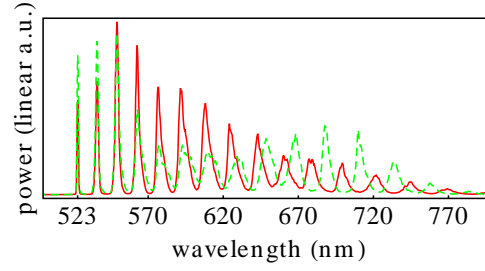


Fig. 5. SRS spectra measured before (red solid line) and after (dashed green line) a slight offset of the pump beam from the fiber center. Shift of Raman peaks is caused by different FWM conditions caused by excitation of different fiber modes.

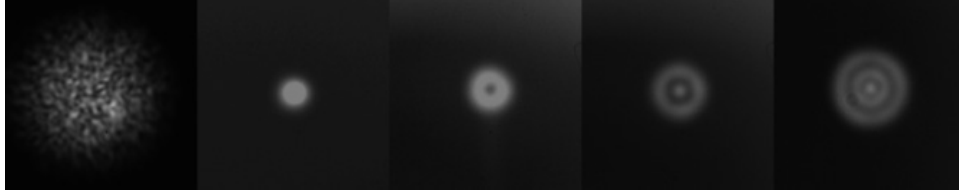


Fig. 6. Measured spatial profiles using a CCD-based beam profiler. The leftmost image is measured with no filters. The other 4 images are obtained using color filters centered at 610 nm (second from left), 700 nm (third from left), 770 nm (fourth from left), and 890 nm (rightmost).

the interference of multiple modes can be clearly observed as a speckle pattern. When a color filter centered at 610 nm is placed in front of the beam (second from left), we observe a narrow round spot that appears to correspond to the spatial profile of the fundamental LG_{00} mode of our GIMF (LG stands for Laguerre-Gauss). A donut-shape spot (third from left) is observed when a color filter centered at 700 nm is placed in front of the beam; it may correspond to the LG_{01} mode of our fiber.

Spatial beam profiles corresponding to higher-order fiber modes were also seen in our experiment. As two examples, the two rightmost images of Fig. 6 show profiles corresponding to the LG_{10} and LG_{20} modes. They were obtained by using optical filters with a 10-nm pass-band centered at 770 nm and 890 nm wavelengths, respectively. The most notable feature we want to stress is that a GIMF can be used as a device that not only shifts the pump wavelength toward the red side through SRS but also performs the beam cleanup owing to the fact that different-order Raman peaks generally propagate in different modes of the fiber. An explanation of SRS-induced beam cleanup in graded-index multimode optical fibers can be found in Ref. [12]. Chiang reported similar results for higher order SRS combs in a 30-m-long fiber [13]. However, only LP_{01} mode (corresponding to LG_{00} mode here) was observed for a 1-km-long fiber. In our experiments, we observed higher-order modes even for a 1-km-long fiber, and beam cleanup was not at the same level reported in Ref. [13].

4. Conclusion

We have used a standard, telecommunication-grade, graded-index multimode fiber for SRS generation by pumping it at 523 nm with 8-ns pulses. We observe multiple cascaded Raman peaks extending up to 1300 nm. Beyond that wavelength, the nature of dispersion changes from normal to anomalous since our fiber has its zero-dispersion wavelength near 1320 nm. At

higher pump powers, in addition to the multiple cascaded Raman peaks, we observe a single broadband spectral peak, extending from 1350 to 1750 nm. Its origin appears to be related to the formation of solitons through modulation instability and their subsequent fission induced by higher-order dispersion and intrapulse raman scattering. Such features have been observed in the past for single-mode fibers. Our experiments show that a supercontinuum can also form in a multimode fiber. The multimode nature of the fiber can also be useful from a practical standpoint. For example, we observed that different spectral peaks have spatial patterns that correspond to different fiber modes. This feature can be useful for beam cleanup. Future efforts will focus on extending the spectrum to the infrared region and on stabilizing the frequency and power of individual comb lines for practical applications.

Acknowledgments

A. Mafi acknowledges support from the UWM Research Growth Initiative grant and the Air Force Office of Scientific Research under Grant FA9550-12-1-0329.

Nonlinear switching in a two-concentric-core chalcogenide glass optical fiber for passively mode-locking a fiber laser

Elham Nazemosadat and Arash Mafi*

Department of Electrical Engineering and Computer Science, University of Wisconsin-Milwaukee, Milwaukee, Wisconsin 53211, USA

*Corresponding author: mafi@uwm.edu

Received June 2, 2014; revised July 1, 2014; accepted July 4, 2014;
posted July 9, 2014 (Doc. ID 213192); published August 5, 2014

We propose an all-fiber mode-locking device, which operates based on nonlinear switching in a novel two-concentric-core fiber structure. The design is particularly attractive given the ease of fabrication and coupling to other components in a mode-locked fiber laser cavity. The nonlinear switching in this coupler is studied, and the relative power transmission is obtained. The analysis shows that this nonlinear switch is practical for mode-locking fiber lasers and is forgiving to fabrication errors. © 2014 Optical Society of America

OCIS codes: (230.4320) Nonlinear optical devices; (140.4050) Mode-locked lasers; (060.3510) Lasers, fiber.
<http://dx.doi.org/10.1364/OL.39.004675>

A nonlinear optical device, referred to as a saturable absorber (SA), is required to start the lasing process in passively mode-locked lasers. The power-dependent transmission of SAs creates an intensity contrast in the laser cavity, which leads to the suppression of random fluctuations and the generation of optical pulse trains. Common fiber-integrable SAs have deficiencies such as long-term reliability, thermal issues, and sensitivity to environmental perturbations, which limit their usefulness for mode-locked fiber laser applications. Also, common SAs have become a limiting factor in boosting the pulse energy and peak power of mode-locked lasers to higher values. Hence, there is a strong need to develop robust alternative mode-locking techniques.

Recently, nonlinear mode coupling in waveguide arrays and multicore fibers [1–5] and also nonlinear multimodal interference in graded-index multimode fibers [6] have been introduced as alternative techniques that address most of the limitations faced by common SAs. In Ref. [7], we compared the nonlinear switching behavior in multicore versus multimode fibers and showed that a much higher switching power is required in the latter case, due to the large difference in the propagation constant of the modes. This feature makes multimode fiber couplers potential mode-locking devices for future high-peak-power lasers. For lower peak powers, as is the case in most present-day mode-locked fiber lasers, it is preferred to use multicore couplers.

Our recent study on multicore fiber array couplers showed that going from a two-core fiber geometry to a higher number of cores does not improve the nonlinear switching performance of the device considerably, if any at all [8]. Hence, according to our studies, a two-core fiber coupler with optimized parameters is the optimum solution to achieve an all-fiber mode-locking device.

In this Letter, we propose a novel all-fiber nonlinear switching and mode-locking device in the form of a triple-clad fiber, as shown in Fig. 1, where the refractive index of the core and that of the second cladding layer are the same. We will refer to this structure as a two-concentric-core (TCC) fiber, which is composed of a

central circular core and a surrounding ring core [9,10]. The main reason for choosing this geometry is its simple fabrication process. Given that conventional fibers are fabricated radially, maintaining the sensitive specifications of this fiber during the drawing process is easier than with nonconcentric conventional two-core fibers [11]. Another related reason is that aligning the central core of this fiber with the single-mode fibers (SMFs) in the laser cavity is much easier and more robust compared with conventional two-core geometries.

In this Letter, the parameters of this two-core-fiber mode-locking device are designed, and the nonlinear propagation of a pulse in this coupler is analyzed numerically. To lower the required switching power, it would be preferred to build the coupler from a material with a higher nonlinearity compared to silica [12]. Chalcogenide glass is a suitable candidate, because it has a nonlinear coefficient up to 1000 times larger than silica [13].

The all-fiber mode-locking device is shown in Fig. 2, where the beam is injected into the central core of the

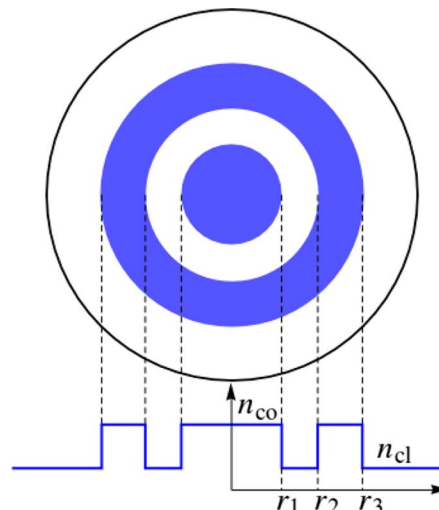


Fig. 1. Cross-sectional view and the refractive index profile of the fiber.

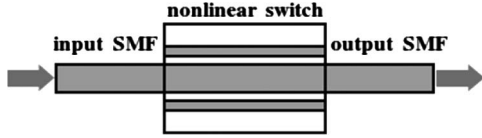


Fig. 2. All-fiber nonlinear switching device composed of a TCC coupler placed in between two SMFs.

TCC fiber coupler using an input SMF and is collected at the output from another SMF. The injected beam from the input SMF is in the form of an azimuthal symmetric nearly Gaussian beam, so by centrally aligning the core of the input SMF with the central core of the TCC coupler, only zero-angular-momentum modes will be excited in the coupler [14]. For low-input optical powers launched into the nonlinear coupler, optical power is periodically exchanged among the two cores because of their modal overlap. To achieve maximum linear coupling, the parameters of the fiber coupler should be designed such that the two cores are phase matched [15]. For high-input optical powers, nonlinear effects arise and alter the refractive index of each waveguide. This will detune the effective propagation constants of the modes and will consequently reduce the power exchange efficiency between the cores, which means that light will be mainly preserved in the launch core [16]. Hence, if an optical pulse is transmitted through a fiber coupler with a length equal to the coupler's half-beat length, its low-intensity tails will be linearly coupled to the adjacent core, while its high-intensity center peak will remain in the launch core [17]. If only the light in the launch core is collected at the output, the required power-dependent transmission for mode-locking is obtained [1,2].

The fiber profile is designed such that it supports only two zero-angular-momentum guided modes, referred to as the first- and second-order guided modes. The electric field in the TCC can be expressed as the summation of these guided modes as

$$E(x, y, z, t) = \sum_{\mu=1,2} A_{\mu}(z, t) F_{\mu}(x, y) e^{i(\omega_0 t - \beta_{0,\mu} z)}, \quad (1)$$

where $A_{\mu}(z, t)$ is the slowly varying envelope of the electric field of the μ th mode with the normalized spatial distribution $F_{\mu}(x, y)$ and propagation constant $\beta_{0,\mu}$. The generalized nonlinear Schrödinger equation (GNLSE) describing the longitudinal evolution of the pulse in this fiber coupler can be written as [18,19]

$$\begin{aligned} \frac{\partial A_{\mu}}{\partial z} = & -\frac{\alpha}{2} A_{\mu} + i\delta\beta_{0,\mu} A_{\mu} - \delta\beta_{1,\mu} \frac{\partial A_{\mu}}{\partial t} - i\frac{\beta_{2,\mu}}{2} \frac{\partial^2 A_{\mu}}{\partial t^2} \\ & + i\left(\frac{n_2\omega_0}{c}\right) \sum_{\nu,\kappa,\rho=1,2} f_{\mu\nu\kappa\rho} A_{\nu} A_{\kappa} A_{\rho}^*, \mu = 1, 2. \end{aligned} \quad (2)$$

The indices can take the value of 1 or 2, corresponding to first- and second-order modes. α is the fiber attenuation, $\beta_{1,\mu}$ is the group delay per unit length, and $\beta_{2,\mu}$ is the group velocity dispersion (GVD) parameter of the μ th mode. We define $\delta\beta_{0,1} = -\delta\beta_{0,2} = \beta_{0,1} - \beta_{0,\text{ref}}$ and $\delta\beta_{1,1} = -\delta\beta_{1,2} = \beta_{1,1} - \beta_{1,\text{ref}}$, where $\beta_{i,\text{ref}} = (\beta_{i,1} + \beta_{i,2})/2$ for $i = 0, 1$. n_2 is the nonlinear index coefficient, and

ω_0 is the carrier frequency. The nonlinear coupling coefficients are given by

$$f_{\mu\nu\kappa\rho} = \iint dx dy F_{\mu}^* F_{\nu} F_{\kappa} F_{\rho}^*, \quad (3)$$

where the mutually orthogonal spatial profiles are assumed to be normalized according to $\iint F_1^2 dx dy = \iint F_2^2 dx dy = 1$. The spatial mode profiles of the guided modes of the TCC coupler, F_1 and F_2 , and also that of the center core, F_c , can be found using the finite element method (FEM) [20], where F_c is calculated for the central core in the absence of the outer ring. The beam is launched into and collected from the center core of the TCC fiber coupler. The transmittance is defined as the energy at the output of the center core divided by the total energy injected into the coupler, given by

$$\tau = \frac{\int_{-\infty}^{+\infty} |A_c(L_c, t)|^2 dt}{\int_{-\infty}^{+\infty} (|A_1(0, t)|^2 + |A_2(0, t)|^2) dt}, \quad (4)$$

where L_c is the half-beat length, $P_{\text{out}} = |A_c|^2$ is the collected output power from the coupler, and A_c is the field amplitude of the center core, defined as

$$A_c(z, t) = A_1(z, t) \iint F_c^* F_1 dx dy + A_2(z, t) \iint F_c^* F_2 dx dy. \quad (5)$$

In the following simulations, we have assumed that the fiber material is As_2Se_3 chalcogenide glass. The operating wavelength is considered $\lambda_0 = 1550$ nm. The refractive index of both cores is $n_{\text{co}} = 2.834$, while that of the cladding is $n_{\text{cl}} = 2.831$. The central core has a radius of $r_1 = 4.1$ μm , and the inner radius of the ring is $r_2 = 8.2$ μm , while its width is 3.94 μm . The nonlinear index is $n_2 = 1.1 \times 10^{-17}$ m^2/W , and the fiber propagation loss is $\alpha = 1$ dB/m [13,21]. The dispersion of the fundamental mode is equal to $D = -826$ ps/nm/km, while that of the second-order mode is $D = -819$ ps/nm/km. These values include both the material and the waveguide dispersion. The material dispersion is calculated using the Sellmeier equation [22] and then incorporated in the FEM to evaluate the total chromatic dispersion. The fiber exhibits normal dispersion at 1550 nm. It should be noted that fibers with such a layered refractive index profile are frequently used for dispersion compensation due to their large negative dispersion values [23].

With these parameters, each individual core supports only 1 zero-angular-momentum mode. It should be pointed out that in order to minimize the splicing losses between the silica SMF-28 fibers of the cavity and the TCC, the dimensions and numerical aperture of the central core are chosen to be similar to those of the cavity SMFs. The Fresnel reflection loss, due to the refractive index difference between silica and chalcogenide glass, is around 0.45 dB on each end of the TCC fiber, which can be potentially suppressed by using antireflection coating [24]. Whether the facet reflection can be tolerated or would require impedance matching depends on the configuration of the mode-locked fiber laser cavity, and is beyond the scope of this analysis. The main

advantage of this to silica-based structures, as will be shown later, is its substantially lower switching power. In what follows, we will refer to the power after reflection and coupling losses at the input end as the input power, and the power before reflection and coupling losses at the output end as the output power. The length of the TCC coupler is 1.74 mm, given by $L_c = \pi/(2C)$, where $C = \delta\beta_{0,1}$ is the linear coupling coefficient among the two propagating modes [15].

We assume that a hyperbolic secant optical pulse in the form of $E(0, t) = P_0^{1/2} \text{sech}(t/t_0)$ is launched into the nonlinear coupler through the input SMF, where P_0 is the peak power, and the full width at half-maximum (FWHM) pulse duration is $T_0 \approx 1.763t_0$. The nearly Gaussian spatial mode profile of the input beam with a temporal power profile of $P_c(t)$ excites the guided modes of the TCC fiber with power profiles $P_1(t)$ and $P_2(t)$ with normalized peak powers p_1 and p_2 , respectively, where it can be shown that $p_1 + p_2 \approx 1$. The normalized peak excitation power of each guided mode at the TCC input facet is calculated using the overlap integral of the input beam and that particular mode, where in this case it is found that $p_1 = 62.6\%$ and $p_2 = 37.2\%$.

We have applied a split-step Fourier method [25] to solve Eq. (2) and analyze the propagation of the pulse inside the nonlinear coupler. For low powers, the TCC fiber operates similarly to a linear directional coupler at half-beat length, and most of the pulse energy is transferred to the ring core. For intense pulses, the central portion of the pulse remains in the central waveguide, while the low-intensity wings of the pulse are transferred to the ring core. In Fig. 3, the normalized input pulse power launched into the central core and that of the output pulse are shown for a FWHM pulse duration of $T_0 = 1$ ns. The reason for choosing a nanosecond pulse width is that in most modern lasers the SA is a critical device only for allowing the pulse to build up from the noise and start the lasing process, while a narrow spectral filter is responsible for the pulse shaping [26]. Hence, nanosecond pulses which are pertinent to the starting process are considered here.

The effect of the pulse duration on the switching dynamics can be seen in Fig. 4, where we have calculated the relative power transmission as a function of the input

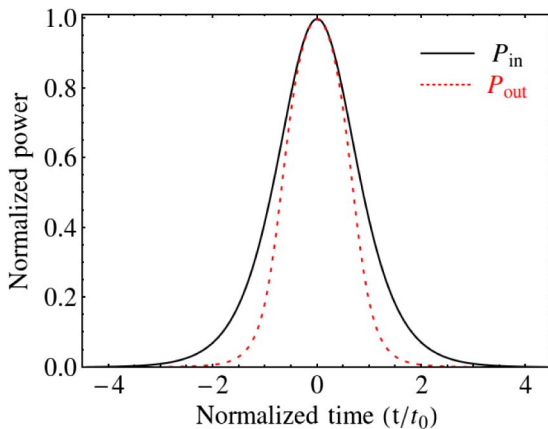


Fig. 3. Normalized input and output pulse shapes for a pulse width of $T_0 = 1.763t_0 = 1$ ns. The input peak power is 5 kW.

peak power for various input pulse durations. The relative power transmission for pulse widths larger than 1 ps are the same as that of $T_0 = 1$ ps. It can be observed that a higher input power is required to switch the output from τ_{\min} to τ_{\max} as the duration of the pulse gets shorter. Also, the maximum achievable transmission decreases as the pulse duration is shortened. The reason is that the dispersion effects become more significant for shorter pulse widths, and the resultant pulse broadening prevents complete power transfer. It should be noted that, as the input peak power is increased, nonlinear terms become larger, and because of the large amount of the induced frequency chirp imposed on the pulse due to self-phase modulation, even weak dispersive effects lead to significant pulse shaping. Hence, for high input powers, the output pulse would become rectangularly shaped with relatively sharp leading and trailing edges [25]. This limits the upper level of the input peak power to these couplers. The damage threshold of chalcogenide glasses should also be considered while designing these couplers. The optical damage mechanisms for these fibers are not well known; however, the obtained switching power in our design is not far from the damage threshold of another chalcogenide glass composition, As_2S_3 [27,28].

The switching power is considered to be the power at which the output from the central core contains 50% of the input energy injected into the fiber. While this power is slightly above 3 kW for the chalcogenide fiber coupler considered here, it is of the order of MWs for silica fibers with the same structure [29]. Also, one can reduce the switching power by increasing the distance between the two cores and reducing the coupling between them. For example, increasing the gap between the two cores to 9 μm results in a switching power of 800 W. However, the length of the coupler is longer in this case, and the strong dispersive effects overcome the nonlinear pulse shortening mechanism if the pulse is too short.

During the fabrication process, random core diameter fluctuations will be inevitable; the effect of these fabrication imperfections on the performance of the coupler is studied in Ref. [29], and it is shown that these imperfections are tolerable as long as the changes they impose on the propagation constant of the modes are smaller than the coupling between the two cores. For the parameters

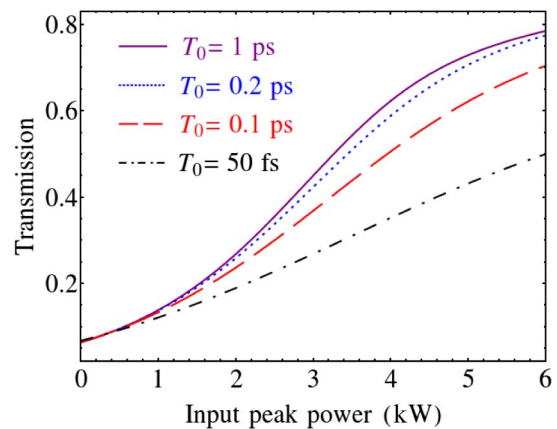


Fig. 4. Relative power transmission is plotted as a function of the input peak power for different pulse widths.

considered here, typical $\pm 2\%$ core size variations are tolerable.

In summary, we have proposed a novel concentric-core fiber structure made of chalcogenide glass to be used as an all-fiber mode-locking element. The nonlinear switching behavior of this coupler is analyzed by carrying out a normal mode analysis of the waveguide. The chalcogenide glass has a large chromatic dispersion. In order to avoid substantial pulse broadening due to dispersion, the length of the coupler (half-beat length) should be reduced as much as possible. This, in turn, can be achieved by reducing the separation between the central core and the ring core and increasing the coupling between them. On the other hand, increasing the coupling between the cores increases the switching power, which may not be desirable. Therefore, the optimal design is a compromise between the pulse broadening and switching power. The pulse broadening and switching power can also be modified by changing the geometrical parameters and glass compositions.

The authors acknowledge support from the Air Force Office of Scientific Research under Grant No. FA9550-12-1-0329 and are indebted to the anonymous reviewers for their detailed and helpful comments.

References

1. H. G. Winful and D. T. Walton, *Opt. Lett.* **17**, 1688 (1992).
2. J. L. Proctor and J. N. Kutz, *Opt. Lett.* **30**, 2013 (2005).
3. D. D. Hudson, K. Shish, T. R. Schibli, J. N. Kutz, D. N. Christodoulides, R. Morandotti, and S. T. Cundiff, *Opt. Lett.* **33**, 1440 (2008).
4. Q. Chao, D. D. Hudson, J. N. Kutz, and S. T. Cundiff, *IEEE Photon. J.* **4**, 1438 (2012).
5. T. F. S. Büttner, D. D. Hudson, E. C. Mägi, A. C. Bedoya, T. Taunay, and B. J. Eggleton, *Opt. Lett.* **37**, 2469 (2012).
6. E. Nazemosadat and A. Mafi, *J. Opt. Soc. Am. B* **30**, 1357 (2013).
7. E. Nazemosadat and A. Mafi, *Opt. Express* **21**, 30739 (2013).
8. E. Nazemosadat and A. Mafi, *J. Opt. Soc. Am. B* **30**, 2787 (2013).
9. J.-L. Auguste, R. Jindal, J.-M. Blondy, M. Clapeau, J. Marcou, B. Dussardier, G. Monnom, D. B. Ostrowsky, B. P. Pal, and K. Thyagarajan, *Electron. Lett.* **36**, 1689 (2000).
10. F. Gérôme, J.-L. Auguste, J. Maury, J.-M. Blondy, and J. Marcou, *J. Lightwave Technol.* **24**, 442 (2006).
11. J. R. Cozens and A. C. Boucouvalas, *Electron. Lett.* **18**, 138 (1982).
12. A. Zakery and M. Hatami, *J. Phys. D* **40**, 1010 (2007).
13. G. Lenz, J. Zimmermann, T. Katsufuji, M. E. Lines, H. Y. Hwang, S. Spälter, R. E. Slusher, S.-W. Cheong, J. S. Sanghera, and I. D. Aggarwal, *Opt. Lett.* **25**, 254 (2000).
14. A. Mafi, P. Hofmann, C. Salvin, and A. Schülzgen, *Opt. Lett.* **36**, 3596 (2011).
15. B. E. A. Saleh and M. C. Teich, *Fundamentals of Photonics*, 2nd ed. (Wiley, 2007).
16. S. M. Jensen, *IEEE J. Quantum Electron.* **18**, 1580 (1982).
17. S. R. Friberg, A. M. Weiner, Y. Silberberg, B. G. Sfez, and P. S. Smith, *Opt. Lett.* **13**, 904 (1988).
18. F. Poletti and P. Horak, *J. Opt. Soc. Am. B* **25**, 1645 (2008).
19. A. Mafi, *J. Lightwave Technol.* **30**, 2803 (2012).
20. T. A. Lenahan, *Bell Syst. Tech. J.* **62**, 2663 (1983).
21. L. Fu, M. Rochette, V. Ta'eed, D. Moss, and B. Eggleton, *Opt. Express* **13**, 7637 (2005).
22. "Specification sheet for product AMTIR-2" (Amorphous Materials Inc., 2009). <http://www.amorphousmaterials.com>.
23. K. Thyagarajan, R. K. Varshney, P. Palai, A. K. Ghatak, and I. C. Goyal, *IEEE Photon. Technol. Lett.* **8**, 1510 (1996).
24. K. Abedin, *Opt. Express* **13**, 10266 (2005).
25. G. P. Agrawal, *Nonlinear Fiber Optics*, 5th ed. (Elsevier, 2013).
26. A. Chong, J. Buckley, W. Renninger, and F. Wise, *Opt. Express* **14**, 10095 (2006).
27. O. P. Kulkarni, C. Xia, D. J. Lee, M. Kumar, A. Kuditcher, M. N. Islam, F. L. Terry, Jr., M. J. Freeman, B. G. Aitken, S. C. Currie, J. E. McCarthy, M. L. Powley, and D. A. Nolan, *Opt. Express* **14**, 7924 (2006).
28. V. G. Taeed, N. J. Baker, L. Fu, K. Finsterbusch, M. R. E. Lamont, D. J. Moss, H. C. Nguyen, B. J. Eggleton, D. Y. Choi, S. Madden, and B. Luther-Davies, *Opt. Express* **15**, 9205 (2007).
29. E. Nazemosadat and A. Mafi, "Design considerations for multi-core optical fibers in nonlinear switching and mode-locking applications," arXiv:1405.1368 (2014).

Design considerations for multicore optical fibers in nonlinear switching and mode-locking applications

Elham Nazemosadat* and Arash Mafi

Department of Electrical Engineering and Computer Science, University of Wisconsin-Milwaukee, Milwaukee, Wisconsin 53211, USA

*Corresponding author: nazemosa@uwm.edu

Received May 7, 2014; revised June 13, 2014; accepted June 13, 2014;
posted June 19, 2014 (Doc. ID 211544); published July 18, 2014

We explore the practical challenges that should be addressed when designing a multicore fiber coupler for nonlinear switching or mode-locking applications. The inevitable geometric imperfections formed in these fiber couplers during the fabrication process affect the performance characteristics of the nonlinear switching device. Fabrication uncertainties are tolerable as long as the changes they impose on the propagation constant of the modes are smaller than the linear coupling between the cores. It is possible to reduce the effect of the propagation constant variations by bringing the cores closer to each other, thereby increasing the coupling. However, higher coupling translates into a higher switching power, which may not be desirable in some practical situations. Therefore, fabrication errors limit the minimum achievable switching power in nonlinear couplers. © 2014 Optical Society of America

OCIS codes: (230.4320) Nonlinear optical devices; (140.4050) Mode-locked lasers; (080.1238) Array waveguide devices.

<http://dx.doi.org/10.1364/JOSAB.31.001874>

1. INTRODUCTION

Nonlinear mode coupling in multicore fiber couplers has recently attracted considerable attention owing to their applications in nonlinear switching, and in particular, in all-optical mode locking of fiber lasers [1–6]. A multicore fiber operates as a linear directional coupler at low optical powers, where power is exchanged periodically among neighboring waveguides. Linear coupling is most efficient when the cores are phase matched, or in other words, their propagating modes have identical propagation constants [7]. At higher optical powers, the nonlinear refractive indices of the cores are altered due to nonlinear effects. Consequently, the effective propagation constants of the participating modes are detuned, which reduces the power exchange efficiency between the neighboring cores and as a result, the majority of light remains in the launch core [8]. Therefore, the different behaviors that a multicore fiber shows based on the intensity of the input optical power make it a suitable device for nonlinear switching and mode-locking applications.

Nonlinear switching and mode-locking schemes, which rely on nonlinear coupling among the propagating modes, deal with practical constraints. For instance, the need for a high nonlinear index of refraction limits the application of long-period fiber gratings in nonlinear switching [9]. In dual-core fiber ring lasers, preserving strong resonant coupling between the core modes over the required cavity lengths is difficult [10]; similarly, maintaining the coupling among the modes of a graded-index multimode fiber over long lengths is a challenge [11]. In multicore fiber couplers, uncertainties such as fluctuations in the core radii happen both in the preform fabrication and the drawing of the fiber. These errors affect the core-to-core couplings. In some applications, such as image transport, errors and variations are incorporated intentionally

in the cores to enhance the image contrast, because efficient core-to-core coupling can be detrimental to the image transport quality [12,13]. By contrast, applications such as nonlinear switching require accurate core-to-core coupling, so, fabrication errors degrade the performance of multicore nonlinear fiber couplers.

In this paper, to get a realistic understanding of the performance of multicore fiber couplers in the presence of fabrication uncertainties, the limitations that these errors impose on the performance of a nonlinear switch are investigated at three levels: (1) effects on the propagation constant of the propagating modes β , relative to the core-to-core coupling; (2) effects on the first derivative of β , otherwise known as the group velocity; and (3) effects on the second derivative of β , known as the group velocity dispersion (GVD). These issues will be addressed in the following sections of the paper.

2. UNCERTAINTIES IN FIBER FABRICATION

In the linear regime, light propagation in each core of a two-core fiber coupler is generally described using the coupled mode theory, and can be written as

$$i\partial_z \begin{pmatrix} A_a \\ A_b \end{pmatrix} = \begin{pmatrix} \beta_0 & C_{ba} \\ C_{ab} & \beta_0 \end{pmatrix} \begin{pmatrix} A_a \\ A_b \end{pmatrix} = \mathbf{B}\mathbf{A}, \quad (1)$$

where A_a and A_b are the amplitudes of the modes in each individual waveguide. It is assumed that the propagating modes in both waveguides have identical propagation constants, β_0 , and coupling coefficients, $C_{ab} = C_{ba}$. Instead of considering the modes of individual waveguides and their couplings, an alternative approach is to study the propagation of the

fundamental modes of the complete index profile of the coupler, known as the symmetric and antisymmetric supermodes. The spatial mode profile of the supermodes, $F_\mu(x, y)$, can be approximated as a superposition of the guided modes of each individual core as [14,15]

$$F_\mu(x, y) \approx \sum_{\mu=1,2} k_\mu \tilde{F}_\mu(x, y), \quad (2)$$

where $\tilde{F}_\mu(x, y)$ is the mode profile of the fundamental guided mode propagating in each core and k_μ is the weight factor of the μ th core. The eigenvectors and eigenvalues of \mathbf{B} provide the weight factors and propagation constants of the supermodes, respectively. The eigenvectors of \mathbf{B} , which are $\begin{pmatrix} 1 \\ 1 \end{pmatrix}$ and $\begin{pmatrix} 1 \\ -1 \end{pmatrix}$, lead to equal excitation of both supermodes at the fiber input. However, if due to fabrication uncertainties the propagation constant of one waveguide changes slightly to $\beta_0 + \delta\beta$, the eigenvectors of \mathbf{B} change as well, and consequently, the input beam is coupled to the symmetric and antisymmetric supermodes unequally. This reduces the power exchange efficiency between the two cores and degrades the nonlinear switching performance of the coupler by lowering the modulation depth of the mode-locking device, as also seen in Ref. [15]. In order to avoid this and observe perfect linear switching for low powers, the fluctuations in β_0 should be much smaller than the coupling between the propagating modes. Hence, we can define $\delta\beta \approx C_{ab}$ as the cutoff for the acceptable range of fabrication errors; in this case, around 70% of the power is in one supermode, whereas the other one carries only 30%.

To present the aforementioned arguments, we explore the nonlinear switching behavior of a two-concentric-core (TCC) fiber geometry. This fiber coupler has TCCs, consisting of a central circular core and a surrounding ring core, as shown in Fig. 1. The refractive index profile of the fiber considered can also be seen in this figure. Owing to its cylindrical

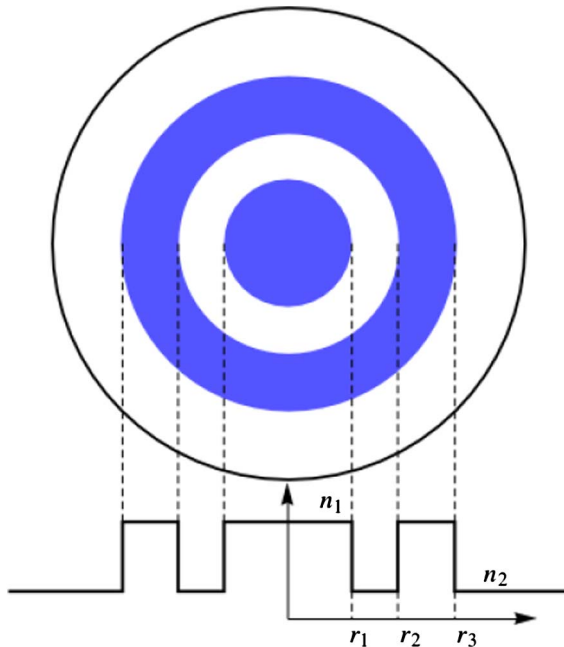


Fig. 1. Cross-sectional view and refractive index profile of the fiber structure.

symmetric configuration, this fiber can be fabricated using the same techniques used for conventional fibers, which is more straightforward compared with nonconcentric two-core fibers. This simple fabrication process is the main reason for choosing this specific geometry. One other reason is that the central core of this fiber can be fabricated with the same material and properties as the single-mode fibers (SMFs) of the laser cavity, easing the alignment of the coupler with the cavity fibers and reducing splicing losses [16].

The fiber profile is designed such that it supports only two zero-angular momentum guided modes, referred to as the first- and second-order guided supermodes. The electric field in the TCC can be expressed as the summation of these guided modes as

$$E(x, y, z, t) = \sum_{\mu=1,2} A_\mu(z, t) F_\mu(x, y) e^{i(\omega_0 t - \beta_{0,\mu} z)}, \quad (3)$$

where $A_\mu(z, t)$ is the slowly varying envelope of the electric field of the μ th mode with the normalized spatial distribution $F_\mu(x, y)$ and propagation constant $\beta_{0,\mu}$. The generalized nonlinear Schrödinger equation describing the longitudinal evolution of a pulse in this fiber coupler can be written as [17,18]

$$\begin{aligned} \frac{\partial A_\mu}{\partial z} = & i\delta\beta_\mu^{(0)} A_\mu - \delta\beta_\mu^{(1)} \frac{\partial A_\mu}{\partial t} - i\frac{\beta_\mu^{(2)}}{2} \frac{\partial^2 A_\mu}{\partial t^2} \\ & + i\left(\frac{n_2\omega_0}{c}\right) \sum_{\nu,\kappa,\rho=1,2} f_{\mu\nu\kappa\rho} A_\nu A_\kappa A_\rho^*, \quad \mu = 1, 2. \end{aligned} \quad (4)$$

The indices can take the value of 1 or 2, corresponding to first- or second-order supermodes, respectively. $\beta_\mu^{(1)}$ denotes the group velocity and $\beta_\mu^{(2)}$ is the GVD parameter of the μ th mode. We define $\delta\beta_1^{(0)} = -\delta\beta_2^{(0)} = \beta_1^{(0)} - \beta_{\text{ref}}^{(0)}$ and $\delta\beta_1^{(1)} = -\delta\beta_2^{(1)} = \beta_1^{(1)} - \beta_{\text{ref}}^{(1)}$, where $\beta_{\text{ref}}^{(i)} = (\beta_1^{(i)} + \beta_2^{(i)})/2$ for $i = 0, 1$. The nonlinear index coefficient of the fiber is defined by n_2 and ω_0 is the carrier frequency. The nonlinear coupling coefficients $f_{\mu\nu\kappa\rho}$ are given by

$$f_{\mu\nu\kappa\rho} = \iint dx dy F_\mu^* F_\nu F_\kappa F_\rho^*, \quad (5)$$

where the mutually orthogonal spatial profiles are assumed to be normalized according to $\iint F_1^2 dx dy = \iint F_2^2 dx dy = 1$.

In the two different TCC fiber couplers studied here, in order to have maximum linear coupling, the inner and outer radii of the ring core are designed such that the propagation constant of its fundamental mode matches that of the central core. The radius of the central core is altered from its original value to the cutoff value, where one supermode carries 70% of the input power, and that value is defined as the maximum acceptable fabrication errors. The core size of the central core is the only geometrical parameter altered in this paper, because it has been shown that the performance of this fiber is more sensitive to variations of the central core radius compared with that of the ring core [19]. The radius of the central core and the refractive index of both cores in coupler A are $r_1 = 2.1 \mu\text{m}$ and $n_1 = 1.465$, respectively, whereas the parameters in coupler B are $r_1 = 4.1 \mu\text{m}$ and $n_1 = 1.451$, respectively. The operating wavelength is $\lambda_0 = 1550 \text{ nm}$ and the cladding refractive index for both couplers is assumed to be 1.444 (corresponding to pure silica). Figure 2 shows how the

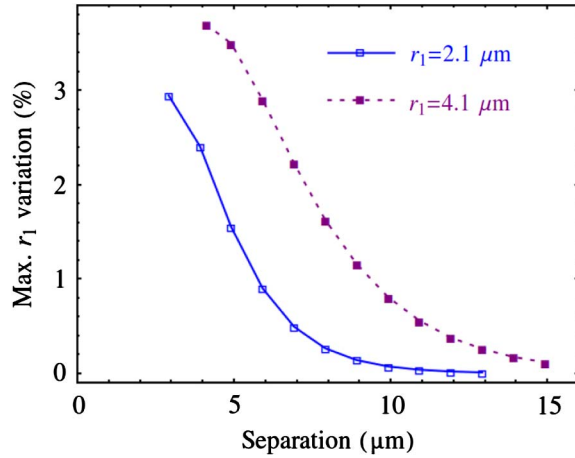


Fig. 2. Maximum acceptable fabrication errors in central core radius as a function of the separation between the cores.

tolerance to fabrication errors in these two couplers varies as a function of the separation between the two cores, where the separation is defined as the gap between the two cores ($r_2 - r_1$ in Fig. 1). As the separation between the ring core and the central core increases, the overlap of the fields reduces, which leads to a smaller coupling and a larger beat length. According to the results, the tolerance to fabrication errors reduces as the ring core is placed farther away from the central core. Hence, it is preferred to design the coupler such that the separation between the two cores is small, at the price of a higher switching power. The switching power is defined as the input power at which the output power from the central and ring core are equal. Typical fabrication errors in core radius are around $\pm 1\%$; thus according to Fig. 2, the maximum allowable separation between the two cores in coupler A is around 6 μm , whereas in coupler B, separations up to 10 μm are acceptable.

3. NONLINEAR SWITCHING BEHAVIOR

The TCC fiber can be used as an all-fiber mode-locking device, referred to as a saturable absorber, as shown in Fig. 3, where the beam is injected into the central core of the TCC coupler using an input SMF and is collected at the output from the same core, using another SMF. To minimize the splicing loss between the cavity and the TCC, the central core is considered identical to the cavity SMFs. Given that the injected beam from the input SMF is in the form of an azimuthal symmetric Gaussian beam, by aligning the central core of the TCC with the input SMF core, only the zero-angular momentum modes of the TCC fiber can be excited [20], which is the case considered in this paper.

When the noise of the gain medium in the laser cavity is transmitted through the TCC fiber coupler with length equal to the coupler's half-beat-length L_{hb} , low-intensity noise is coupled linearly to the ring core and experiences a high loss,

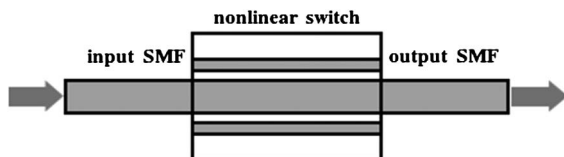


Fig. 3. All-fiber nonlinear switching device composed of a TCC coupler placed between two SMFs.

whereas high-intensity noise remains in the launch core, resulting in a high-intensity contrast. This leads to the formation of optical pulses. The power-dependent transmission feature of the coupler can be used for mode-locking fiber lasers [1,3]. In modern lasers, the saturable absorber is a critical device only for allowing the pulse to build up from noise and start the lasing process, while pulse shaping is achieved through using a narrow spectral filter [21,22]. Therefore, it would be reasonable to study the performance of the device for nanosecond pulses, which are pertinent to the starting process.

A hyperbolic secant optical pulse with a pulse width of t_0 is launched into the nonlinear coupler through the input SMF. The nearly Gaussian spatial mode profile of the input beam excites the supermodes of the coupler. The excitation power related to each supermode can be found using the overlap integral of that particular supermode with the input beam. The pulse propagation inside the nonlinear coupler was analyzed by solving Eq. (4) using the split-step Fourier method. The collected output power from the coupler is $P_{\text{out}} = |A_c|^2$, where A_c is the field amplitude of the central core, obtained by

$$A_c(z, t) = A_1(z, t) \iint F_c^* F_1 dx dy + A_2(z, t) \iint F_c^* F_2 dx dy, \quad (6)$$

where F_1 , F_2 , and F_c are the spatial mode profiles of the two supermodes of the TCC coupler and that of the propagating mode of the central core, respectively. The finite-element method was used to calculate these profiles [23]. F_c is calculated for the coupler in the absence of the outer ring. Transmittance is defined as the energy at the output of the central core divided by the total energy injected into the coupler, given by

$$\tau = \frac{\int_{-\infty}^{+\infty} |A_c(L_{hb}, t)|^2 dt}{\int_{-\infty}^{+\infty} (|A_1(0, t)|^2 + |A_2(0, t)|^2) dt}. \quad (7)$$

In Fig. 4, the normalized input pulse and output pulses corresponding to different peak input pulse intensities are displayed for coupler A. The fiber is assumed to be made of silica and its parameters, with reference to Fig. 1, are $r_1 = 2.1$, $r_2 = 8$, and $r_3 = 9.95$ μm . These parameters are chosen such that the coupler's tolerance to fabrication errors is around $\pm 1\%$, as shown in Fig. 2. It can be observed that as the input power increases, a larger portion of the pulse energy remains in the central waveguide. For the parameters considered here, a switching power of the order of 0.5 MW is required. Transition from low transmission to high transmission occurs when the nonlinear interaction of each mode with itself is comparable to the linear core-to-core coupling; therefore, a fair estimate for obtaining the power threshold for nonlinear switching in an ideal coupler without any fabrication errors is $(n_2 \omega_0 / c) f_{1111} P_0 \approx C$, where $C = \delta \beta_{0,1}$ is the linear coupling coefficient among the two propagating modes. Hence, a lower switching power requires a coupler with a large nonlinear coefficient and a small linear coupling coefficient. In Fig. 5, it can be seen how the linear coupling coefficient, C , varies as a function of the separation between the cores of couplers A and B. To observe better the difference between the C parameter of these two couplers, the figure is plotted on logarithmic scale. As can be observed in the figure, for small separations, the coupling coefficient in coupler A is larger than that in

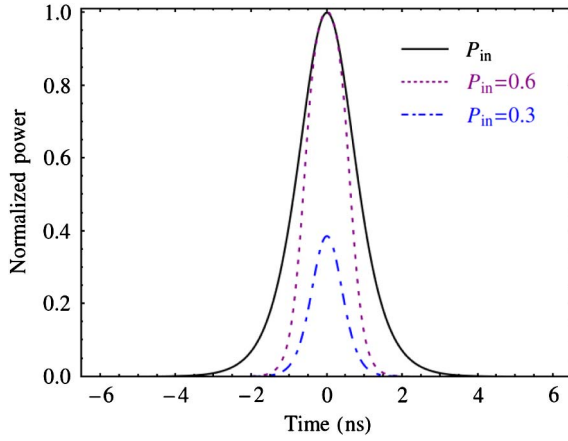


Fig. 4. Normalized pulse power at the output of the central core for different input peak powers (units are MW) when pulse width is $t_0 = 1$ ns. A similar behavior is observed for picosecond pulses, but we considered nanosecond pulses because they are more relevant for the start of a lasing process.

coupler B, whereas vice versa occurs for larger separations. Considering a fixed separation, the effective area of coupler A is less than that of coupler B, resulting in a larger nonlinear coefficient. For the specific couplers considered here, the nonlinear coefficient of coupler A is approximately 3 times that of coupler B for all separations. The combination of linear coupling and nonlinearity leads to a lower switching power in the coupler with the smaller central core radius, for all separation values, as can be seen in Fig. 6. To reduce the switching power, one can increase the separation between the two cores and reduce the coupling. However, as mentioned in the previous section, such a coupler with a large separation between the two cores requires high fabrication precision in order to operate properly in the linear regime.

In Fig. 7, the sensitivity of the coupler transmission has been studied against $\pm 1\%$ variations in the radius of the central core. As observed, the modulation depth of the nonlinear switch is reduced in both cases. When there are no variations in the central core, both supermodes are excited equally, whereas in $\delta_{r_1} = 1\%$, most of the power is carried by the first-order supermode and vice versa for the $\delta_{r_1} = -1\%$ case. This unequal excitation of the modes is the reason behind the lower quality of the transmission curves of these two cases compared with the error-free case. $\delta_{r_1} = 1\%$ variations have

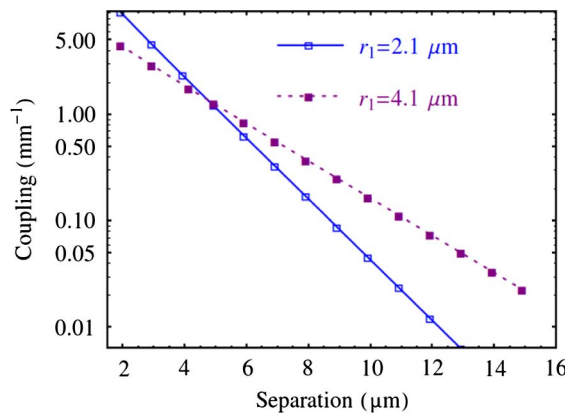


Fig. 5. Coupling among the two cores as a function of the separation between them on logarithmic scale.

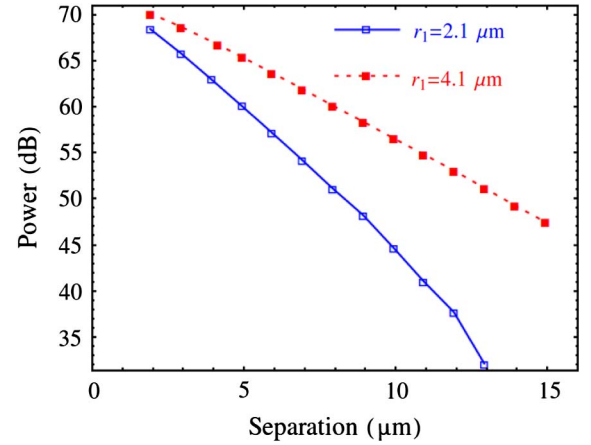


Fig. 6. Approximate power required for nonlinear switching in couplers A and B as a function of the separation between the cores.

the advantage of shifting the transmission curve to lower powers, whereas, $\delta_{r_1} = -1\%$ variations increase the power threshold of the device, which is not desirable. Larger amounts of error reduce the modulation depth further; thus, there is a compromise between the fabrication error and the modulation depth of the device. In cases where a lower modulation depth is sufficient to start the lasing process of the laser, one can deliberately increase the central core radius slightly from the designed value, and hence, reduce the switching power required.

4. GROUP VELOCITY

The two supermodes have different group velocities; thus, the pulses carried by these two modes walk-off due to traveling at different speeds and after a certain propagation distance, known as the walk-off length, given by $L_w = t_0/(\beta_{1,1} - \beta_{1,2})$, the two pulses will not have any overlap and hence, will not interact. Given that the length of the coupler is chosen based on its half-beat-length, L_{hb} , to avoid the walk-off effect, while designing a fiber coupler, one should take note that the minimum pulse width that can propagate through the coupler without experiencing walk-off is $t_0 = L_{hb} \times (\beta_{1,1} - \beta_{1,2})$. For the coupler length considered in this paper, the minimum acceptable pulse width that will not experience walk-off is $t_0 \approx 14.7$ fs.

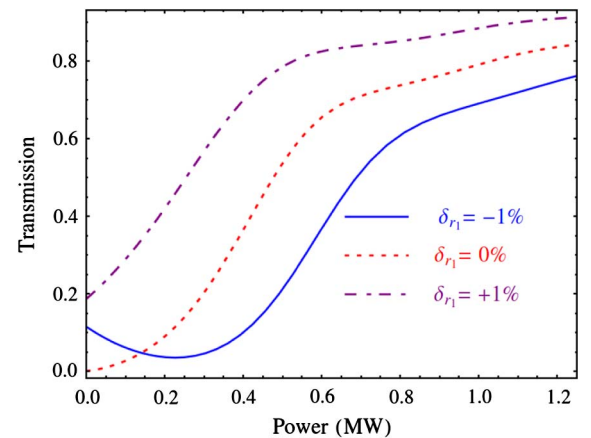


Fig. 7. Relative power transmission of coupler A is plotted as a function of input power with variations in the central core radius.

5. GROUP VELOCITY DISPERSION

When the two cores are coupled strongly and the separation between them is not large, the GVD and also dispersion are comparable to that of SMF-28, and fluctuations due to fabrication imperfections do not affect the dispersion significantly. It is interesting to note that, although for large separations the dispersion in the specific fiber geometry considered here increases rapidly [24], possible fabrication fluctuations reduce the dispersion considerably. Hence, fabrication uncertainties not only are not a limiting factor in terms of the waveguide dispersion but in fact help reduce the dispersion as well. In addition, for the pulse widths considered here, the dispersion length of the fiber is much longer than the coupling length, so even high amounts of dispersion do not affect the coupler's performance considerably.

6. CONCLUSIONS

From a practical point of view, we have studied the design considerations for multicore fiber couplers used in nonlinear switching and mode-locking applications. The effect of fabrication imperfections on the performance of a two-core fiber is investigated, which can be generalized to all multicore couplers. It is observed that there is a compromise between fabrication error and the required nonlinear switching power, and also, the modulation depth of the device.

The geometrical parameters considered in this paper are chosen such that the coupler's tolerance to fabrication errors is around $\pm 1\%$. This limits the maximum separation between the two cores, which in turn increases the switching power. In a more precise fabrication process, the separation between the two cores can be increased and, consequently, the required switching power is reduced. For example, if the separation is increased from its current value of 5.9 to 7.9 μm , the switching power can be reduced by a factor of 3.5 down to 140 kW. To further decrease the switching power, the central core radius can be designed such that it is slightly larger than its optimum value. In this case, in order to achieve the required optical properties, the errors are designed directly into the fiber preform. This lower switching power is achieved at the expense of a lower modulation depth, but this is not much of an issue given that in many cases even a low modulation depth is sufficient to start the lasing process of the laser. It should also be pointed out that to decrease the power threshold, the coupler can be fabricated from material with a higher nonlinearity compared with silica [25].

Given that there are many possible ways to build a mode-locked fiber laser cavity, we did not want to limit ourselves to one particular setup and so we did not discuss any specific laser configurations here. Otherwise, in our recent publication [5], we have shown the possibility of mode locking a laser cavity with multicore optical fibers. Also, a mode-locked fiber laser using a waveguide array has been demonstrated experimentally [4], which serves as a convincing experimental proof of concept for the potential application of nonlinear mode coupling as saturable absorbers.

ACKNOWLEDGMENTS

The authors acknowledge support from the Air Force Office of Scientific Research under Grant FA9550-12-1-0329.

REFERENCES

1. H. G. Winful and D. T. Walton, "Passive mode locking through nonlinear coupling in a dual-core fiber laser," *Opt. Lett.* **17**, 1688–1690 (1992).
2. S. R. Friberg, A. M. Weiner, Y. Silberberg, B. G. Sfez, and P. S. Smith, "Femtosecond switching in a dual-core-fiber nonlinear coupler," *Opt. Lett.* **13**, 904–906 (1988).
3. J. L. Proctor and J. N. Kutz, "Passive mode-locking by use of waveguide arrays," *Opt. Lett.* **30**, 2013–2015 (2005).
4. Q. Chao, D. D. Hudson, J. N. Kutz, and S. T. Cundiff, "Waveguide array fiber laser," *IEEE Photon. J.* **4**, 1438–1442 (2012).
5. E. Nazemosadat and A. Mafi, "Saturable absorption in multicore fiber couplers," *J. Opt. Soc. Am. B* **30**, 2787–2790 (2013).
6. T. F. S. Büttner, D. D. Hudson, E. C. Mägi, A. C. Bedoya, T. Taunay, and B. J. Eggleton, "Multicore, tapered optical fiber for nonlinear pulse reshaping and saturable absorption," *Opt. Lett.* **37**, 2469–2471 (2012).
7. B. E. A. Saleh and M. C. Teich, *Fundamentals of Photonics*, 2nd ed. (Wiley, 2007).
8. S. M. Jensen, "The nonlinear coherent coupler," *IEEE J. Quantum Electron.* **18**, 1580–1583 (1982).
9. A. S. Karar, T. Smy, and A. L. Steele, "Nonlinear dynamics of a passively mode-locked fiber laser containing a long-period fiber grating," *IEEE J. Quantum Electron.* **44**, 254–261 (2008).
10. Y. Oh, S. L. Doty, J. W. Haus, and R. L. Fork, "Robust operation of a dual-core fiber ring laser," *J. Opt. Soc. Am. B* **12**, 2502–2507 (1995).
11. E. Nazemosadat and A. Mafi, "Nonlinear multimodal interference and saturable absorption using a short graded-index multimode optical fiber," *J. Opt. Soc. Am. B* **30**, 1357–1367 (2013).
12. X. Chen, K. L. Reichenbach, and C. Xu, "Experimental and theoretical analysis of core-to-core coupling on fiber bundle imaging," *Opt. Express* **16**, 21598–21607 (2008).
13. S. Karbasi, R. J. Frazier, K. W. Koch, T. Hawkins, J. Ballato, and A. Mafi, "Image transport through a disordered optical fibre mediated by transverse Anderson localization," *Nat. Commun.* **5**, 3362 (2014).
14. A. Mafi and J. V. Moloney, "Shaping modes in multicore photonic crystal fibers," *IEEE Photon. Technol. Lett.* **17**, 348–350 (2005).
15. E. Nazemosadat and A. Mafi, "Nonlinear switching in multicore versus multimode waveguide junctions for mode-locked laser applications," *Opt. Express* **21**, 30739–30745 (2013).
16. J. R. Cozens and A. C. Boucouvalas, "Coaxial optical couplers," *Electron. Lett.* **18**, 138–140 (1982).
17. F. Poletti and P. Horak, "Description of ultrashort pulse propagation in multimode optical fibers," *J. Opt. Soc. Am. B* **25**, 1645–1654 (2008).
18. A. Mafi, "Pulse propagation in a short nonlinear graded-index multimode optical fiber," *J. Lightwave Technol.* **30**, 2803–2811 (2012).
19. F. D. Nunes, H. F. da Silva, and S. C. Zilio, "Design consideration on a dispersion compensating coaxial fiber," *Braz. J. Phys.* **28**, 85–89 (1998).
20. A. Mafi, P. Hofmann, C. Salvin, and A. Schülzgen, "Low-loss coupling between two single-mode optical fibers with different mode-field diameters using a graded-index multimode optical fiber," *Opt. Lett.* **36**, 3596–3598 (2011).
21. A. Chong, J. Buckley, W. Renninger, and F. Wise, "All-normal-dispersion femtosecond fiber laser," *Opt. Express* **14**, 10095–10100 (2006).
22. Y. S. Fedotov, S. M. Kobtsev, R. N. Arif, A. G. Rozhin, C. Mou, and S. K. Turitsyn, "Spectrum-, pulsewidth-, and wavelength-switchable all-fiber mode-locked Yb laser with fiber based birefringent filter," *Opt. Express* **20**, 17797–17805 (2012).
23. T. A. Lenahan, "Calculation of modes in an optical fiber using the finite element method and EISPACK," *Bell Syst. Tech. J.* **62**, 2663–2694 (1983).
24. K. Thyagarajan, R. K. Varshney, P. Palai, A. K. Ghatak, and I. C. Goyal, "A novel design of a dispersion compensating fiber," *IEEE Photon. Technol. Lett.* **8**, 1510–1512 (1996).
25. E. Nazemosadat and A. Mafi, "Nonlinear switching in a concentric ring core chalcogenide glass optical fiber for passively mode-locking a fiber laser," arXiv:1401.7892 (2014).

Preprint: Four-Wave Mixing in a Graded-Index Multimode Optical Fiber

Elham Nazemosadat, *Member, OSA*, Hamed Pourbeyram, *Member, OSA*, and Arash Mafi, *Member, IEEE, Senior Member, OSA*

Abstract—A detailed analysis of four-wave mixing in graded-index multimode fibers is presented. We derive a simplified analytic expression for calculating the phase mismatch occurring as a result of waveguide dispersion among the pump, signal and idler waves in these fibers. According to our analysis, we have found a novel expression that suggests which mode combinations of the participating beams will exhibit identical phase-matching conditions.

I. INTRODUCTION

TO overcome the capacity limitation of nowadays optical communication networks which are based on single mode fibers (SMFs) [1], [2], many researchers are looking into using multimode fibers (MMFs) for transmission in near future networks. The reason is that MMFs can further increase the per-fiber capacity through employing mode division multiplexing. Consequently, there will be a need for suitable signal amplification and wavelength conversion schemes in these type of fibers. Four-wave mixing (FWM) in these fibers is a promising technique to achieve amplification and wavelength conversion [3]–[8].

In this paper, we focus on FWM in graded-index multimode fibers (GIMFs). Unlike conventional MMFs, all guided modes in a GIMF can propagate with nearly identical group velocities at special wavelengths [9]; therefore, nonlinear coupling amongst short pulses is maximally achieved all along the fiber, which adds to the richness of the nonlinear dynamics [10], [11].

The ultrashort pulse propagation in multimode fibers can be described by a generalized nonlinear Schrödinger equation (GNLSE) [12]–[14]. Using the GNLSE, we derive a set of general coupled equations describing the intermodal FWM process in a GIMF. An interesting analytic expression regarding the phase matching condition in these fibers is presented. For different spatial mode combinations of the pump, signal

and idler the phase-matching conditions are analyzed and the nonlinear coefficients are calculated.

II. BRIEF OVERVIEW OF GIMFs

In this section, we present a brief overview of GIMFs and establish the notation that will be used in the rest of the paper [15]. The refractive index profile of a GIMF is given by

$$\begin{aligned} n^2(\rho) &= n_0^2 \left[1 - 2\Delta \left(\frac{\rho}{R} \right)^\alpha \right] & \rho \leq R, \\ &= n_0^2 (1 - 2\Delta) & \rho > R, \end{aligned} \quad (1)$$

where R is the core radius, n_0 is the maximum refractive index in the center of the core, Δ is the relative index difference between the core and cladding, and $\alpha \approx 2$ characterizes a near parabolic-index profile. The spatial transverse profile of the electric field of a propagating mode can be decomposed into separate radial and angular components as

$$F_{p,m}(\rho, \phi) = \tilde{F}_{p,m}(\rho) e^{im\phi}, \quad (2)$$

where [16]

$$\tilde{F}_{p,m}(\rho) = \tilde{A}_p^m \frac{\rho^m}{\rho_0^{m+1}} \exp\left(-\frac{\rho^2}{2\rho_0^2}\right) L_p^m\left(\frac{\rho^2}{\rho_0^2}\right), \quad (3)$$

and

$$\rho_0 = \frac{R}{(4N_2)^{1/4}}, \quad \tilde{A}_p^m = \sqrt{\frac{p!}{\pi(p+m)!}}. \quad (4)$$

L_p^m is the generalized Laguerre polynomial. Here, each mode is labeled by two integers, $p \geq 0$ and $m \geq 0$, referred to as the radial and angular mode order, respectively. The coefficients in the field profile in Eq. 3 are chosen such that the fields are orthonormal according to

$$\int_0^{2\pi} d\phi \int_0^\infty \rho d\rho F_{p',m'}(\rho, \phi) F_{p,m}(\rho, \phi) = \delta_{pp'} \delta_{mm'}. \quad (5)$$

The total number of guided modes (counting the polarization degeneracy) is given as

$$N_\alpha = \frac{\alpha}{\alpha + 2} n_0^2 k^2 R^2 \Delta, \quad (6)$$

where N_2 in Eq. 3 is also given by Eq. 6, and $k = 2\pi/\lambda$.

The near parabolic shape of the refractive index profile in Eq. 1 is due to the near parabolic Germanium (Ge) doping concentration d in the core of the GIMF.

$$\begin{aligned} d(\rho) &= d_0 \left[1 - \left(\frac{\rho}{R} \right)^\alpha \right] & \rho \leq R, \\ &= 0 & \rho > R, \end{aligned} \quad (7)$$

E. Nazemosadat is with the Department of Electrical Engineering and Computer Science, University of Wisconsin-Milwaukee, Milwaukee, WI, 53211 USA (e-mail:nazemosa@uwm.edu).

H. Pourbeyram and A. Mafi are with the Department of Physics and Astronomy, University of New Mexico, Albuquerque, NM, USA.

A. Mafi is also with the Center for High Technology Materials, University of New Mexico, Albuquerque, NM, USA.

A. Mafi and E. Nazemosadat acknowledge support from the Air Force Office of Scientific Research under Grant FA9550-12-1-0329. A. Mafi and H. Pourbeyram acknowledge support from the National Science Foundation under Award Number 1253233.

Copyright (c) 2011 IEEE. Personal use of this material is permitted. However, permission to use this material for any other purposes must be obtained from the IEEE by sending a request to pubs-permissions@ieee.org.

Manuscript received December 12, 2014; revised December 12, 2014.

where d_0 is the maximum doping in weight percentage (wt%) at the center of the core. At each given value of Ge doping concentration, the refractive index can be accurately described by a fit to the Sellmeier equation, where the Sellmeier coefficients depend on the Ge doping concentration. In particular, the Sellmeier coefficients are available in Refs. [17], [18] for pure fused silica (refractive index represented as $n_{\text{si}}(\lambda)$), and Ge-doped fused silica with a Ge doping concentration of 6.3-wt% (refractive index represented as $n_{6.3}(\lambda)$). Here, we have implicitly assumed that the refractive index of the Ge-doped fused silica increases linearly with the Ge doping concentration and we have already relied on this assumption to relate Eqs. 1 and 7. This is a reasonable approximation, which is also supported by experimental measurements [19]. Therefore, we derive a generalized Sellmeier equation to incorporate the dependence of the refractive index on both the wavelength and Ge doping concentration of fused silica as

$$n^2(\lambda, d) = n_{\text{si}}^2(\lambda) + \frac{d}{6.3} [n_{6.3}^2(\lambda) - n_{\text{si}}^2(\lambda)], \quad (8)$$

where d is again the Ge doping concentration in wt%. The utility of Eq. 8 is that it provides, along with Eqs. 1 and 7, a reliable estimate of the refractive index for a broad wavelength span from near-ultraviolet through mid-infrared region for common levels of Ge doping concentration in GIMFs.

All the modes with equal group mode number $g = 2p + |m| + 1$ are almost degenerate in the value of the propagation constant, which is given according to the formula

$$\beta_g = n_0 k (1 - 2\Delta x)^{1/2}, \quad (9)$$

where

$$x = \left(\frac{g}{\sqrt{N\alpha}} \right)^{2\alpha/(\alpha+2)}. \quad (10)$$

There are three important points of caution regarding the use of analytical equations presented above. The first point is that Eq. 3 is only strictly valid for $\alpha = 2$; however, the deviations are small and Eq. 3 is often very reliable. The second point is that Eq. 3 is only a solution of the Maxwell's equations in the core of the fiber and must be matched to an exponentially decaying modified Bessel function of the second kind in the cladding. In calculating the overlap integrals for coupling in and out of the GIMF, as long as the beam-diameters of the in-coupling and out-coupling "often"-Gaussian fields are smaller than the core diameter of the GIMF, it is perfectly fine to use Eq. 3. For larger in-coupling beam diameters, the use of Eq. 3 can still be at least qualitatively valid. In such cases, better accuracy can be achieved if the cladding profile is properly accounted for, for example by using a numerical solver. In either case, small adjustments in the normalization coefficients of Eq. 3 are expected according to Eq. 5 in order to compensate for substituting Eq. 3 for the modified Bessel function of the second kind in the cladding. The third point is that the presence of the cladding removes the degeneracy among modes within a mode group, both in the propagation constant and the group velocity. While this effect is generally quite small, it is more pronounced for higher order mode groups, which have a larger overlap with the cladding.

III. FWM IN A MULTIMODE OPTICAL FIBER

Four-wave mixing in a MMF can be described by considering a pump, a signal and an idler wave oscillating at frequencies ω_p , ω_s and ω_i , respectively. During the FWM process two pump photons are annihilated and two photons at the signal and idler frequencies are created simultaneously, such that the net energy and momentum are conserved. It is assumed that all three waves are linearly polarized along the \hat{x} axis and that they maintain their state of polarization while propagating in the MMF. This paper focuses on FWM among multiple spatial modes and therefore, polarization-related phenomena are left for future work.

The (scalar) electric field is decomposed into a sum of mode functions $F_\mu(x, y, \omega)$ with envelopes $A_\mu(z, \omega)$

$$E(x, y, z, t) = \frac{1}{2} \sum_\mu \int d\omega \left\{ \frac{F_\mu(x, y, \omega)}{N_\mu(\omega)} A_\mu(z, \omega) \times \exp[i(\tilde{\beta}_\mu(\omega)z - \tilde{\omega}t)] + c.c. \right\}. \quad (11)$$

We define

$$\tilde{\beta}_\mu(\omega) = \beta_\mu(\omega) - \beta_{\text{fun}}(\omega_{\text{ref}}), \quad \tilde{\omega} = \omega - \omega_{\text{ref}}, \quad (12)$$

where $\beta_\mu(\omega)$ is the propagation constant of mode μ at frequency ω , and $\beta_{\text{fun}}(\omega_{\text{ref}})$ is the propagation constant of the fundamental mode at frequency ω_{ref} . The fundamental mode is taken to be the mode with the largest value of the propagation constant in this paper. The field normalization constant $N_\mu(\omega)$ is chosen such that the mode profile satisfies the normalization and orthogonality condition

$$\iint dx dy F_\mu^*(x, y, \omega) F_\nu(x, y, \omega) = \delta_{\mu\nu}. \quad (13)$$

Considering that FWM in a MMF leads to a wide separation between the frequencies of the pump, signal, and idler, it is appropriate to use separate carrier frequencies for each of these beams. Therefore, for the spatial mode μ , separate envelopes A_μ^p , A_μ^s , and A_μ^i are assumed for the pump, signal, and idler, respectively. The upper p, s, i indices refer to the pump, signal, idler envelopes, and the lower indices refer to the spatial modes. The field can then be written in the form of

$$A_\mu(z, t) = A_\mu^p(z, t) e^{i\tilde{\beta}_\mu(\omega_p)z} + A_\mu^s(z, t) e^{i\Omega t} e^{i\tilde{\beta}_\mu(\omega_s)z} + A_\mu^i(z, t) e^{-i\Omega t} e^{i\tilde{\beta}_\mu(\omega_i)z}, \quad (14)$$

where $\Omega = \omega_p - \omega_s = \omega_i - \omega_p$. It is assumed that $\omega_{\text{ref}} = \omega_p$, which leads to $\tilde{\beta}_{\text{fun}}(\omega_p) = 0$. The optical power carried by mode μ is $|A_\mu(z, t)|^2$, where $A_\mu(z, t)$ is the Fourier transform of $A_\mu(z, \omega)$.

The formulation of the nonlinear pulse propagation in a multimode optical fiber is based on the pioneering work of Kolesik and Moloney [20] and Poletti and Horak [12]. More recently a simplified form of the GNLSE was presented in Ref. [13], which describes the propagation of light in GIMFs. By substituting Eq. 14 in the GNLSE of Ref. [13], the coupled nonlinear equations governing the evolution of $A_\mu^p(z, t)$,

$A_\mu^s(z, t)$, and $A_\mu^i(z, t)$ are obtained and can be expressed as

$$\begin{aligned} \frac{\partial A_\mu^p}{\partial z} = & i \sum_{n>0} \frac{\beta_\mu^{(n)}(\omega_p)}{n!} \left(i \frac{\partial}{\partial t} \right)^n A_\mu^p \\ & + i \frac{n_2 \omega_p}{c} \left[\sum_{\nu, \kappa, \xi} \gamma_{\mu\nu\kappa\xi}^{pppp} \Phi_{\mu\nu\kappa\xi}^{pppp} A_\nu^p A_\kappa^p A_\xi^{p*} \right. \\ & + 2 \sum_{\nu, \kappa, \xi} \gamma_{\mu\nu\kappa\xi}^{ppss} \Phi_{\mu\nu\kappa\xi}^{ppss} A_\nu^p A_\kappa^s A_\xi^{s*} \\ & + 2 \sum_{\nu, \kappa, \xi} \gamma_{\mu\nu\kappa\xi}^{ppii} \Phi_{\mu\nu\kappa\xi}^{ppii} A_\nu^p A_\kappa^i A_\xi^{i*} \\ & \left. + 2 \sum_{\nu, \kappa, \xi} \gamma_{\mu\nu\kappa\xi}^{psip} \Phi_{\mu\nu\kappa\xi}^{psip} A_\nu^s A_\kappa^i A_\xi^{p*} \right]. \end{aligned} \quad (15)$$

$$\begin{aligned} \frac{\partial A_\mu^s}{\partial z} = & i \sum_{n>0} \frac{\beta_\mu^{(n)}(\omega_s)}{n!} \left(i \frac{\partial}{\partial t} \right)^n A_\mu^s \\ & + i \frac{n_2 \omega_s}{c} \left[\sum_{\nu, \kappa, \xi} \gamma_{\mu\nu\kappa\xi}^{ssss} \Phi_{\mu\nu\kappa\xi}^{ssss} A_\nu^s A_\kappa^s A_\xi^{s*} \right. \\ & + 2 \sum_{\nu, \kappa, \xi} \gamma_{\mu\nu\kappa\xi}^{sspp} \Phi_{\mu\nu\kappa\xi}^{sspp} A_\nu^s A_\kappa^p A_\xi^{p*} \\ & + 2 \sum_{\nu, \kappa, \xi} \gamma_{\mu\nu\kappa\xi}^{ssii} \Phi_{\mu\nu\kappa\xi}^{ssii} A_\nu^s A_\kappa^i A_\xi^{i*} \\ & \left. + \sum_{\nu, \kappa, \xi} \gamma_{\mu\nu\kappa\xi}^{sppi} \Phi_{\mu\nu\kappa\xi}^{sppi} A_\nu^p A_\kappa^i A_\xi^{s*} \right]. \end{aligned} \quad (16)$$

The nonlinear equation for the idler can be constructed from Eq. 16 by exchanging all the signal and idler indices ($s \leftrightarrow i$). These equations include the effects of self phase modulation (SPM), cross phase modulation (XPM) and FWM. It should be noted that only the relevant FWM terms that satisfy the conservation of energy, $2\omega_p = \omega_s + \omega_i$, are retained. In the equations above, n_2 is the nonlinear index coefficient and $\Phi(z)$ are the spatial phase terms. Three representative examples are given in Eq. 17 from which all the other phase terms can be easily written.

$$\begin{aligned} \Phi_{\mu\nu\kappa\xi}^{pppp}(z) &= \exp \left[i(-\beta_\mu^p + \beta_\nu^p + \beta_\kappa^p - \beta_\xi^p)z \right], \\ \Phi_{\mu\nu\kappa\xi}^{ssii}(z) &= \exp \left[i(-\beta_\mu^s + \beta_\nu^s + \beta_\kappa^i - \beta_\xi^i)z \right], \\ \Phi_{\mu\nu\kappa\xi}^{sppi}(z) &= \exp \left[i(-\beta_\mu^s + \beta_\nu^p + \beta_\kappa^i - \beta_\xi^i)z \right]. \end{aligned} \quad (17)$$

β_μ^p is the propagation constant of the spatial mode μ at the pump frequency ω_p : $\beta_\mu^p = \beta_\mu(\omega_p)$, and so on. We also have

$$\beta_\mu^{(n)}(\omega_j) = \frac{\partial^n}{\partial \omega^n} \beta_\mu(\omega) \Big|_{\omega=\omega_j}, \quad j = p, s, i. \quad (18)$$

Three representative examples of the nonlinear coupling terms appearing in Eqs. 15 and 16 are given as

$$\begin{aligned} \gamma_{\mu\nu\kappa\xi}^{pppp} &= \iint dxdy F_\mu^*(\omega_p) F_\nu(\omega_p) F_\kappa(\omega_p) F_\xi^*(\omega_p), \\ \gamma_{\mu\nu\kappa\xi}^{ssii} &= \iint dxdy F_\mu^*(\omega_s) F_\nu(\omega_s) F_\kappa(\omega_i) F_\xi^*(\omega_i), \\ \gamma_{\mu\nu\kappa\xi}^{sppi} &= \iint dxdy F_\mu^*(\omega_s) F_\nu(\omega_p) F_\kappa(\omega_p) F_\xi^*(\omega_i). \end{aligned} \quad (19)$$

all other nonlinear coupling terms can be easily written using these examples.

IV. FWM IN A GRADED-INDEX MULTIMODE FIBER

Equations 15 and 16 are very complex and include the effects of SPM, XPM, and FWM processes. In general, solving these equations requires a powerful numerical algorithm. However, much insight will be obtained by making a few approximations that are easily justifiable in many practical situations [7]. In the following, it is assumed that the pump field remains much stronger than the signal and idler and remains undepleted during the FWM interaction. This simplifies the equations to:

$$\begin{aligned} \frac{\partial A_\mu^p}{\partial z} = & i \sum_{n>0} \frac{\beta_\mu^{(n)}(\omega_p)}{n!} \left(i \frac{\partial}{\partial t} \right)^n A_\mu^p \\ & + i \frac{n_2 \omega_p}{c} \sum_{\nu, \kappa, \xi} \gamma_{\mu\nu\kappa\xi}^{pppp} \Phi_{\mu\nu\kappa\xi}^{pppp} A_\nu^p A_\kappa^p A_\xi^{p*}. \end{aligned} \quad (20)$$

$$\begin{aligned} \frac{\partial A_\mu^s}{\partial z} = & i \sum_{n>0} \frac{\beta_\mu^{(n)}(\omega_s)}{n!} \left(i \frac{\partial}{\partial t} \right)^n A_\mu^s \\ & + i \frac{n_2 \omega_s}{c} \left[2 \sum_{\nu, \kappa, \xi} \gamma_{\mu\nu\kappa\xi}^{sspp} \Phi_{\mu\nu\kappa\xi}^{sspp} A_\nu^s A_\kappa^p A_\xi^{p*} \right. \\ & \left. + \sum_{\nu, \kappa, \xi} \gamma_{\mu\nu\kappa\xi}^{sppi} \Phi_{\mu\nu\kappa\xi}^{sppi} A_\nu^p A_\kappa^i A_\xi^{s*} \right]. \end{aligned} \quad (21)$$

The nonlinear equation for the idler can again be constructed from Eq. 21 by exchanging all the signal and idler indices ($s \leftrightarrow i$).

The last line in Eq. 21 contains the FWM terms that couple the pump, signal, and idler. Efficient FWM requires the vanishing of the effective phase mismatch [7]. In a SMF, the linear phase mismatch is often compensated by a nonlinear contribution to the phase. However, in a MMF such as the GIMF, it is possible to satisfy the phase-matching condition required for FWM even in the near-linear regime where the pump power is low. The linear phase-matching has a few distinctive features in that it involves multiple modes, signal and idler frequencies are far from the pump, and the effect of the nonlinear phase on the phase-matched signal and idler frequencies is negligible. The FWM phase-matching condition requires

$$\left[\Phi_{\mu\nu\kappa\xi}^{sppi}(z) = 1 \right] \leftrightarrow \left[\Delta k = \beta_\mu^s + \beta_\xi^i - \beta_\nu^p - \beta_\kappa^p = 0 \right] \quad (22)$$

In a GIMF, the propagation constants of the modes in Eq. 9 depend on the mode group number. Therefore, the phase-matching condition of Eq. 22 can be cast in terms of the mode group numbers of the pump, signal, and idler modes expressed as $\{g_p^{(1)}, g_p^{(2)}, g_i, g_s\}$. This represents phase-matching between a pump beam belonging to mode group $g_p^{(1)}$, another pump beam belonging to mode group $g_p^{(2)}$, the idler beam belonging to mode group g_i , and the signal beam belonging to mode group g_s . Eigenmodal analysis was performed using the finite element method in order to calculate the propagation constants of the beams [21]. In Fig. 1, we consider possible phase-matching of the form $\{1, 1, g_i, g_s\}$; therefore, the pump modes are assumed to be in the lowest order mode of the GIMF ($g_p^{(1)} = g_p^{(2)} = 1$). The horizontal axis in Fig. 1 represents the

pump wavelength and the vertical axis represents the phase-matched idler wavelength. The solid (black) line shows the phase-matching for $\{1,1,1,2\}$, where the two pump beams, idler, and signal, propagate in the modes belonging to group numbers 1, 1, 1, and 2, respectively.

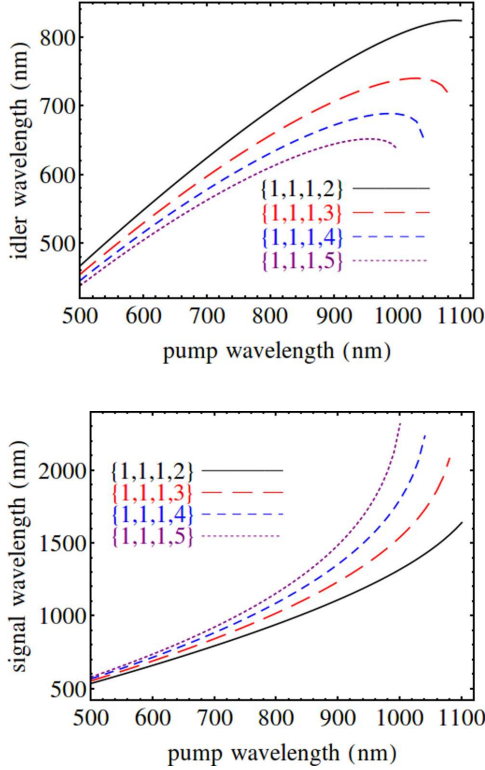


Fig. 1. The phase-matching condition is the same for all $\{1,1,g_i,g_s\}$ configurations where $g_i + g_s$ is the same. Therefore, $\{1,1,2,3\} \equiv \{1,1,1,4\}$.

V. PHASE-MATCHING IN GRADED-INDEX MULTIMODE FIBERS

For $\Delta \ll 1$, Eq. 9 can be simplified and written as

$$\beta_g \approx n_0 k \left(1 - \Delta x - \frac{\Delta^2 x^2}{2} \right) + O(\Delta^3), \quad (23)$$

For short propagation lengths the $O(\Delta^2)$ term can be neglected because it does not amount to substantial extra phase mismatch between different mode groups. For situations where this term can be ignored and $\alpha \approx 2$ can be trusted, Eq. 23 transforms into

$$\beta_g = n_0 k - \frac{\sqrt{2\Delta}}{R} g, \quad (24)$$

The phase-matching condition is

$$\kappa = \Delta k_M + \Delta k_W + \Delta k_{NL} = 0, \quad (25)$$

where κ is the summation of the mismatch occurring due to material dispersion (Δk_M), waveguide dispersion (Δk_W) and nonlinear effects (Δk_{NL}). Assuming that Δk_{NL} is negligible, the phase-matching condition is satisfied when the linear phase mismatch $\Delta k = \Delta k_M + \Delta k_W$ is zero; $\Delta k_M = -\Delta k_W$. The mismatch contribution of the material and waveguide dispersion for $\{1,1,1,3\}$ and $\{1,1,1,5\}$ configurations are

shown in Fig. 2. Phase-matching occurs at the intersection of the Δk_M and $-\Delta k_W$ curves.

Using Eqs. 22, 24 and 25, we can find

$$\Delta k_M = n_0(\omega_s)k_s + n_0(\omega_i)k_i - 2n_0(\omega_p)k_p, \quad (26)$$

$$\Delta k_W = -\frac{\sqrt{2\Delta}}{R} C_{\text{FWM}}, \quad (27)$$

where C_{FWM} is defined as

$$C_{\text{FWM}} = g_i + g_s - (g_p^{(1)} + g_p^{(2)}) \quad (28)$$

Although the relative index step Δ is a function of the wavelength, this dependency is negligible. Therefore, Δ can be assumed to be a constant value for all wavelengths. This approximation is considered in the derivation of Eq. 27. Consequently, according to Eq. 27, Δk_W can be approximated to be independent of the wavelength as well (seen as an almost horizontal line in Fig. 2), and so it only depends on the mode group number of the participating waves. Therefore, different mode combinations of pump, signal and idler that exhibit the same C_{FWM} value, will have similar phase-matching conditions. This means that if in separate FWM setups, different modes of a pump beam placed at a fixed wavelength are excited, the FWM interactions which have identical C_{FWM} s will generate signals (idlers) with identical wavelengths.

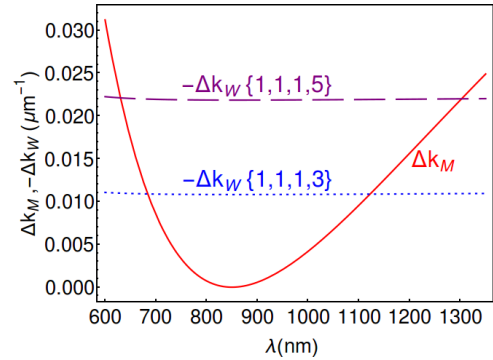


Fig. 2. The phase-matching curve for FWM in the considered GIMF for a pump wavelength of 850 nm. The Δk_M curve displays the contribution from the material dispersion and the Δk_W curves display the waveguide dispersion contributions for two different combinations of spatial modes.

For a better understanding, a number of equivalent configurations are mentioned in Table I. Although all of these spatial mode combinations satisfy the phase matching condition and are equivalent wavelength-wise (result in identical signal and idler wavelengths if FWM process occurs), they have different FWM efficiencies. The reason is that the efficiency depends on the overlap integral of the participating spatial modes (see Eq. 19), which is different for each case. This can be observed in Tables II and III, where the FWM efficiency of some phase matched beams are displayed through their nonlinear coupling terms. In Table II the pump wavelength is $\lambda_p = 850$ nm, while that of Table III is 1064 nm. In both cases it is assumed that the first pump beam belongs to mode group $g_p^{(1)} = 1$ which is related to the LP_{01} mode. Also, it is worth mentioning that the nonlinear coupling terms $\gamma_{\mu\nu\kappa\zeta}^{\text{ipps}}$ will only have non-zero values when $m_\mu^i - m_\nu^p - m_\kappa^p + m_\zeta^s = 0$, where m_μ^j is the angular

TABLE I
MODE COMBINATIONS WITH EQUIVALENT PHASE-MATCHING CONDITIONS

$\{1,1,1,2\} \equiv \{1,2,2,2\} \equiv \{1,2,1,3\}$
$\{1,1,1,3\} \equiv \{1,1,2,2\}$
$\{1,1,1,4\} \equiv \{1,1,2,3\}$
$\{1,1,1,5\} \equiv \{1,1,3,3\}$
$\{1,2,1,2\} \equiv \{1,3,2,2\} \equiv \{1,3,1,3\}$

mode order of the μ th mode at frequency j (see Eq. 2). For instance, the combinations $\{1,1,1,2\}$ and $\{1,1,1,4\}$ and their equivalents do not satisfy this condition and thus do not exist.

TABLE II
 $\lambda_p = 850 \text{ nm}$

Pump 2	Idler	Signal	γ^{sppi}
LP ₀₁	LP ₀₁ , 683.9 nm	LP ₀₂ , 1122.8 nm	0.608
LP ₀₁	LP ₀₂ , 684 nm	LP ₀₁ , 1122.3 nm	0.3645
LP ₀₁	LP ₀₁ , 630.2 nm	LP ₀₃ , 1305.1 nm	0.277
LP ₀₁	LP ₀₃ , 630.7 nm	LP ₀₁ , 1302.9 nm	0.0074
LP ₀₂	LP ₀₂ , 683.7 nm	LP ₀₂ , 1123.1 nm	0.2667
LP ₂₁	LP ₂₁ , 683.7 nm	LP ₀₂ , 1123.1 nm	-0.0408
LP ₂₁	LP ₀₂ , 683.7 nm	LP ₂₁ , 1123.1 nm	-0.1649
LP ₁₁	LP ₁₁ , 683.8 nm	LP ₀₂ , 1122.9 nm	0.1346
LP ₁₁	LP ₀₂ , 683.9 nm	LP ₁₁ , 1122.7 nm	-0.1075

TABLE III
 $\lambda_p = 1064 \text{ nm}$

Pump 2	Idler	Signal	γ^{sppi}
LP ₀₁	LP ₀₁ , 733.9 nm	LP ₀₂ , 1933.7 nm	0.5225
LP ₀₁	LP ₀₂ , 739.2 nm	LP ₀₁ , 1898.2 nm	0.2014
LP ₀₂	LP ₀₂ , 734.3 nm	LP ₀₂ , 1931.1 nm	0.2225
LP ₂₁	LP ₂₁ , 734.3 nm	LP ₀₂ , 1931.1 nm	0.0439
LP ₂₁	LP ₀₂ , 734.3 nm	LP ₂₁ , 1931.1 nm	-0.1217
LP ₁₁	LP ₁₁ , 734.1 nm	LP ₀₂ , 1932.4 nm	0.1923
LP ₁₁	LP ₀₂ , 736.8 nm	LP ₁₁ , 1913.7 nm	-0.1229

VI. PARAMETRIC GAIN AND BANDWIDTH

In order to use FWM in MMFs for amplification or wavelength conversion applications, it is required to know the amount of gain and its bandwidth. To understand the basic features of parametric gain, we restrict our studies to the case where the pump beam propagates in a single fiber mode. The parametric gain coefficient g is defined as [6], [7]

$$g = \sqrt{(\gamma^{sppi} P_0)^2 - (\kappa/2)^2}, \quad (29)$$

where P_0 is the incident pump power at $z = 0$, and κ is defined as

$$\kappa = \Delta k + (\gamma^{spps} + \gamma^{ippi} - 2\gamma^{pppp})P_0, \quad (30)$$

For simplicity, we consider the case where only the signal P_{s0} is launched into the fiber together with the pump, and the initial idler power is zero. Using the coupled wave equations describing FWM, the general solution for the signal and idler

powers at the end of a fiber of length L , defined as P_s and P_i , are expressed as [6]

$$G_s = \frac{P_s}{P_{s0}} = 1 + (\gamma^{sppi} P_0 L)^2 \frac{\sinh^2(gL)}{(gL)^2}, \quad (31)$$

$$G_i = \frac{P_i}{P_{s0}} = (\gamma^{sppi} P_0 L)^2 \frac{\sinh^2(gL)}{(gL)^2}, \quad (32)$$

where Eqs. 31 and 32 describe the signal amplification and idler generation, respectively. The maximum G_s occurs at the signal wavelength where the phase-matching condition is perfectly satisfied ($\kappa = 0$). As κ increases, g decreases, and drops to zero for $\kappa/2 = \gamma^{sppi} P_0$. If κ is further increased, g becomes imaginary and for $gL = \pm i\pi$, $G_s = 0$, which when substituted in Eq. 29 gives us the bandwidth as

$$\Delta\kappa_B = 2\sqrt{\left(\frac{\pi}{L}\right)^2 + (\gamma^{sppi} P_0)^2}, \quad (33)$$

VII. CONCLUSIONS

We have presented a detailed theoretical description of FWM in GIMFs. After simplifying the analytical term describing phase mismatch in these fibers, our analysis has resulted in a useful universal expression for finding separate mode combinations of pump, signal and idler that have similar phase-matching conditions.

REFERENCES

- [1] R. Essiambre, G. Kramer, P.J. Winzer, G.J. Foschini, and B. Goebel, "Capacity Limits of Optical Fiber Networks," *J. Lightwave Technol.* **28**, 662–701, (2010).
- [2] R. W. Tkach, "Scaling optical communications for the next decade and beyond," *Bell Labs Tech. J.* **14**, 3–9 (2010).
- [3] R. H. Stolen, J. E. Bjorkholm, and A. Ashkin, "Phase-matched three-wave mixing in silica fiber optical waveguides," *Appl. Phys. Lett.* **24**, 308–310 (1974).
- [4] C. Lin and M. A. Bösch, "Large-Stokes-shift stimulated fourphoton mixing in optical fibers," *Appl. Phys. Lett.* **38**, 479–481 (1981).
- [5] K. O. Hill, D. C. Johnson, and B. S. Kawasaki, "Efficient conversion of light over a wide spectral range by four-photon mixing in a multimode graded-index fiber," *Appl. Opt.* **20**, 1075–1079 (1981).
- [6] R. H. Stolen, and J. E. Bjorkholm, "Parametric amplification and frequency conversion in optical fibers," *IEEE J. Quantum Electron.* **18**, 1062–1072 (1982).
- [7] G. P. Agrawal, "Nonlinear Fiber Optics, 4th ed.," Academic Press, San Diego (2007).
- [8] G. P. Agrawal, "Nonlinear fiber optics: its history and recent progress [invited]," *J. Opt. Soc. Am. B* **28**, A1–A10 (2011).
- [9] R. Olshansky and D. B. Keck, "Pulse broadening in graded-index optical fibers," *Appl. Opt.* **15**, 483–491 (1976).
- [10] S. Raghavan and G. P. Agrawal, "Spatiotemporal solitons in inhomogeneous nonlinear media," *Opt. Commun.* **180**, 377–382 (2000).
- [11] W.H. Renninger and F. W. Wise, "Optical solitons in graded-index multimode fibres," *Nat. Commun.* **4**, 1719 (2013).
- [12] F. Poletti and P. Horak, "Description of ultrashort pulse propagation in multimode optical fibers," *J. Opt. Soc. Am. B* **25**, 1645–1654 (2008).
- [13] A. Mafi, "Pulse propagation in a short nonlinear graded-index multimode optical fiber," *J. Lightwave Technol.* **30**, 2803–2811 (2012).
- [14] E. Nazemosadat and A. Mafi, "Nonlinear multimodal interference and saturable absorption using a short graded-index multimode optical fiber," *J. Opt. Soc. Am. B* **30**, 1357–1367 (2013).
- [15] D. Gloge and E. A. J. Marcatili, "Multimode theory of graded-core fibers," *Bell. Syst. Tech. J.* **52**, 1563–1578 (1973).
- [16] A. Mafi, "Bandwidth improvement in multimode optical fibers via scattering from core inclusions," *J. Lightwave Technol.* **28**, 1547–1555 (2010).
- [17] K. Okamoto, "Fundamentals of optical waveguides, 2nd ed.," Academic Press, San Diego (2006).

- [18] N. Shibata and T. Edahtiro, "Refractive index dispersion properties of glasses for optical fibers," Paper of Technical Group, IEICE Japan, no. OQE80, 114–118 (1980).
- [19] T. Izawa and S. Sudo, "Optical Fibers: Materials and Fabrication," KTK Scientific Publisher, Tokyo (1987).
- [20] M. Kolesik and J. V. Moloney, "Nonlinear optical pulse propagation simulation: From Maxwell's to unidirectional equations," *Phys. Rev. E* **70** 036604 (2004).
- [21] T. A. Lenahan, "Calculation of modes in an optical fiber using the finite element method and EISPACK," *Bell Syst. Tech. J.* **62**, 2663–2694 (1983).